Ph.D. Thesis

Theoretical investigation of the reactions of the OH radical with C_2H_6, CH_3NH_2 and glycine molecules

Balázs Gruber

Supervisor:

Dr. Gábor Czakó

Associate professor
Doctor of the Hungarian Academy of Sciences

University of Szeged
Faculty of Science and Informatics
Department of Physical Chemistry and Materials Science
Doctoral School of Chemistry

MTA-SZTE Lendület Computational Reaction Dynamics Research Group

Szeged, 2024

Content

PUBLICATIONS COVERED IN THE THESIS

[1] **B. Gruber** and G. Czakó: *Benchmark ab initio characterization of the abstraction and substitution pathways of the OH + CH$_4$/C$_2$H$_6$ reactions,* Phys. Chem. Chem. Phys., 22, 14560 (2020)

[2] **B. Gruber**, V. Tajti and G. Czakó**: *Full-dimensional automated potential energy surface development and dynamics for the OH + C$_2$H$_6$ reaction*, J. Chem. Phys.*, 157, 074307 (2022)

[3] **B. Gruber** and G. Czakó: *High-level ab initio mapping of the multiple H-abstraction pathways of the OH + glycine reaction*, Phys. Chem. Chem. Phys.*, 25, 5271 (2023)

[4] **B. Gruber**, V. Tajti and G. Czakó: *Vibrational mode-specific dynamics of the OH + C$_2$H$_6$ reaction*, J. Phys. Chem. A*, 127, 7364 (2023)

[5] G. Czakó, **B. Gruber**, D. Papp, V. Tajti, D. A. Tasi and C. Yin: *First-principles mode-specific reaction dynamics*, Phys. Chem. Chem. Phys., 26, 15818 (2024)

[6] **B. Gruber** and G. Czakó: *High-level ab initio characterization of the OH + CH$_3$NH$_2$ reaction*, Phys. Chem. Chem. Phys., 26, 28543 (2024)

PUBLICATIONS RELATED TO THE THESIS

[7] D. Papp, **B. Gruber** and G. Czakó, *Detailed benchmark ab initio mapping of the potential energy surfaces of the X + C$_2$H$_6$ [X = F, Cl, Br, I] reactions*, Phys. Chem. Chem. Phys., 21, 396 (2019)

1 INTRODUCTION AND OBJECTIVES

To thoroughly investigate complex chemical reactions quantum chemical methods are indispensable. Quantum chemistry offers advanced computational tools that enable precise descriptions of molecular electronic structures and detailed explorations of chemical reaction mechanisms.[1] These methods allow researchers to calculate potential energy surfaces, analyze reaction dynamics and predict the outcomes of chemical processes with high accuracy. The field of quantum chemical reaction dynamics has evolved significantly over the years beginning with the pioneering work of Schatz and Kuppermann. They achieved a landmark breakthrough by solving the quantum mechanical description of the H + H_2 reaction marking the start of major advancements in the field.[2] Subsequent research was expanded to include various three-atom systems such as reactions involving H, F, and Cl with H_2O.[3,4,5] This exploration led to the development of the Polanyi rules, which provide a framework for predicting reaction dynamics based on the relative position of transition state compared to the reactants and products.[6] According to the Polanyi rules, the impact of collision energy versus vibrational excitation on reactivity depends on the nature of the transition state. For reactions with an "early" barrier, where the transition state closely resembles the reactants, collision energy has a greater influence on reactivity compared to vibrational excitation. Conversely, if the transition state is more product-like, vibrational excitation plays a more significant role in enhancing reactivity. As the number of atoms increases, so does the number of vibrational degrees of freedom, which can affect reactivity differently in polyatomic systems, sometimes leading to deviations from the Polanyi rules. The 1990s marked a transition towards studying larger molecular systems with significant focus on the reaction between H and H_2O, which became one of the most thoroughly investigated polyatomic reactions.[7,8,9,10,11] As the new millennium began, research efforts were expanded to include the reactions of methane and its isotopically-labeled variants.[12,13,14,15,16,17,18,19,20,21,22] This period also initiated the exploration of even more complex systems and nowdays it is possible to investigate seven or more atomic chemical systems with highly-accurate first-princliples tools. In light of these advancements, this dissertation employs quantum chemical and quasi-classical methods to theoretically investigate OH radical reactions with ethane, methylamine and glycine molecules.

The hydroxyl radical is a highly reactive species with crucial roles in various chemical processes both on Earth and beyond. In atmospheric chemistry, the OH radical is essential for the degradation of pollutants and the transformation of greenhouse gases contributing significantly to the chemical balance of the atmosphere.[23] Similarly, in space chemistry, OH radical reactions provide insights into the chemical processes occurring in interstellar environments and on celestial bodies aiding our understanding of the chemical evolution of the universe. In addition to its importance in atmospheric and space chemistry, the OH radical is also vital in biochemical processes. It plays a crucial role in the oxidation of organic molecules such as amines and amino acids. Studying OH radical reactions in this context is vital for clarifying the chemical processes within biological systems and for uncovering the underlying mechanisms of different biochemical phenomena.

Ethane is released into the atmosphere through both natural processes such as the degradation of organic molecules and human activities including fossil fuel combustion.[24,25] In the atmosphere, the interaction between OH radicals and ethane is fundamental to understanding the degradation of alkanes and the formation of secondary pollutants. In combustion processes, the $OH + C_2H_6$ reaction is integral to the understanding of fuel oxidation mechanisms. Ethane is used as a fuel in various industrial applications and understanding its reaction with OH radicals helps in optimizing combustion efficiency and reducing emissions. Ethane is also a key feedstock in the chemical industry, where it is used to produce ethylene and other chemicals. Understanding its reaction with OH radicals can help refine industrial processes by controlling reaction conditions and reducing the formation of undesired products. All in all, by investigating the mechanisms and dynamics of the $OH + C_2H_6$ reaction, we can enhance our knowledge of its role in atmospheric chemistry, combustion processes and industrial applications contributing to improved pollution control and process optimization.

Understanding the reaction of hydroxyl radicals with ethane is significantly informed by studies of related reactions, particularly the $OH + CH_4$ reaction. Methane serves as a simpler model providing valuable insights into the mechanisms that are also relevant to ethane. In 1993, Dobbs and Dixon investigated the $OH + CH_4 \rightarrow H_2O + CH_3$ abstraction reaction using *ab initio* methods.[26] They employed Hartree−Fock (HF) and

second-order perturbation theory (MP2) methods with various basis sets including polarized double-zeta (DZ+P) and twice-polarized triple-zeta (TZ+2P and TZ+2P+f). Their study revealed differences in transition-state structures depending on the computational method used: the HF method led to an open conformation for the CH_3 group and the attached hydroxyl hydrogen, while the MP2 method resulted in a closed conformation. Additionally, they observed that the distance between the oxygen atom and the departing hydrogen atom from methane was greater at the MP2 level compared to the C-H distance, although the HF method indicated a longer O-H bond. Their computations at the MP2/TZ+2P+f level were consistent with experimental data and they determined the reaction barrier height, zero-point energy corrected values and reaction enthalpy. Li and Guo in 2015 further advanced the understanding of the OH + CH_4 reaction by developing a global potential energy surface (PES).[27] They utilized approximately 135 000 *ab initio* points computed at the UCCSD(T)-F12a/aug-cc-pVTZ level and fitted these points using a combination of permutation invariant polynomials and neural network methods (PIP-NN). Their study successfully determined the minima and transition-state structures as well as the relative energies. In 2002, Hashimoto and Iwata examined the potential energy surfaces of hydroxyl radical reactions with methane and ethane using *ab initio* methods.[28] They performed geometry optimizations at the MP2 level applying aug-cc-pVDZ and aug-cc-pVTZ basis sets for the OH + CH_4 system and the aug-cc-pVDZ basis set for ethane. Energy calculations were carried out using MP2, MP4, and CCSD(T) methods for the OH + CH_4 reaction using an aug-cc-pVQZ basis set and for the OH + C_2H_6 reaction using an aug-cc-pVTZ basis set. Their work successfully identified the minima and transition-state structures for both reactions. Rangel and coworkers developed a full-dimensional PES for the OH + C_2H_6 reaction named PES-2020.[29] This surface accurately represents the H-abstraction reaction enabling reliable kinetic and dynamic simulations. Their dynamics study revealed that the ethyl radical in the reaction has significant internal energy.

In my research, I aim to identify the minima and transition states on the potential energy surface of the OH + C_2H_6 reaction with high accuracy using advanced *ab initio* methods. My goal is to perform correction calculations to assess the accuracy of the (T) approximation, evaluate the impact of scalar relativistic effects on the reaction, determine the core correlation correction and account for energy changes due to spin-orbit coupling.

Following the characterization of these stationary points, I plan to develop a full-dimensional potential energy surface to investigate the dynamics of both the initial ground-state and vibrationally-excited-state reactions.

Methylamine (CH_3NH_2) is present in biological systems, where it is involved in metabolic pathways and is a byproduct of protein degradation. In biological contexts, the oxidation of methylamine by OH radicals involves a series of steps that ultimately produce formamide and formaldehyde. Formaldehyde, being highly reactive, can interact with cellular components, potentially altering protein function and enzyme activity. Formamide can influence amino acid metabolism and other cellular processes. Studying the OH + CH_3NH_2 reaction is essential for understanding oxidative stress and its effects on cellular health as modifications induced by radicals can impact enzyme activity, protein structure and overall cellular well-being. In atmospheric chemistry, the reaction between OH radicals and methylamine is important for understanding how methylamine is removed from the atmosphere.[30,31,32] Methylamine is released into the atmosphere from both natural sources such as biomass burning and anthropogenic activities including industrial emissions. The reaction with OH radicals facilitates the degradation of methylamine helping to reduce its concentration and influencing the formation of secondary pollutants such as nitramines and organic nitrates. All in all, by investigating the mechanisms and dynamics of the reaction between hydroxyl radicals and methylamine, we gain important insights into its role across various environments. This understanding enhances our ability to address pollution control challenges and provides deeper insights into biochemical transformations and oxidative stress.

The H-abstraction pathway of the OH + methylamine reaction has been the focus of considerable theoretical investigation, given its role as a major channel in the reaction. This pathway involves two competitive routes: abstraction of hydrogen from the amino group leading to the formation of H_2O and CH_3NH and abstraction from the methyl group resulting in H_2O and CH_2NH_2. Tian and coworkers in 2009 provided a detailed theoretical analysis of these pathways.[33] They used CCSD/6-31G(d) level of theory to determine the geometries and vibrational frequencies of the reactants, pre-reaction minima, transition states, post-reaction complexes and products. To further refine their results, single-point

energy calculations were carried out at the CCSD(T)/6-311++G(2d,2p) level yielding the relative energies of the stationary points along the reaction pathways. They also calculated rate coefficients based on transition state theory. In 2013, Onel and colleagues continued the exploration of the H-abstraction pathway by optimizing the geometries of the stationary points using the MP2 method with aug-cc-pVDZ and aug-cc-pVTZ basis sets.[34] They complemented their work with energy calculations at higher levels employing CCSD(T) and CCSD(T)-F12a methods to provide a more comprehensive understanding of the reaction energetics and mechanisms. Reaction rate coefficients for the H-abstraction channel also were investigated experimentally by Atkinson and coworkers,[35] Carl and Crowley,[36] Butkovskaya and Setzer[37] and Onel and coworkers[38] across a temperature range of 295 to 426.1 K.

Building on the existing theoretical and experimental investigations of the H-abstraction reaction pathways and their associated rate coefficients, my goal is to achieve a significantly more accurate characterization of the stationary points on the potential energy surface of the OH + methylamine reaction considering the same energy corrections like in the case of the OH + C_2H_6 reaction. Furthermore, my research aims to cover not only the previously-examined H-abstraction reaction channel, but also the various substitution product channels. In addition, a comprehensive search for the conformer structures of each transition state and post-reaction complex is conducted. Finally, based on transition state theory, I plan to estimate the rate coefficients for a temperature range of 294-3000 K.

The interaction between hydroxyl radicals and glycine, the simplest amino acid, holds substantial importance in both biochemical and environmental contexts due to the pivotal role of the glycine molecule in protein chemistry and its widespread occurrence in various chemical systems. Glycine is integral to many biological processes including protein synthesis and metabolic pathways. When glycine reacts with OH radicals, it undergoes oxidation that can lead to the formation of several oxidative byproducts. These byproducts can alter the structure and function of proteins making it essential to study this reaction to understand oxidative stress. In the pharmaceutical industry comprehending how glycine reacts with OH radicals is crucial for evaluating the stability of amino acids and their derivatives. This information is valuable for optimizing drug formulations and ensuring the

stability of pharmaceutical products over time. All in all, investigating the mechanisms and dynamics of the reaction between hydroxyl radicals and glycine offers significant insights into its roles across biochemical processes, environmental chemistry and pharmaceutical research.

It is well known that gaseous glycine has 8 conformers[39,40,41,42,43,44,45,46] and this was investigated most accurately by our research group.[47] The conformers are illustrated in **Figure 1**.
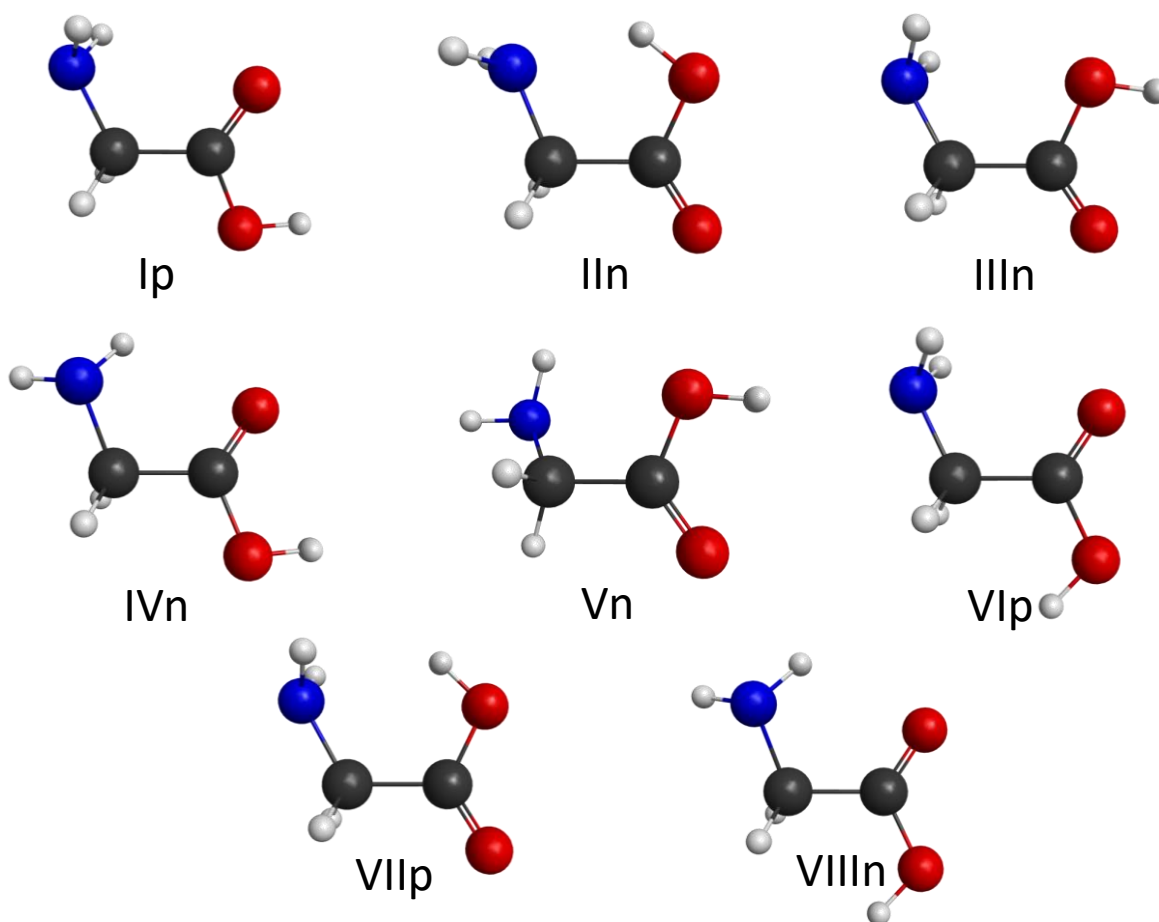
Figure 1. Conformers of glycine determined at the CCSD(T)-F12b/aug-cc-pVDZ level of theory. Adapted from Ref. [3].

In the H-abstraction reaction the hydroxyl radical can abstract a hydrogen atom from different sites of the glycine molecule, specifically from the CH_2, NH_2 and COOH groups. This abstraction results in the formation of dehydrogenated glycine radicals: $H_2N–CH–COOH$, $HN–CH_2–COOH$ and $H_2N–CH_2–COO$. Following the earlier

investigations,[48,49,50,51,52,53,54,55,56,57] our research group made a significant advancement in 2020 by performing a high-level study using explicitly-correlated coupled-cluster and multireference configuration interaction methods.[47] A comprehensive mapping of the conformational space for the dehydrogenated glycine radicals was carried out identifying 4, 7 and 4 conformers for the $H_2N–CH–COOH$, $HN–CH_2–COOH$ and $H_2N–CH_2–COO$ radicals, respectively. The revealed products are shown in **Figure 2**.
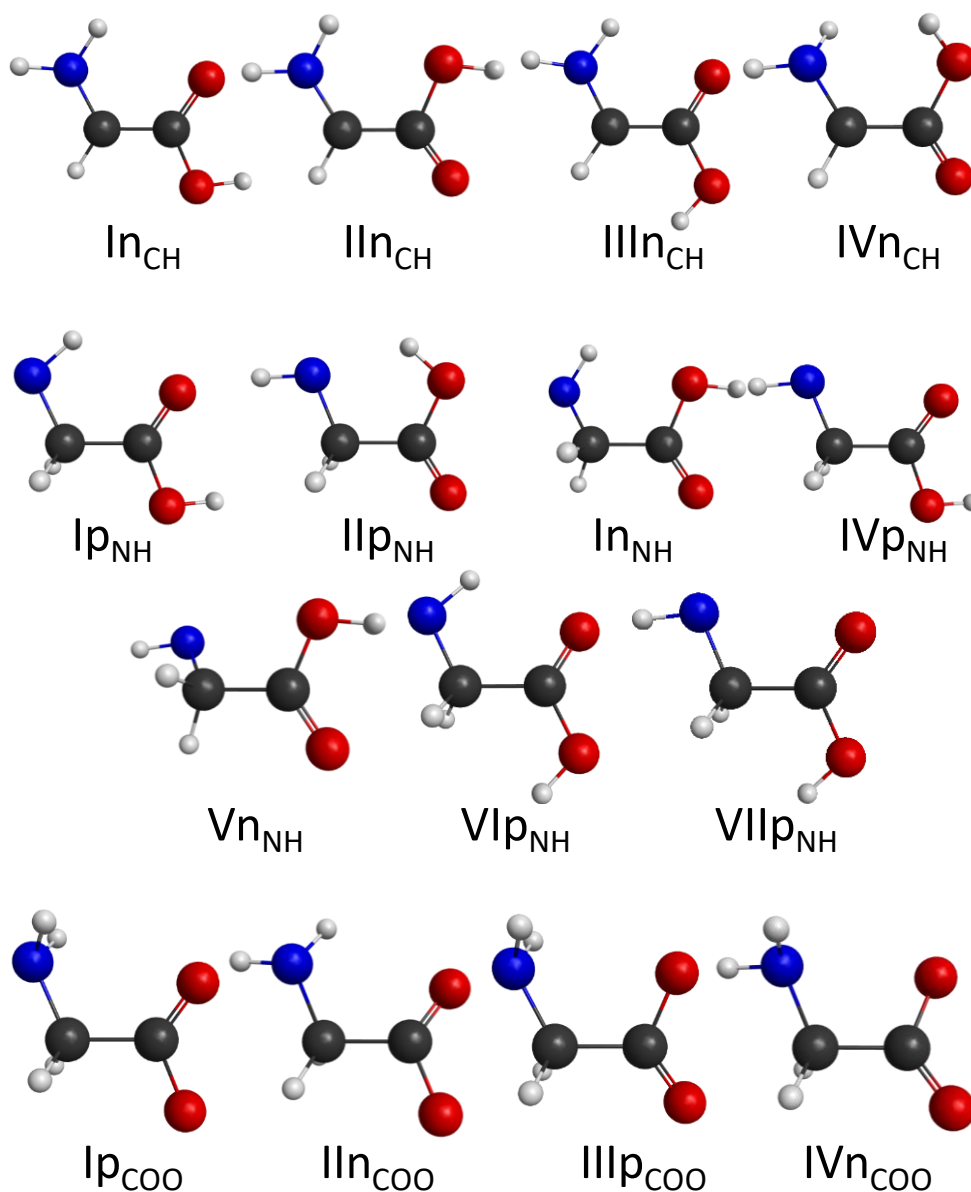
Figure 2. Conformers of the $H_2N–CH–COOH$, $HN–CH_2–COOH$ and $H_2N–CH_2–COO$ radicals determined at the CCSD(T)-F12b/aug-cc-pVDZ, CCSD(T)-F12b/aug-cc-pVDZ and MRCI/aug-cc-pVDZ levels of theory, respectively. Adapted from Ref. [3].

In the literature, the saddle points and minima of the potential energy surface for the OH + glycine H-abstraction reaction are less thoroughly explored. While there are some studies available, they employ relatively low-accuracy quantum chemical methods. For instance, Alvarez-Idaboy and colleagues in 2001 applied density functional theory (DFT) and MP2 methods with double- and triple-zeta Pople-type basis sets to study the C–H abstraction channel identifying a pre-reaction complex and a transition state.[49] Further research by Li and coworkers in 2010 explored two minimum energy pathways for H-abstraction from the carbon center using various DFT functionals, HF and MP2 methods including some single-point energy calculations at the CCSD(T) level.[55]

Expanding on the existing research, which has only partially explored the OH + glycine reaction, my research focuses on a more comprehensive investigation of the hydrogen-abstraction pathways involving the CH_2, NH_2 and COOH groups. Accurate benchmark energies are obtained by incorporating corrections for the effects of the post-(T) correlation, scalar relativity, core correlation, and spin-orbit coupling. Additionally, I plan to develop a full-dimensional, analytical potential energy surface with coupled-cluster accuracy. A key aspect of my work is conducting quasi-classical trajectory (QCT) simulations to investigate the reaction dynamics that has not been explored in the literature until now.

2 THEORETICAL BACKGROUND

2.1 BORN−OPPENHEIMER APPROXIMATION

In quantum mechanics, the physical-chemical properties of a chemical system are described with the Schrödinger equation:

$$\hat{H}_{\text{tot}}\psi = E_{\text{tot}}\psi, \tag{1}$$

where $\hat{H}_{\text{tot}}$ is the total energy operator called Hamiltonian operator, E_{tot} is the total energy, and ψ is the wave-function of the system. In the abscenece of external forces the non-relativistic Hamiltonian operator of a molecular system considers the followings: the kinetic energy of the electrons and nuclei, the attraction between the nuclei and electrons, the repulsion between the electrons and the repulsion between the nuclei. The exact, analytic solution of the molecular Schrödinger equation exists only for the hydrogen atom, because the mathematical description becomes simpler in this case as the internal interactions of the atom are limited to the electrostatic attraction between the electron and the nucleus, thus the electron-electron and nucleus-nucleus interaction terms are omitted. If the system contains more than one electron, the application of approximations is essential for solving the Schrödinger equation. Through the Born−Oppenheimer separation (BO), we handle the motion of nuclei and electrons independently.[58] This can be accomplished, because the electrons nearly instantaneously follow the motion of the nuclei as nuclei are orders of magnitude heavier than electrons. Thus, using the BO approximation the wave function can be expressed as a product of functions containing only electronic coordinates (ψ_{e}) and only nuclear coordinates (ψ_{n}):

$$\psi = \psi_{\text{e}}(1,2,\dots,n)\psi_{\text{n}}(1,2,\dots,N), \tag{2}$$

where $(1,2,\dots,n)$ denotes the coordinates of the electrons and $(1,2,\dots,N)$ signifies the coordinates of the nuclei. Based on these, the Schrödinger equation can be obtained in the following form:

$$\left(\hat{H}_{\text{e}} + \hat{T}_{\text{n}}\right)\psi_{\text{e}}\psi_{\text{n}} = (E_{\text{e}} + E_{\text{n}})\psi_{\text{e}}\psi_{\text{n}}, \tag{3}$$

where $\widehat{H}_e$ operator includes the kinetic energy operator of electrons and all potential energy terms and $\widehat{T}_n$ is the kinetic energy operator of nuclei. E_e and E_n represents the energies of electrons and nuclei, respectively. After performing the appropriate mathematical operations, we arrive to the following two time-independent equations:

$$\widehat{H}_e \psi_e = E_e \psi_e, \tag{4}$$

$$(\widehat{T}_n + E_e)\psi_n = E\psi_n, \tag{5}$$

The first equation provides the Schrödinger equation for the motion of the electrons, while the second one pertains to the motion of the nuclei, where the electronic energy E_e depends on the positions of the nuclei.

2.2 QUANTUM CHEMICAL METHODS

As discussed in the previous chapter (2.1), utilizing the BO approximation enables us to formulate two equations: one pertaining to the electrons and one concerning the nuclei, thus dividing the field of quantum chemistry into two parts: electron structure and nuclear motion calculations. In this chapter, we can read about methods by which solving the time-independent Schrödinger equation for electrons allows us to obtain the energies of atoms and molecules and their associated wave functions.

2.2.1 Hartree−Fock method

The Hartree−Fock method (HF) is based on the so-called independent particle approximation. The basis of this concept lies in approximating the wave function, which depends on the coordinates of n electrons as a product of single-electron functions as follows:

$$\psi(1,2,\dots n) \approx \psi_1(1)\psi_2(2)\dots\psi_n(n), \tag{6}$$

where ψ_i is a single-electron wave function depending only on the coordinates of the i-th electron. However, the product form written in this way does not satisfy the axiom of quantum mechanics, which states that if we exchange the coordinates of two electrons, the sign of the wave function changes. Therefore, the wave function is expressed in determinant form since if we exchange two columns of the determinant, i.e., two electrons,

the value of the determinant changes sign. The determinant constructed from single-electron functions (ϕ) is called Slater-determinant:

$$\phi = \frac{1}{\sqrt{n!}} \begin{bmatrix} \varphi_1(1) & \cdots & \varphi_1(n) \\ \vdots & \ddots & \vdots \\ \varphi_n(1) & \cdots & \varphi_n(n) \end{bmatrix}, \tag{7}$$

where n is the number of electrons. The HF energy can be calculated by taking the expectation value of the Hamiltonian operator ($\widehat{H}_e$) with the previously written Slater-determinant (ϕ):

$$E_{\mathrm{HF}} = \langle \phi | \widehat{H}_e | \phi \rangle. \tag{8}$$

Based on the number of electron coordinates involved in its terms, the Hamiltonian operator can be divided into three parts:

$$\widehat{H}_e = \widehat{h}_0 + \widehat{h}_1 + \widehat{h}_2, \tag{9}$$

where $\widehat{h}_0$ is the zero-electron operator, which represents the nucleus-nucleus repulsion, $\widehat{h}_1$ is the one-electron operator including the kinetic energy and the nucleus-electron attraction and $\widehat{h}_2$ is the two-electron operator describing electron-electron repulsion. In fact, it is the $\widehat{h}_2$ operator that complicates the solution of the Schrödinger equation as it couples the motion of electrons. The HF method approximates the $\widehat{h}_2$ term as if each electron was moving in some average potential field created by the others. Utilizing the Slater-Condon rules, the energy expression can be formulated in the following manner:

$$E_{\mathrm{HF}} = E_0 + \sum_{i=1}^{n} H_{ii} + \frac{1}{2} \sum_{i=1}^{n} \sum_{j=1}^{n} (J_{ij} - K_{ij}), \tag{10}$$

where E_0 is a constant arising from nucleus-nucleus repulsion, H_{ii} denotes the one-electron integral, J_{ij} represents the Coulomb integral and K_{ij} is the exchange integral. It can be seen that the HF energy can be expressed in terms of one-electron functions meaning that the energy depends on the choice of one-electron functions (φ) within the determinant. The variational principle plays an important role in the proper selection of one-electron functions, which states that the energy calculated with any approximate wave function is guaranteed to be greater than or equal to the exact energy. Equality occurs when the wave function is not an approximation but precisely the exact wave function. The

consequence of the variational principle is that when approximate wave functions are randomly chosen and the energy is calculated with them, without knowing the exact energy, we can still determine which is the best energy, since it cannot go below the exact energy; therefore, the one that is the smallest will be the closest to the exact one. Therefore, according to the variational principle, we seek those one-electron functions within the Slater determinant that yield the deepest energy. Mathematically formulated, the energy, which is a functional of the one-electron functions $E[\boldsymbol{\phi}]$, needs to be minimized. As a result of this minimization procedure, the so-called canonical Hartree−Fock equation emerges as follows:

$$\hat{F}(i)\varphi_i = \varepsilon_i\varphi_i, \tag{11}$$

where $\hat{F}$ denotes the Fock operator, φ_i represents the sought one-electron functions, referred to as orbitals and ε_i is the orbital energy associated with the φ_i orbital. The Fock operator can be written in the following form:

$$\hat{F}(i) = \hat{h}_1(i) + \sum_{j=1}^{n}\langle\varphi j(j)|\hat{h}_2(ij)(1 - \hat{P}_{ij})\varphi j(j)\rangle, \tag{12}$$

where $\hat{h}_1$ is the one-electron operator:

$$\hat{h}_1 = -\frac{\hbar^2}{2m}\nabla_i^2 - \sum_j\frac{e^2 Z_j}{r_{ij}}, \tag{13}$$

where m denotes the mass of the electron, ∇ is the nabla operator, Z represents the nuclear charge and r_{ij} indicates the distance between the nucleus and electron. $\hat{h}_2$ is the two-electron operator:

$$\hat{h}_2 = \frac{e^2}{r_{ij}}, \tag{14}$$

where r_{ij} represents the electron-electron distance. In **Equation 12** $\hat{P}_{ij}$ denotes the operator that exchanges the i-th and j-th electrons. At this point, it is important to notice that while the Fock operator depends only on the coordinate of one electron, orbitals of all electrons are included in the summation term, therefore the Fock operator depends on all the orbitals. A vicious circle has emerged, as the Fock operator cannot be written without knowledge of the orbitals, yet the orbitals can only be obtained by solving the eigenvalue equation of the Fock operator. This problem can be addressed by applying the self-

consistent field (SCF) method. By utilizing this iterative solution, initial $\varphi(0)$ functions are assumed, thus building the Fock operator and then solving the Hartree−Fock equations to obtain a new set of φ_i functions is possible. From these, a new Fock operator can be constructed and the process is repeated until a convergent result is achieved which means that the energies (ε) and the orbitals (φ) change only very slightly. After determining the orbitals, the HF energy can be obtained based on **Equation 10**.

2.2.2 Hartree−Fock−Roothan method

The eigenvalue equation of the Fock operator itself is a complex differential equation, which lacks an analytical solution. Therefore, we employ an approximate, numerical procedure known as the Hartree−Fock−Roothan (HFR) method, within which the one-electron orbitals (φ) are expanded in a series of basis functions (χ) as follows:

$$\varphi_i = \sum_{m=1}^{M} c_{im} \chi_m, \tag{15}$$

where $\mathbf{c}$ represents the expansion coefficients and M denotes the number of basis functions. Substituting this formula into the eigenvalue equation of the Fock operator, the following matrix eigenvalue equation can be obtained for each electron:

$$\mathbf{F}\mathbf{c}_i = \varepsilon_i \mathbf{S}\mathbf{c}_i, \tag{16}$$

where $\mathbf{F}$ is the Fock matrix, $\mathbf{S}$ is the overlap matrix, $\mathbf{c}$ contains the expansion coefficients and ε remains the orbital energy. It is important to mention that transitioning from the differential equation to matrix eigenvalue equations is an approximation, so the exact energy is not attainable (except in the case of an infinite matrix, i.e., when an infinite number of basis functions are used). However, with the appropriate selection of basis functions, accurate results can be obtained. Since the elements of the Fock matrix depend on all the orbitals and the orbitals are obtained as linear combinations of basis functions, meaning the Fock matrix ($\mathbf{F}$) depends on the expansion coefficients ($\mathbf{c}$). Therefore, the use of the SCF procedure is necessary in this case as well. In this case, initial $\mathbf{c}$ coefficients are assumed. Plugging these into **Equation 15** gives us the orbitals allowing us to construct the Fock operator. Subsequently, the matrix elements of the Fock matrix ($\mathbf{F}$) can be computed and by solving the eigenvalue equation of the Fock matrix, new $\mathbf{c}$ coefficients are obtained.

These steps are repeated iteratively until the $\mathbf{c}_i$ coefficients and ε_i orbital energies converge within a certain threshold.

2.2.3 Basis sets

In the manner discussed in the previous section, the orbitals are treated as linear combinations of basis functions. Two main types of orbitals are typically distinguished: Slater (STO) and Gaussian (GTO) types. The Slater-type orbitals can be expressed in the following form:

$$\chi_{l,m,n}^{\mathrm{STO}}(r,\zeta) = N x^l y^m z^n e^{-\zeta r}, \tag{17}$$

and the Gaussian orbitals can be described as:[59]

$$\chi_{l,m,n}^{\mathrm{GTO}}(r,\xi) = N x^l y^m z^n e^{-\xi r^2}, \tag{18}$$

where ζ, ξ are the STO and GTO orbital coefficients, N is the normalization factor, and l, m, n are parameters. The exact wave functions must satisfy Kato's cusp condition, which states that the derivative of the electron density function (ρ) at the nucleus ($r = 0$) must be proportional to the atomic number (Z) and not equal to zero:

$$\left.\frac{\partial \rho(r)}{\partial r}\right|_{r=0} = -2Z\rho(0), \tag{19}$$

This requirement is only fulfilled by STOs making STOs much more realistic. However, in practice, GTOs have become prevalent because integrals formed with them are easier to compute compared to using STOs. This is explained by the fact that the product of two Gaussian functions with different centers remains Gaussian. The accuracy of STOs can be approached by taking the linear combination of multiple Gaussian functions, which are referred to as contracted bases:

$$\chi^{\mathrm{STO}} = \sum_{i=1}^{k} c_i \chi_i^{\mathrm{GTO}}, \tag{20}$$

where k is the contraction rate and c_i is the contraction coefficient. The simplest case of the contracted basis sets is known as STO-nG bases, where n denotes the number of utilized primitive GTOs. It is worth noting that no matter how many Gaussian functions are linearly

combined, they will not reproduce the sharp peak characteristic of STOs at $r = 0$. However, this method can approximate the shape of STOs well.

The split valence basis sets are attributed to Pople,[60,61] wherein the inner shell is described by a linear combination of Gaussian functions, while the valence shell orbitals are divided into multiple parts. Depending on the number of basis function sets assigned to the valence shell orbitals, double (DZ), triple (TZ), quadruple (QZ), etc. zeta quality orbitals are distinguished. As an illustration, the 6-31G notation indicates that the inner shells of each atom are constructed using six primitive Gaussian functions. Meanwhile, the valence shell, characterized as DZ quality, is made up from a set of orbitals comprising three primitive Gaussian functions alongside another set containing one primitive Gaussian function. The basis functions can be augmented with polarization functions, which represent higher angular momentum orbitals. For example, in the case of nitrogen atom, when polarization functions are used, not only s and p type orbitals are employed, but also d type orbitals are included in the basis set. Moreover, the basis functions can be extended with diffuse functions, which represent functions with small exponents meaning they decay slowly. These slowly decaying functions are crucial in describing long-range interactions such as hydrogen bonding, dispersion interactions and characterizing molecular complexes or in the case of anions, where there is one additional electron in the system compared to the neutral form resulting in a significantly more diffuse electron cloud.

The creation of the most modern basis sets is attributed to Dunning.[62,63,64] These are the correlation-consistent basis sets, built from a series of polarization functions and their greater accuracy is achieved by utilizing orbitals of increasing angular momentum rather than solely using polarization functions of the same angular momentum. These bases are represented by the abbreviations cc-pVNZ, where "cc" stands for correlation-consistency, "p" signifies the incorporation of polarized functions, "N" indicates the use of symbols D (double), T (triple), etc., representing the extent of splitting and "Z" refers to zeta. Dunning's bases can be enhanced with diffuse functions as well, in which the prefix "aug-" is added to the abbreviation (aug-cc-pVNZ).[65]

2.2.4 Correlation consistent methods

If a quantum system contains more than one electron, the HF method will never be accurate, because it incorporates various approximations. From a mathematical perspective, the problem arises from seeking the wave function in a single determinant form, which is not a good approximation for systems with more than one electron. From a physical aspect, the problem with the HF approximation is that it assumes each electron moves in the average potential field created by the others neglecting the coordinated motion of electrons, where the movement of one electron influences the movement of another that is known as correlated motion. In order to improve upon the HF method, several methods have been developed, known as correlation methods, which are discussed concisely in this section.

2.2.4.1 Excited determinants

The essence of correlation methods is to define so-called excited determinants, which can be originated from the HF determinant (ϕ_0) in the following manner:

$$\phi_0 = \frac{1}{\sqrt{n!}} \begin{vmatrix} \varphi_1(1) & \dots & \varphi_1(n) \\ \vdots & & \vdots \\ \varphi_i(1) & \dots & \varphi_i(n) \\ \vdots & & \vdots \\ \varphi_n(1) & \dots & \varphi_n(n) \end{vmatrix} \rightarrow \phi_i^a = \frac{1}{\sqrt{n!}} \begin{vmatrix} \varphi_1(1) & \dots & \varphi_1(n) \\ \vdots & & \vdots \\ \varphi_a(1) & \dots & \varphi_a(n) \\ \vdots & & \vdots \\ \varphi_n(1) & \dots & \varphi_n(n) \end{vmatrix}, \qquad (21)$$

where ϕ_0 represents the HF wave function, n stands for the number of electrons in the system, i indicates an occupied orbital and a denotes a virtual orbital. How exactly are the occupied and virtual orbitals obtained and how is the excited determinant constructed from them? Considering the HFR method, the dimension of the Fock matrix matches the number of basis functions and the orbitals are derived from the eigenvalue equation of the Fock matrix. However, since more basis functions are generally employed than the number of electrons in the system, more orbitals are obtained than the number of electrons present. Thus, in the HF determinant, the lowest-energy n orbitals are filled, which are referred to as occupied orbitals, while the remaining ones are called virtual orbitals. The excited determinant is formed by replacing the i-th occupied orbital with the a-th virtual orbital. The number of occupied orbitals replaced with virtual ones determines the distinction between singly, doubly, triply, etc. excited determinants. It is important to note

20

that the excitation here is not a physical process but rather a mathematical operation, thus an excited determinant does not necessarily represent an excited state.

2.2.4.2 Configuration Interaction method

One type of variational method is the configuration interaction (CI) method,[1] where the exact wave function is approximated by a linear combination of excited determinants as follows:

$$\phi_{\mathrm{CI}} = c_0\phi_0 + \sum_i \sum_a c_i^a \phi_i^a + \sum_i \sum_{j>i} \sum_a \sum_{b>a} c_{ij}^{ab} \phi_{ij}^{ab} + ..., \tag{22}$$

where c_0, c_i^a, c_{ij}^{ab} are the coefficients of the expansion that are obtained variationally. The series expansion seen here, however, does not extend infinitely as the possible number of excitations is constrained by the number of occupied orbitals, which corresponds to the number of electrons. So, for example, if we wanted to perform calculations for a 10-electron system (water molecule), the series expansion would stop at the level of tenfold excited determinants. The CI energy (E_{CI}) itself is derived by taking the expectation value of the Hamiltonian operator with the wave function (ϕ_{CI}) written in the previous form:

$$E_{\mathrm{CI}} = \langle \phi_{\mathrm{CI}} | \widehat{H} | \phi_{\mathrm{CI}} \rangle. \tag{23}$$

A practical solution involves a matrix eigenvalue equation, which can be written with the following expression:

$$\mathbf{Hc} = E_{\mathrm{CI}}\mathbf{c}, \tag{24}$$

where $\mathbf{H}$ denotes the matrix representation of the Hamiltonian operator in the basis of excited determinants and $\mathbf{c}$ is the row vector of expansion coefficients. However, a challenge emerges with the $\mathbf{H}$ matrix potentially growing exceedingly large making it impractical to consider all potential excited determinants even with modern computing power. Even for relatively small systems like water with just 10 electrons, the sheer number of possible excited determinants can be so immense that it becomes unfeasible to handle. As a result, the series expansion is typically truncated and depending on the number of occupied orbitals replaced with virtual ones, i.e., how many excited determinants are considered, we distinguish CI, CIS, CISD, CISDT, etc. methods, where S represents single, D double, T triple and so forth. In a given basis, exact energy can be obtained through the so-

called full-CI (FCI) calculation, as in this case, the entire CI series, meaning all possible excited determinants, is taken into account. For instance, in a system with 2 electrons, FCI aligns with the CISD method, while for a 3-electron system, it corresponds to CISDT and so on. A major drawback of the CI method is its lack of size consistency. The size consistency problem means that when the energies of individual non-interacting systems are determined separately and added up, the same result is not obtained as when the calculation is performed for the entire system. This discrepancy poses a significant problem in chemical applications, which is why the use of the CI method is not common in practice.

2.2.4.3 Møller−Plesset perturbation theory

Within the perturbation theory, the Hamiltonian operator ($\widehat{H}$) is divided into two parts: reference operator ($\widehat{H}^0$) and perturbation operator ($\widehat{W}$):[66,67]

$$\widehat{H} = \widehat{H}^0 + \lambda \widehat{W}, \tag{25}$$

where λ is the perturbation parameter. The $\widehat{H}^0$ reference operator is chosen so that its eigenvalue problem can be solved relatively easily, thus using the eigenvalues and eigenfunctions of $\widehat{H}^0$, a small energy correction can be calculated for the perturbative term. Both the wave function (ψ) and the energy (E) can be expressed as a power series in λ:

$$\psi = \psi^{(0)} + \lambda \psi^{(1)} + \lambda^2 \psi^{(2)} + \cdots, \tag{26}$$

$$E = E^{(0)} + \lambda E^{(1)} + \lambda^2 E^{(2)} + \cdots, \tag{27}$$

Depending on which power of λ we consider, we can distinguish first-, second- and so on, order perturbations. In the case of the Møller−Plesset perturbation method, the reference operator ($\widehat{H}^0$) is defined as the sum of the Fock operators ($\widehat{F}$):

$$\widehat{H}^0 = \sum_{i=1}^n \widehat{F}_i, \tag{28}$$

where n means the number of electrons. Thus, the perturbing operator ($\widehat{W}$) is the difference between the zeroth-order ($\widehat{H}^0$) and the exact Hamiltonian operator ($\widehat{H}$). Based on the order of the perturbation parameter (λ) in the Møller−Plesset separation, we can distinguish methods like MP0, MP1, MP2 and so on. MP0 simply provides the sum of orbital energies, while MP1 yields the HF energy itself making these two methods not practically

useful. MP2, on the other hand, is a widely used method that adds the following energy correction to the HF energy:

$$E^{(2)} = \sum_{i<j} \sum_{a<b} \frac{\left|\left\langle \Phi_{ij}^{ab} \middle| \widehat{W} \middle| \Phi^{(0)} \right\rangle\right|^2}{\varepsilon_a + \varepsilon_b - \varepsilon_i - \varepsilon_j}, \tag{29}$$

where ε_i and ε_j denote the energies of the occupied orbitals and ε_a and ε_b represent the energies of the virtual orbitals. The doubly-excited Φ_{ij}^{ab} determinant in the numerator is obtained by exchanging two occupied orbitals (i and j) with two virtual orbitals (a and b). Higher-order methods such as MP3, MP4, etc., are not commonly used due to their high computational costs. Calculating this energy correction does not significantly increase the computation time compared to HF, yet it describes approximately 90% of the correlation energy providing much more accurate energy than HF. For open-shell systems, we can apply the so-called restricted (RMP2) and unrestricted (UMP2) MP2 methods. In the RMP2 approach, electrons are paired with opposite spins (α or β) in spatial orbitals. In the UMP2 method, however, each orbital can accommodate only one electron.

2.2.4.4 Coupled Cluster theory

The most accurate single-reference approximate method, which is not fully variational, is the so-called coupled cluster method (CC).[68,69,70] Within the CC procedure, the energy of the system is sought by applying an operator ($e^{\widehat{T}}$) to the HF wave function (Φ_{HF}) approximating the exact wave function with this new function (ψ_{CC}):

$$\psi_{\text{CC}} = e^{\widehat{T}} \Phi_{\text{HF}}, \tag{30}$$

where $\widehat{T}$ is the so-called excitation operator, which is the sum of $\widehat{T}_1 + \widehat{T}_2 + \cdots$ operators, where if $\widehat{T}_1$ acts on the HF determinant, then all singly-excited determinants are generated; if $\widehat{T}_2$ acts, then all doubly-excited determinants are generated and so forth. Based on the excitation levels considered in the $\widehat{T}$ operator, we can distinguish methods like CCSD ($\widehat{T}_1 + \widehat{T}_2$), CCSDT ($\widehat{T}_1 + \widehat{T}_2 + \widehat{T}_3$) and so on. Expanding the operator $e^{\widehat{T}}$ in a Taylor series, we can describe its effect in the following manner:

$$e^{\widehat{T}} = \left(1 + \widehat{T} + \frac{1}{2}\widehat{T}^2 + \frac{1}{3!}\widehat{T}^3 \dots\right) = \left(1 + \widehat{T}_1 + \widehat{T}_2 + \frac{1}{2}\widehat{T}_1^2 + \widehat{T}_3 + \widehat{T}_1\widehat{T}_2 + \frac{1}{3!}\widehat{T}_1^3 + \cdots\right). \tag{31}$$

Taking a closer look at the expansion, we can notice that even if we truncate the series at a certain point, higher-order excitations still emerge. For example, in the case of the CCSD method, which considers only single and double excitations in the $\hat{T}$ operator, triple and quadruple excitations also arise. This is the source of the power of the CC method, enabling it to deliver significantly more precise results than any preceding methods (HF, CI, MP). A special case is the CCSD(T) method,[71,72,73] when we consider the excitation operators $\hat{T}_1$ and $\hat{T}_2$, while the (T) term implies that the triple excitations are calculated using perturbative approximations. With the explicitly-correlated F12 method,[74,75] where an exponential function of electron-electron distances is utilized, we can obtain even more accurate results. The CCSD(T)-F12b method has a significant advantage that it can provide more precise results even with lower-level basis sets compared to using the CCSD(T) method, while the required computational time is not significantly higher.

2.3 BASICS OF THE QUANTUM CHEMICAL GEOMETRY OPTIMIZATION

One cornerstone of my work is the identification of structures associated with stationary points (minima and saddle points) on the potential energy surfaces of the investigated reactions. The search and optimization of these structures are based on the Newton−Raphson method, whose fundamental idea is to iteratively refine the result from an initial approximation until the desired accuracy is achieved. In quantum chemical geometry optimization, the initial approximation is provided by specifying a structure that closely resembles the one we want to identify. In the optimization process, the gradient of the potential energy surface along a coordinate ($\mathbf{g}(\mathbf{x})$) can be defined as follows:

$$\mathbf{g}(\mathbf{x}) = \mathbf{g}_0 + \mathbf{H}_0 \Delta\mathbf{x}, \tag{32}$$

where $\mathbf{H}_0$ is the Hessian matrix, $\mathbf{g}_0$ denotes the value of the function calculated at point 0 and $\Delta\mathbf{x}$ represents the magnitude of the displacement. We reach a stationary point when $\mathbf{g}(\mathbf{x}) = \mathbf{0}$. Based on these, the displacement at a given point or the so-called Newton−Raphson step is obtained as follows:

$$\Delta\mathbf{x} = -\mathbf{H}_0^{-1}\mathbf{g}_0, \tag{33}$$

During my work, some variations of the previously introduced Newton−Raphson method were applied: the QSD (Quadratic Steepest Descent) method[76] was used for locating transition states and the RF (Rotational Function) method[77] was employed for finding minima.

2.4 VIBRATIONAL FREQUENCY CALCULATION

In this chapter, the significance of frequency calculation is discussed first followed by a brief overview of the theoretical background of such calculations. On one hand, in quantum chemical calculations, the potential energy arising from electron motion, referred to as classical energy, is first determined using one of the methods described earlier. Following this, the zero-point energy (ZPE) is obtained through frequency calculations serving as a correction. The resultant combined energy is denoted as adiabatic energy. On second hand, frequency calculation is crucial for mapping the topology of potential energy surfaces as it determines the nature of the identified stationary points. From chemical perspective, the minima and first-order saddle points of the potential energy surfaces are the most important as the minima represent the stable conformations of molecules, while the first-order saddle point characterizes a transition state of a reaction and outline the pathway of its progression. During a reaction, the first-order saddle point serves as the maximum energy when transitioning between two minima, but it represents the minimum energy from all other directions.

To characterize the stationary points, normal mode analysis is performed to determine their vibrational frequencies and zero-point energies. This involves calculating the frequency (v_i) of each normal mode using the following expression:

$$v_i = \frac{\sqrt{\lambda_i}}{2\pi}. \tag{34}$$

In this context, λ_i represents the i-th eigenvalue of the transformed Hessian matrix, where i ranges from 1 to $3N - 6$ for a non-linear molecule or $3N - 5$ for a linear molecule with N atoms. Consequently, a transition state or first-order saddle point is characterized by a single imaginary frequency, which arises from the presence of a negative eigenvalue.

In reality, the vibrations of molecules are not purely harmonic. For determining thermodynamic data, as I have done, the harmonic approximation can be considered sufficient as its error is comparable with other applied methods. Additionally, the computational time significantly increases considering anharmonicity, hence employing an anharmonic approach is only justified when indispensable, for instance, in forecasting spectral data.

2.5 TRANSITION-STATE THEORY

Using the barrier heights, vibrational frequencies and rotational constants obtained from the computations, it becomes possible to determine the reaction rate coefficients based on transition state theory (TST). Within this theoretical framework, the rate coefficient (k_{TST}) for a bimolecular reaction is calculated utilizing the following expression:

$$k_{TST} = \left(\frac{k_B T}{h}\right)\left(\frac{Q_{TS}}{Q_{reactant,1}Q_{reactant,2}}\right) exp\left(\frac{-\Delta E}{RT}\right), \tag{35}$$

where k_B denotes the Boltzmann constant, T represents the temperature, h is the Planck constant, Q_{TS} stands for the total partition function of the transition state, $Q_{reactant,1}$ and $Q_{reactant,2}$ refer to the total partition functions of the respective reactants, ΔE is the reaction barrier height and R is the universal gas constant. The total partition function (Q_{total}) for each species is given by the following formula:

$$Q_{total} = Q_{trans}Q_{rot}Q_{vib}Q_{elec}, \tag{36}$$

where Q_{trans} denotes the translational component of the partition function, Q_{rot} signifies the rotational contribution, Q_{vib} accounts for the vibrational contribution and Q_{elec} represents the electronic contribution to the overall partition function. It is important to highlight that for atoms the rotational and vibrational contributions are 1, since atoms do not exhibit rotational or vibrational motion. The translational contribution can be calculated as follows:

$$Q_{trans} = \frac{(2\pi m k_B T)^{3/2}}{h^3}, \tag{37}$$

where h represents the Planck constant, m denotes the mass of the species, k_B is the Boltzmann constant and T is the temperature. The method for calculating the rotational

contribution to the partition function differs based on whether the molecule is linear or non-linear. For linear molecules, the contribution is determined using the following formula:

$$Q_{\text{rot,linear}} = \frac{k_{\text{B}}T}{\sigma hcB},\qquad(38)$$

where k_{B} represents the Boltzmann constant, T denotes the temperature, σ is the symmetry number, h stands for the Planck constant, c is the speed of light and B indicates the rotational constant of the molecule. For non-linear molecules, the rotational contribution is given by the following expression:

$$Q_{\text{rot,nonlinear}} = \left(\frac{k_{\text{B}}T}{h}\right)^{3/2}\left(\sqrt{\frac{\pi}{ABC}}\right)\left(\frac{1}{\sigma}\right),\qquad(39)$$

where A, B, and C correspond to the three rotational constants of the molecule. The vibrational contribution of molecules to the total partition function can be calculated using the following expression:

$$Q_{\text{vib}} = \prod_i \frac{1}{1-exp(\beta hc\nu_i)},\qquad(40)$$

where ν_i corresponds to the vibrational frequency of the i-th vibrational mode. The parameter β can be expressed as:

$$\beta = \frac{1}{k_{\text{B}}T}.\qquad(41)$$

Finally, the electronic contribution to the total partition function is given by the following formula:

$$Q_{\text{elec}} = \sum_i g_i exp\left(-\frac{\varepsilon_i}{k_{\text{B}}T}\right),\qquad(42)$$

where g_i represents the degeneracy of the i-th energy level and ε_i denotes the energy of the i-th energy level. While TST offers a valuable estimate for the rate coefficient, it relies on several simplifying assumptions that may limit its accuracy. These assumptions include the presumption that the transition state and the reactants are in a state of thermodynamic equilibrium. This means that TST assumes that the transition state is rapidly established and remains in constant equilibrium with the reactants, which may not always hold in real

27

reactions. Another limitation of the TST model is the assumption that once the transition state is reached, there is no possibility of reverting to the reactant state. This simplification implies a one-way progression from reactants to products without considering the possibility of recrossing or the dynamic nature of the transition state. This assumption may not accurately reflect the behavior of systems where recrossing of the transition state or backward reactions are significant. Additionally, TST generally neglects quantum mechanical effects such as tunneling, which can significantly impact the reaction rate. To address the limitation related to tunneling, the so-called Wigner correction can be applied. This correction accounts for quantum mechanical tunneling effects based on the imaginary frequency associated with the reaction mode. The Wigner correction modifies the TST rate coefficient by incorporating an adjustment factor that reflects the probability of tunneling through the energy barrier. The correction (χ) is expressed as:

$$\chi = 1 + \frac{1}{24}\left(\frac{h|\nu^{im}|}{k_B T}\right)^2,$$

(43)

where ν^{im} denotes the imaginary frequency of the transition state. This adjustment provides a more accurate rate coefficient by incorporating the effects of tunneling, which are initially overlooked by TST.

2.6 POTENTIAL ENERGY SURFACE DEVELOPMENT

Applying the previously-discussed Born−Oppenheimer approximation, quantum chemistry can be divided into two parts: electronic structure calculations and nuclear motion calculations.[78] These two areas are closely related, because within the framework of electronic structure calculations solving the electronic Schrödinger equation for many fixed nuclear configurations allows us to obtain the potential energy surfaces (PESs) of chemical systems. These surfaces are essential, for example, for studying the dynamics of reactions as the negative gradient of the potential energy provides the force that moves the nuclei as the reaction progresses in a classical picture. This chapter (2.6) provides an overview of the methodology employed for PES developments during my research followed by a discussion of reaction dynamics simulations in the next chapter (2.7).
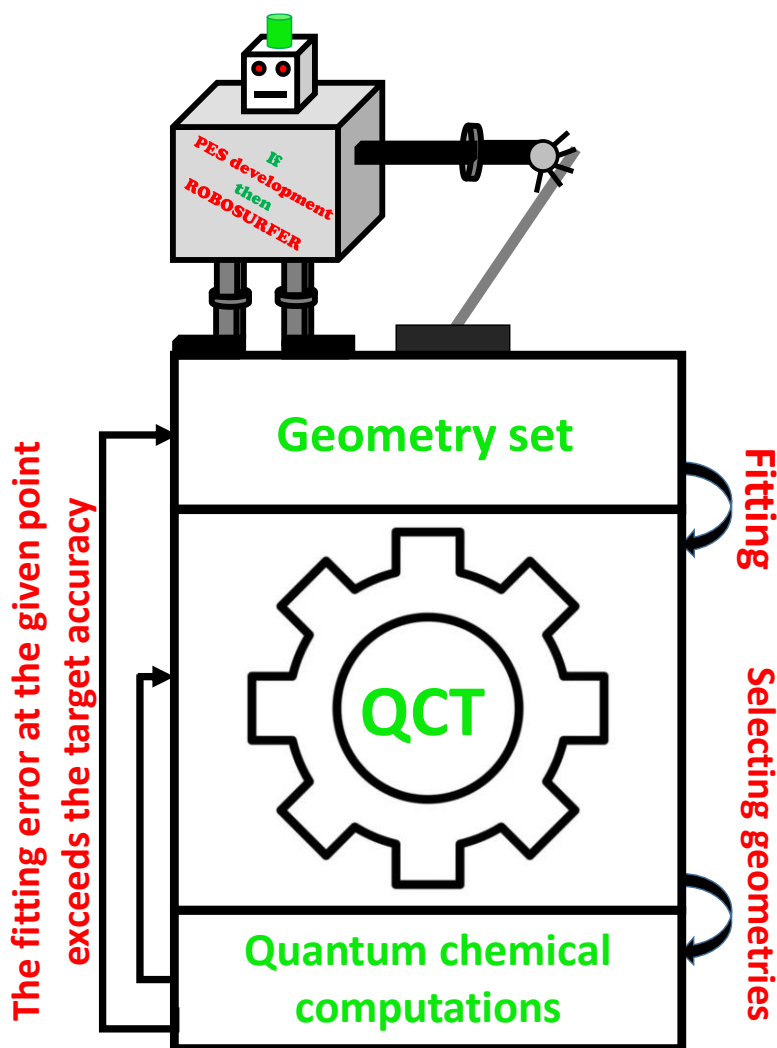
Figure 3. The basic processes of the ROBOSURFER program.

During my research, the development of PESs are carried out using the ROBOSURFER program package,[79] which iteratively repeats the following subprocesses step by step to facilitate the construction of a high-quality PES from an initial set of geometries: 1) fitting energy points corresponding to various nuclear configurations with a function, 2) running dynamic simulations, 3) selecting geometries that contribute the most to the development of the PES, 4) performing quantum chemical calculations at these structures and 5) adding energy points to the initial set. **Figure 3** represents the basic operation of the ROBOSURFER program. Before initiating PES development, the structures corresponding to the key stationary points of the reaction are determined. An initial set of geometries is obtained by randomly displacing the specified structures and for reactants and products, the individual species are scattered randomly around each other. Following this, the potential energy is

computed for each structure by selecting the most appropriate theoretical level for the given system. The potential energy surface itself is represented by an analytical function, which can be obtained by fitting the energy points. When choosing the appropriate functional form one must consider the physical properties of the PES, specifically the fact that the potential energy remains unchanged under translation, rotation or permutation of identical atoms. The first two conditions can be fulfilled by choosing a suitable internal coordinate system as the atom-atom distances, bond angles, and torsional angles do not change under the translation or rotation of the entire system. The permutation-invariance property of the potential energy is crucial because without it, we would obtain potential energy surfaces where dynamics simulations would show different reactivity for chemically equivalent atoms (e.g., the hydrogens in CH_4). This requirement is also satisfied (along with the previous two) by the so-called permutationally invariant polynomial (PIP) method, thus in my research, fitting the energy points during PES development is done using this method. Within the framework of the PIP method, we use so-called Morse-type coordinates (y_{ij}), which ensure the correct asymptotic behavior of the PES and can be given by the following expression:

$$y_{ij} = e^{-\frac{r_{ij}}{a}}, \tag{44}$$

where r_{ij} denotes the distance between atoms i and j, while a is a fixed parameter typically chosen within the range of 2-3 bohr. The PES is represented by the following functional form:[80,81]

$$V = \sum_{n=0}^{N} C_n S(y_{12}^{n_{12}} y_{13}^{n_{13}} y_{14}^{n_{14}} \cdots y_{23}^{n_{23}} y_{24}^{n_{24}} \cdots), \tag{45}$$

where S is a symmetry operator and C_n denotes the coefficients, which are determined by a weighted linear least squares fitting. The order of fitting (D) can be specified as follows:

$$\sum_{i=1}^{N-1} \sum_{j=i+1}^{N} n_{ij} \leq D. \tag{46}$$

Using the theory of invariant polynomials, the PES functions are practically represented by the following equation as its implementation can be performed much more efficiently than that of **Equation 45**:

$$V(\boldsymbol{y}) = \sum_{n=0}^{M} h_n[p(\boldsymbol{y})]q_n(\boldsymbol{y}), \tag{47}$$

where h_n represents the polynomial of primary invariant polynomials $p(\mathbf{y})$ and $q_n(\mathbf{y})$ denotes the secondary invariant polynomials. In practice, the fitting time during PES development is greatly influenced by the number of coefficients. The number of coefficients depends on the fitting degree, the number of atoms, and the permutation symmetry. If every atom within an N-atomic system is unique, the number of coefficients can be determined using the following equation:

$$\sum_{k=0}^{D} \binom{n+k-1}{k},$$

(48)

where n means the number of atom-atom coordinates, which is $N(N-1)/2$. However, it should be noted that as the size of the system increases, the number of identical atoms in the system usually also increases, resulting in a significant decrease in the number of coefficients. The precision of the PES is significantly affected by both the theoretical level of the energy calculations and the accuracy of the fitting performed with the PIP method. We can evaluate the accuracy of the fitting through the calculation of the root mean square (RMS) error, which indicates how accurately the analytical function (PES) reproduces the energy points used for fitting. In PES developments, we aim to keep the RMS value below 1 kcal/mol as this is considered the so-called chemical accuracy. After fitting the energy points as described previously, RoboSurfer begins to run dynamics simulations, which are elaborated in more detail in the following chapter (2.7). Dynamics simulations serve two main purposes: firstly, they generate new geometries from which promising ones are selected and secondly, at this stage, the quality of the PES can be verified by the number of „invalid" trajectories. These so-called „invalid" trajectories refer to dynamics simulations where the outcome leads to physically uninterpretable processes such as every molecule breaking apart into its constituent atoms. During developments, the aim is to decrease their occurrence to 0-3% in order to obtain high-quality PESs. After the energy calculations are performed at the selected geometries the new data points undergo another filter before being added to the initial database checking whether the fitting error of the energy point is above the target accuracy, which is chosen at the beginning of the PES development. If the fitting error of the given energy point exceeds the selected target accuracy, then it is added to the initial database and the 5-step cycle described earlier restarts.

2.7 DYNAMICS SIMULATIONS: THE QUASI-CLASSICAL TRAJECTORY METHOD

As introduced at the beginning of the previous chapter (2.6) by solving the nuclei motion problem, we can study the dynamics of reactions. Based on whether we treat the motion of nuclei classically or quantum mechanically, we distinguish between classical mechanical and quantum mechanical reaction dynamics calculations. Although the motion of nuclei is usually well described by the laws of classical mechanics, the experience shows that treating nuclear motion entirely classically results in rather inaccurate outcomes. This can be explained by the fact that molecules possess vibrational energy even at 0 K temperature, yet this energy is neglected in the classical approach. Furthermore, while the complete quantum approach yields highly precise outcomes, it also imposes limitations on modern computing capabilities as full-dimensional quantum dynamical calculations are not feasible for systems with more than 5-6 atoms. Thus, in my research, I employed a method for performing dynamics simulations that considers the fact that molecules possess ZPE and offers suitable computational efficiency. This method is the quasi-classical trajectory (QCT) method,[82] which is introduced in further detail in the following sections of the chapter.

2.7.1 Initial conditions

In the application of the QCT method at the beginning of the simulations the energy of the reactants is choosen to correspond to a quantum mechanical vibrational state. This initial quasi-classical vibrational state is determined through normal mode sampling.[82] The normal coordinates and their corresponding momenta for an N-atomic reactant are obtained using the following equations:

$$Q_k = \frac{\sqrt{2E_k}}{\omega_k} cos(2\pi R_k), \qquad P_k = \sqrt{2E_k}\, sin(2\pi R_k), \qquad k = 1, 2, \dots, 3N - 6 \quad (49)$$

where R_k is a random number between 0 and 1, ω_k is the vibrational frequency associated with the k-th normal mode and the energies of individual modes can be given by the following formula:

$$E_k = (n_k + 0.5)\omega_k \qquad (50)$$

where n_k denotes the vibrational quantum number corresponding to the k-th normal mode. The vibrational ground state can be defined by setting the vibrational quantum number for each mode to zero. If we intend to perform the dynamics simulation with vibrationally-excited reactants in a mode-specific manner, we set a positive integer corresponding to the desired excitation level for the vibrational mode we wish to excite. It should be noted that the harmonic vibrational energy of each mode can be calculated classically using the following expression:

$$E_k = \frac{P_k{}^2}{2} + \frac{\omega_k{}^2 Q_k{}^2}{2} \tag{51}$$

where P_k and Q_k are derived from **Equation 49**. After determining the values of the vectors **Q** and **P** using **Equations 49**, we calculate the corresponding **q** and **p** Cartesian coordinates with the following transformations:

$$\mathbf{q} = \mathbf{q}_e \mathbf{M}^{-\frac{1}{2}} \mathbf{T} \mathbf{Q} \qquad \text{and} \qquad \mathbf{p} = \mathbf{M}^{\frac{1}{2}} \mathbf{T} \mathbf{P}, \tag{52}$$

The $\mathbf{q}_e$ vector holds the equilibrium Cartesian coordinates, **M** is a diagonal matrix containing the masses of the atoms in its main diagonal and **T** represents the transformation matrix containing the normal mode eigenvectors. The angular momentum resulting from the previous transformation can be calculated as follows:

$$\mathbf{j}_0 = \sum_{i=1}^{N} \mathbf{q}_i \times \mathbf{p}_i, \tag{53}$$

where N is the number of atoms. The desired angular momentum can be set by modifying the velocity vectors according to the following formula:

$$\mathbf{v}_i = \mathbf{v}_i^0 + \mathbf{\Omega} \times \mathbf{q}_i, \tag{54}$$

where $\mathbf{v}_i^0$ is the initial velocity vector and $\mathbf{\Omega}$ can be calculated based on the following expression:

$$\mathbf{\Omega} = \mathbf{I}^{-1}(\mathbf{j} - \mathbf{j}_0), \tag{55}$$

where **I** is the moment of inertia tensor, which is calculated from the masses and positions of the reactant atoms. Following this, utilizing the **q** and **v** coordinates, the internal energy of the reactants is calculated using the applied PES according to the following equation:

$$E = 0.5 \sum_{i=1}^{N} m_i \mathbf{v}_i (\mathbf{v}_i^{\mathrm{T}}) + V(\mathbf{q}) - V(\mathbf{q}_{\mathrm{e}}). \tag{56}$$

Then, we modify the coordinates (**q**) and momenta (**p**) iteratively as described below:

$$\mathbf{q}^i = \mathbf{q}^0 + (\mathbf{q}^{i-1} - \mathbf{q}^0)\left(\frac{E_{\mathrm{int}}^0}{E_{\mathrm{int}}^{i-1}}\right)^{\frac{1}{2}}, \tag{57}$$

$$\mathbf{p}^i = \mathbf{p}^{i-1}\left(\frac{E_{\mathrm{int}}^0}{E_{\mathrm{int}}^{i-1}}\right)^{\frac{1}{2}}, \tag{58}$$

where i denotes the individual steps of the iterative process. I would like to note that in my research, the rotational angular momentum of the reactants was chosen to be zero ($\mathbf{j} = \mathbf{0}$), meaning that the reactants do not undergo rotational motion. For bimolecular reactions, the next step is to set the random orientation of the reactants. To achieve this, the Cartesian coordinates (**q**) and velocities (**v**) of the reactant molecules are rotated using an Euler rotation matrix (**R**):

$$\mathbf{q} = \mathbf{R}(\theta, \Phi, \psi)\mathbf{q}, \tag{59}$$

$$\mathbf{v} = \mathbf{R}(\theta, \Phi, \psi)\mathbf{v}. \tag{60}$$

The Euler angles are chosen as follows:

$$cos\,\theta = 2R_1 - 1, \ \ \Phi = 2\pi R_2, \ \ \psi = 2\pi R_3, \tag{61}$$

where R_1, R_2 and R_3 are different random real numbers between 0 and 1. Following this, the center of mass of one reactant is placed at the origin, while the Cartesian coordinates of the other are specified as follows:

$$x = \sqrt{s^2 - b^2}, \ y = b, \ z = 0, \tag{62}$$

where the initial distance between the center of masses of the reactants is denoted by s and b represents the impact parameter. By placing them in this manner, the reactants approach each other along the x axis as illustrated in **Figure 4**. Subsequently, the relative velocity of the reactants (v_{rel}) can be calculated using the following formula:

$$v_{\mathrm{rel}} = [2E_{\mathrm{coll}}\frac{(m_{\mathrm{A}}+m_{\mathrm{B}})}{(m_{\mathrm{A}}m_{\mathrm{B}})}]^{\frac{1}{2}}, \tag{63}$$

where E_{coll} represents the collision energy and m_{A} and m_{B} denote the masses of the reactants.
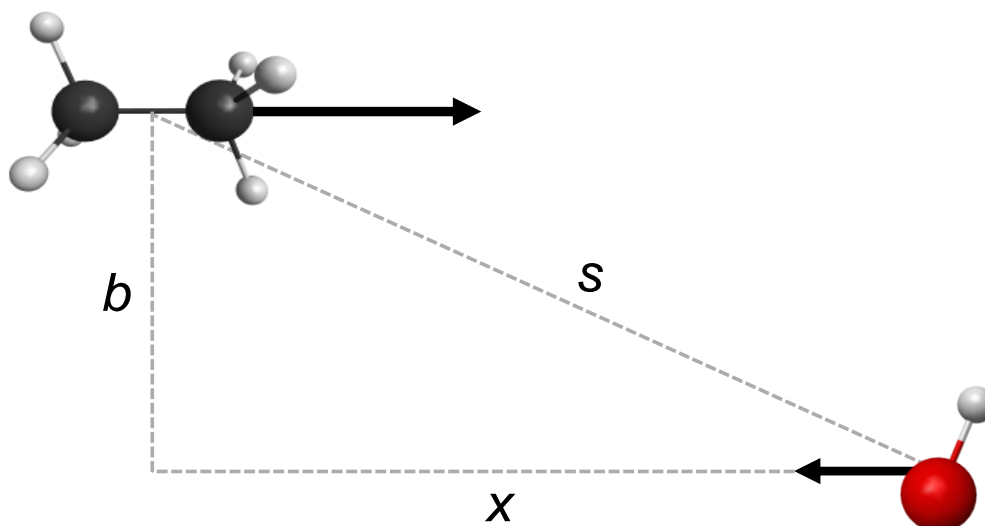
Figure 4. The initial arrangement of the reactants at the beginning of the dynamics simulation illustrating the x-axis, the meaning of the impact parameter (b), plotting the distance between the reactants (s) and indicating the velocity vectors associated with each molecule with arrows. (This example pertains to the OH + C_2H_6 reaction.)

Thus, the elements of the relative velocity vectors (x, y, z) correspond to each atom of reactants A and B as follows:

$$\mathbf{v}_A = \left(\frac{m_B}{m_A+m_B}\right) v_{rel}, 0,0),\tag{64}$$

$$\mathbf{v}_B = \left(\frac{-m_A}{m_A+m_B}\right) v_{rel}, 0,0).\tag{65}$$

2.7.2 Final conditions

Using the final Cartesian coordinates obtained at the end of the QCT simulation, we can determine the probabilities (P) of various reaction channels, typically under fixed impact parameter (b), collision energy (E_{coll}), vibrational (n) and rotational quantum numbers (J, K).

$$P(b, E_{coll}, n, J, K) = \frac{N_r(b,E_{coll},n,J,K)}{N_t(b,E_{coll},n,J,K)},\tag{66}$$

where N_r represents the number of reactive trajectories for the different reaction channels and N_t denotes the total number of trajectories.

The integral cross-section (ICS, σ) is obtained by integrating the reaction probability over the impact parameter from $b = 0$ to $b = b_{\text{max}}$, where b_{max} is the value of the maximum impact parameter beyond which the reaction probability becomes zero:

$$\sigma(E_{\text{coll}}, n, J, K) = \int_0^{b_{\text{max}}} 2\pi b P(b, E_{\text{coll}}, n, J, K) db. \tag{67}$$

In practice, this quantity can be calculated through numerical integration, for example, using the trapezoidal method by running trajectories with uniform steps between 0 and b_{max}:

$$\sigma(E_{\text{coll}}, n, J, K) = \pi \sum_{n=1}^{n_{\text{max}}} [b_n - b_{n-1}][b_n P(E_{\text{coll}}, n, J, K) + b_{n-1} P(E_{\text{coll}}, n, J, K)], \tag{68}$$

where typically each b value is chosen with a step size of 0.5 bohr and n_{max} means the number of b intervals.

In the QCT method, although we set a quantum mechanical vibrational energy level for the reactants at the beginning of the simulations, once the reaction commences, we propagate it solely according to the laws of classical physics. Consequently, during the process, the zero-point energy of the reactants can leak into other modes resulting in products whose vibrational energy does thus not reach the ZPE value. We can eliminate this kind of zero-point energy violation by introducing constraints (SOFT and HARD) on the vibrational energy of the products. In the SOFT case, we disregard those trajectories where the sum of the vibrational energies of the products is less than the sum of their ZPEs. In the case of HARD constraint, we only consider those trajectories where the vibrational energy of each product individually exceeds its respective ZPE value.

Experimentally measured quantity is the scattering angle distribution (*differential cross-section*: DCS) where the scattering angle (θ) itself is defined by taking the cosine of the angle of the relative velocity vectors of the center of masses of the reactants and products:

$$cos(\theta) = \frac{\mathbf{v}_{\text{rel,r}} \cdot \mathbf{v}_{\text{rel,p}}}{|\mathbf{v}_{\text{rel,r}}| \cdot |\mathbf{v}_{\text{rel,p}}|}, \tag{69}$$

where the center of mass relative velocity vectors of the reactants ($\mathbf{v}_{\text{rel,r}}$) and products ($\mathbf{v}_{\text{rel,p}}$) can be derived as follows:

$$\mathbf{v}_{rel,r} = \mathbf{v}_{reactant,1} - \mathbf{v}_{reactant,2}, \tag{70}$$

$$\mathbf{v}_{rel,p} = \mathbf{v}_{product,1} - \mathbf{v}_{product,2}, \tag{71}$$

where $\mathbf{v}_{reactant,1}$ and $\mathbf{v}_{reactant,2}$ denote the velocity vectors for the reactants, while $\mathbf{v}_{product,1}$ and $\mathbf{v}_{product,2}$ represent those for the products. Backward scattering is indicated when $\cos(\theta) = -1$ and forward scattering is defined as $\cos(\theta) = 1$. For better understanding, the meaning of scattering angle is illustrated in **Figure 5**. The initial attack angle (α) can be determined for reactants providing information on how the reactants collide with each other in different reaction types. We can define the initial attack angle as the angle between the center of mass velocity vector of the given reactant ($\mathbf{v}_r$) and a vector corresponding to a specific bond ($\mathbf{v}_b$):

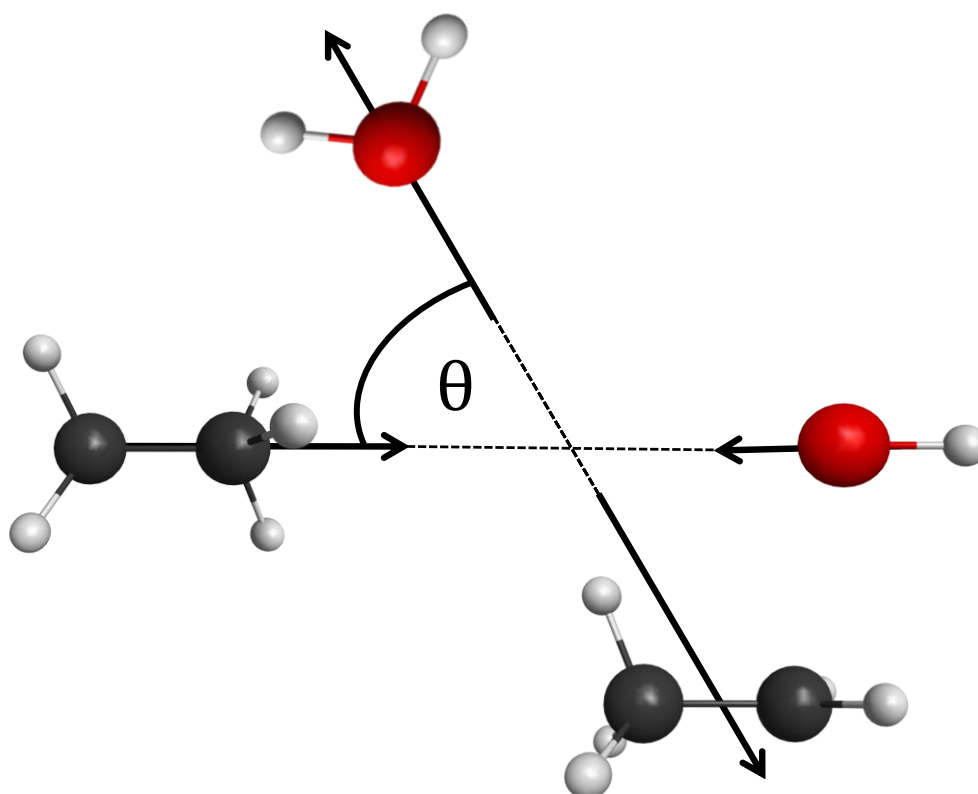$$cos(\alpha) = \frac{\mathbf{v}_r \cdot \mathbf{v}_b}{|\mathbf{v}_r| \cdot |\mathbf{v}_b|}. \tag{72}$$

Figure 5. The scattering angle (θ) depicted through the example of the OH + C_2H_6 reaction. Adapted from Ref. [2].

The understanding of the initial attack angle is aided by **Figure 6**. For the products, the translational energy (E_{trans}) can be calculated based on the following formula:

$$E_{\text{trans}} = \frac{1}{2}\mu v_{\text{rel,p}}^2, \tag{73}$$

where μ is the so-called reduced mass, which can be obtained as follows:

$$\mu = \frac{m_A m_B}{m_A + m_B}, \tag{74}$$

where m_A and m_B are the masses of the products in atomic mass units.
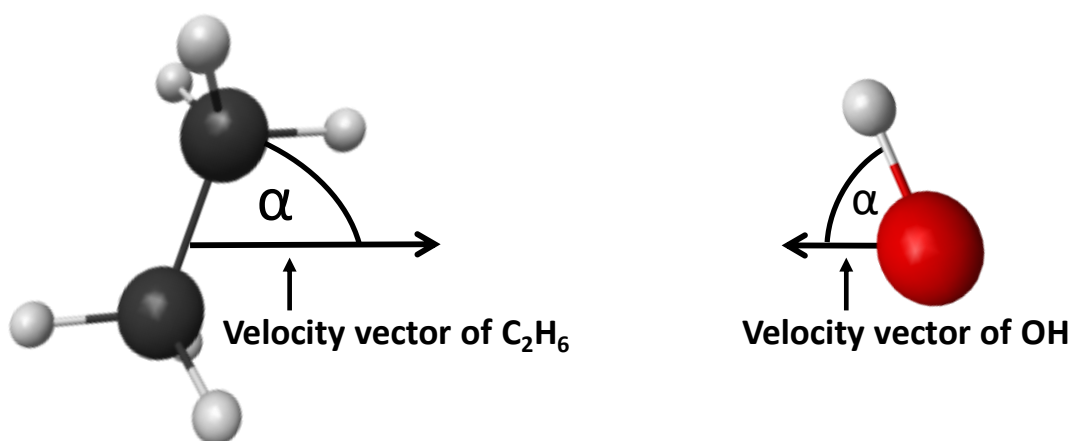
Figure 6. The meaning of the initial attack angle (α) is illustrated for the OH + C$_2$H$_6$ system. Adapted from Ref. [2].

The internal energy of a polyatomic product (E_{int}) consists of two parts: kinetic energy (T) and potential energy (V):

$$E_{\text{int}} = T + V. \tag{75}$$

The kinetic part can be calculated based on the following equation:

$$T = \sum_{i=1}^{N} \frac{1}{2} m_i \mathbf{v}_i^2, \tag{76}$$

where m_i denotes the mass of the i-th atom, $\mathbf{v}_i$ represents the mass center velocity vector of the i-th atom and N is the number of atoms. The potential energy component is obtained by taking the difference between the potential energy associated with the structure corresponding to the given product at the end of the QCT simulation and the potential energy associated with the equilibrium geometry of the product on the analytical PES. Furthermore, the internal energy (E_{int}) can be expressed as the sum of vibrational (E_{vib}) and rotational (E_{rot}) energies, so the difference between the internal energy and the rotational energy gives the vibrational energy of individual products:

$$E_{\text{vib}} = E_{\text{int}} - E_{\text{rot}}. \tag{77}$$

The rotational energy can be determined using the following equation:

$$E_{\text{rot}} = \frac{1}{2}\boldsymbol{\omega}^{\text{T}}\mathbf{j}, \tag{78}$$

where $\boldsymbol{\omega}$ represents the angular velocity vector and $\mathbf{j}$ denotes the angular momentum vector. The angular velocity vector can be calculated after diagonalizing the inertia tensor ($\mathbf{I}$) as follows:

$$\boldsymbol{\omega} = \mathbf{I}^{-1} \cdot \mathbf{j}. \tag{79}$$

The angular momentum vector can be obtained with the following expression:

$$\mathbf{j} = \sum_i m_i \mathbf{r}_i \times \mathbf{v}_i, \tag{80}$$

where m_i represents the mass of the i-th atom, $\mathbf{r}_i$ denotes the center of mass position coordinates for the i-th atom, and $\mathbf{v}_i$ is the center-of-mass velocity vector associated with the i-th atom. Once the angular momentum vector is determined, the rotational quantum number can be obtained using a classical approach by taking the length of the $\mathbf{j}$ vector and rounding the result to the nearest integer value.

After conducting QCT simulations for the OH + C_2H_6 reaction, I have also obtained mode-specific vibrational energy distributions for the water molecule. The procedure of these calculations is briefly outlined below. Firstly, we determine the harmonic vibrational frequencies and normal-mode eigenvectors for the water molecule using normal mode analysis on the PES. Next, we set the angular momentum of the product molecule to zero

by modifying the velocity vectors. Next, the product needs to be rotated to the orientation that best overlaps with the equilibrium geometry for each reactive trajectory, which can be achieved using an Eckart transformation. In the following phase, the normal modes (Q_k) and momenta (P_k) are computed based on the mass-scaled Cartesian displacement coordinates and velocities employing the transformation matrix determined earlier. In the end, the harmonic vibrational energies (E_k) corresponding to individual normal-modes can be obtained with **Equation 51** and the integer quantum numbers are derived using the following expression:

$$n_k = \left\lfloor \frac{E_k}{\omega_k} \right\rfloor, \tag{81}$$

where n_k is determined by rounding down to the closest integer number. Then, the mode-specific vibrational distribution can be obtained utilizing the histogram binning technique. The following formula provides the probability of a specific vibrational state (n) at a particular impact parameter (b):

$$P(b, n) = \frac{N(b,n)}{N_t}, \tag{82}$$

where N represents the number of the given molecule, in this case H_2O, at vibrational state n, and N_t is the total number of trajectories at a given b.

3 RESULTS

3.1 MAPPING THE TOPOLOGY OF THE PESS OF THE REACTIONS

The theoretical study of individual reactions begins with identifying the key stationary points of the reactions providing a good foundation for the further PES development. The general procedure for mapping out the PES is as follows. The desired minima and transition states are initially located using a lower theoretical level and then, geometry optimization and frequency calculations are performed at a higher theoretical level to improve the results obtained earlier. Following this, we refine the energy values determined so far by employing a larger basis set utilizing the best geometries identified. Finally, in order to achieve higher chemical accuracy, using the most accurate structures obtained, five different energy correction calculations are taken into account. (1 and 2) To gain insight into the effects of the perturbative approximations indicated in parentheses in the name of the explicitly-correlated coupled cluster method, post-CCSD(T) correlation corrections (δ[T] and δ[(Q)]) are calculated. (3) Since chemical processes typically involve the valence orbitals of individual molecules, thus frozen-core (FC) calculations are traditionally carried out, where only the valence electrons are correlated during the computations. To account for the effects of core electron correlation, all-electron (AE) calculations are performed and the core-correlation correction (Δ_{core}) is calculated as the difference between the AE and FC energies. The two main types of relativistic effects are scalar and spin-orbit interactions. (4) The foundation of Einstein's special theory of relativity is the recognition that time and space are not absolute but rather relative concepts which can vary depending on the motion and velocity of the observer. Mathematically, we can gain insight into the matter as follows:

$$m = \frac{m_0}{\sqrt{1-\frac{v^2}{c^2}}}, \tag{83}$$

where m represents the relativistic mass of the particle, m_0 denotes its rest mass, v stands for its velocity and c indicates the speed of light. Thus, the relationship between mass, energy and velocity does not change unambiguously in a classical manner at high speeds as evident from the equation where as velocity approaches the speed of light, mass tends to infinity. This implies that increasingly more energy is required to achieve further

increases in velocity. The effect arising from this increase in mass is called the scalar relativistic effect (Δ_{rel}) that is calculated with the second-order Douglas−Kroll (DK) operator. (5) Another relativistic effect is the spin-orbit interaction (Δ_{SO}), which is based on the notion that electronic energy is influenced not only by the rotation of the electrons around their own axis (spin) and their motion around the atomic nucleus, but also by the interaction between these two. The spin-orbit corrections are calculated using the Breit−Pauli Hamiltonian in the interacting-states approach utilizing the Davidson-corrected multi-reference configuration interaction (MRCI+Q) method. In the following subsections of this chapter (3.1), the details of the computations are presented for each reaction first, which is followed by an in-depth discussion of the results.

3.1.1 OH + C$_2$H$_6$

3.1.1.1 Computational details

For the OH + C$_2$H$_6$ reaction, optimization of the structures corresponding to each stationary point and determination of the harmonic frequencies are carried out at three different theoretical levels: MP2/aug-cc-pVDZ, CCSD(T)-F12b/aug-cc-pVDZ and CCSD(T)-F12b/aug-cc-pVTZ (except for some of the stationary points). Single-point energy calculations are performed at the CCSD(T)-F12b/aug-cc-pVQZ level of theory. The post-CCSD(T) correlation correction is computed with the CCSDT,[83] CCSD(T), and CCSDT(Q)[84] methods using the cc-pVDZ basis set:

$$\delta[T] = CCSDT/cc\text{-}pVDZ - CCSD(T)/cc\text{-}pVDZ \tag{84}$$

and

$$\delta[(Q)] = CCSDT(Q)/cc\text{-}pVDZ - CCSDT/cc\text{-}pVDZ. \tag{85}$$

All-electron calculations are performed to account for the effects of core electron correlation on energy where namely the $1s^2$ electrons are also correlated for both the C and O atoms in case of the OH + C$_2$H$_6$ reaction. CCSD(T)-F12b/cc-pCVTZ-F12 level of theory is applied to calculate the core-correlation correction:

$$\Delta_{core} = AE\text{-}CCSD(T)\text{-}F12b/cc\text{-}pCVTZ\text{-}F12 - FC\text{-}CCSD(T)\text{-}F12b/cc\text{-}pCVTZ\text{-}F12. \tag{86}$$

The scalar relativistic effect is obtained with the following expression:

$$\Delta_{rel} = \text{DK-AE-CCSD(T)-F12b/cc-pCVTZ-F12} - \text{AE-CCSD(T)-F12b/cc-pCVTZ-F12.} \quad (87)$$

During spin-orbit calculations in the MRCI calculations a 21-electron active space is employed, consisting of 11 spatial orbitals, while keeping all 6 core electrons frozen. The SO computations are obtained at the following levels of theory:

$$\Delta_{SO} = \text{SO}_1(\text{MRCI+Q/aug-cc-pVTZ(DZ)}) - \text{non-SO}_1(\text{MRCI+Q/aug-cc-pVTZ(DZ)}). \quad (88)$$

The benchmark classical relative energies (E_{cl}) are calculated as follows:

$$E_{cl} = \text{CCSD(T)-F12b/aug-cc-pVQZ} + \delta[T] + \delta[(Q)] + \Delta_{core} + \Delta_{rel}. \quad (89)$$

The adiabatic energies are obtained by adding the ZPE calculated at the highest theoretical level to the classical energy:

$$E_{ad} = \text{CCSD(T)-F12b/aug-cc-pVQZ} + \delta[T] + \delta[(Q)] + \Delta_{core} + \Delta_{rel} + \text{ZPE}. \quad (90)$$

3.1.1.2   Results

In the case of the OH + C_2H_6 reaction, 3 different product channels are considered: 1) H-abstraction, 2) H-substitution and 3) methyl-substitution. For H-abstraction, the OH radical removes a hydrogen atom from the C_2H_6 molecule yielding a water molecule and a C_2H_5 radical as products. In a substitution reaction, a portion of the C_2H_6 molecule is replaced by the attacking OH. If only a hydrogen atom is removed from C_2H_6, it is called H-substitution, while methyl-substitution occurs when the CH_3 group is replaced by OH. Substitution reactions can proceed via two mechanisms: Walden inversion and front-side attack. If the hydroxyl radical attacks from the opposite side of the departing group, we refer to the well-known Walden-inversion mechanism; whereas if the hydroxyl radical approaches the ethane molecule from the same side as the departing group is, it can be considered a front-side attack mechanism. **Figure 7** illustrates the identified minima and transition states corresponding to the previously-mentioned reaction channels along with their relative classical and adiabatic energies. Out of the 3 possible product channels the H-abstraction and methyl substitution are exothermic with relative classical(adiabatic) energies of −16.70(−18.19) kcal/mol and −0.94(−2.20) kcal/mol, respectively. The H-substitution reaction pathway exhibits an endothermic character as the energy of the

products exceeds that of the reactants by 9.10(7.12) kcal/mol classically(adiabatically). It can be observed that for each reaction pathway, there is an energy barrier that must be overcome for the reaction to proceed indicating that every reaction pathway is kinetically hindered.
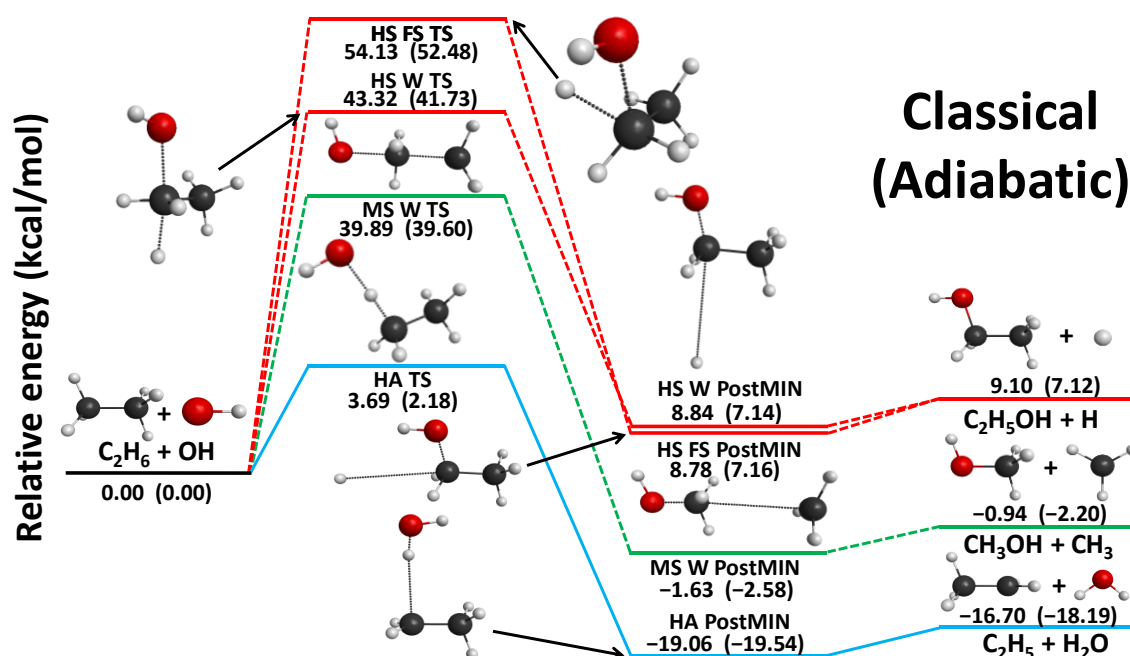

Figure 7. Graphical representation of the schematic potential energy landscape of the OH + C_2H_6 reaction showing classical(adiabatic) relative energy levels corresponding to the stationary points along the different reaction pathways. Blue indicates the H-abstraction, green represents the methyl-substitution and red signifies the H-substitution reaction channels. Adapted from Ref. [1].

The smallest energy barrier belongs to H-abstraction with a height of 3.69(2.18) kcal/mol classically(adiabatically) that is followed by the methyl-substitution with the second smallest barrier, which has a value of 38.89(39.60) kcal/mol classically(adiabatically). The highest energy barriers are observed in the case of H-substitution where if the reaction proceeds through the Walden-inversion mechanism the barrier height is 43.32(41.73) kcal/mol classically(adiabatically), while if the reaction occurs via the front-side attack mechanism, then 54.13(52.48) kcal/mol energy is required classically(adiabatically) to form the characteristic transition state of the reaction. In the exit channel, 4 different minima can be identified among which the H-abstraction minimum has the deepest energy with a relative classical(adiabatic) energy of 19.06(19.54) kcal/mol. This is followed by the methyl-

substitution minimum with a relative classical(adiabatic) energy of −1.63(2.58) kcal/mol, while the highest-energy minima in the exit channel are associated with the H-substitution reaction pathway. Between the two H-substitution minima only a tiny energy difference can be observed and when the ZPE is considered the energy order is reversed. In classical terms, the front-side H-substitution minimum stands deeper at 8.78 kcal/mol compared to the Walden-inversion H-substitution minimum, which is only 0.06 kcal/mol higher. However, in adiabatic terms, the front-side mechanism minimum is at 7.16 kcal/mol, while the Walden-inversion minimum is at 7.14 kcal/mol relative energy. By examining the structural parameters of each stationary point with the help of **Figure 8**, we can verify the validity of the Hammond postulate.[85] The Hammond postulate states that an exothermic reaction has a transition state that more closely resembles the structure of the reactants, whereas an endothermic reaction has a transition state that more closely resembles the structure of the products. In the OH + C_2H_6 H-abstraction reaction, the attacking hydroxyl radical removes a hydrogen atom from the ethane molecule resulting in the formation of an ethyl radical and a water molecule. Accordingly, a transition state forms during the reaction, where the hydroxyl radical begins to bond to one of the hydrogen atoms in the ethane molecule, while simultaneously the affected C-H bond, from which the hydrogen atom departs, elongates. The hydrogen of the corresponding OH group is located away from the C-C bond of the ethane molecule (trans configuration). In the case of the minimum in the hydrogen-abstraction product channel, it can be observed that compared to the structure of the transition state, the hydrogen atom of the OH group is no longer closer to the ethane molecule, but rather further away. In this structure, the distance between the departing hydrogen and the carbon atom of the ethane molecule is much larger, nearly twice the distance of the C-H bond in the transition state. The distance between the departing hydrogen and the associated oxygen atoms as well as the H-O-H bond angle, now take values almost identical to those of a water molecule. Furthermore, it is worth noting that the trans configuration characteristic of the transition state structure no longer applies to the structure of the minimum in the product channel as the hydrogen of the OH radical is oriented towards the C-C bond. The transition state can be considered as reactant-like in the case of the H-abstraction reaction channel as the resulting O-H bond distance is less similar to that in the water molecule than the elongating C-H bond to that in the ethane. Thus, in this case, the Hammond postulate can be considered true as the reaction is

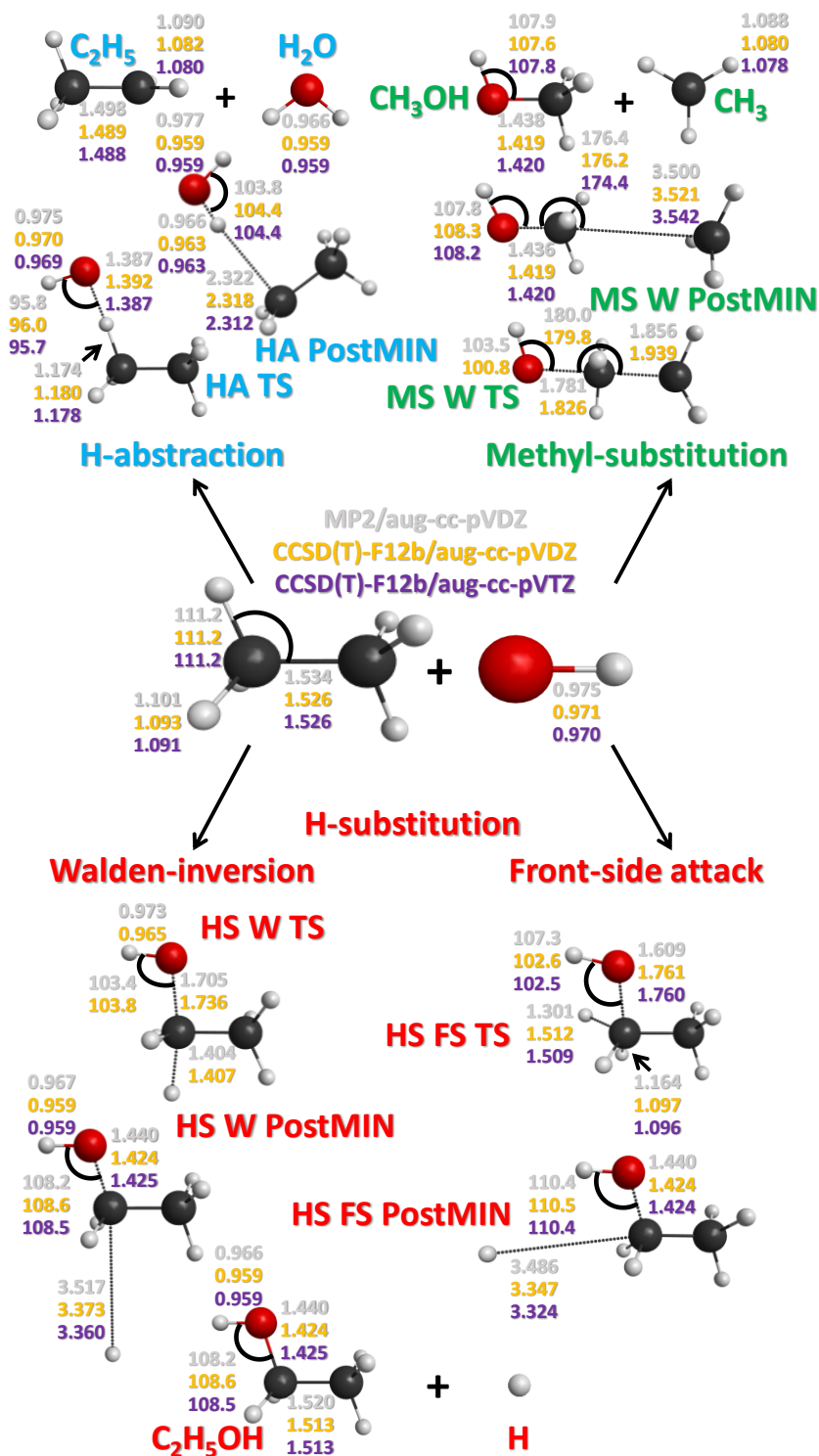**Figure 8.** Presenting the structural parameters of the stationary points corresponding to the various reaction pathways in the OH + C_2H_6 reaction. The values of the structural parameters are indicated at three different quantum chemical levels marked with gray, orange and purple colors, respectively. Bond distances are in angstroms (Å), bond angles are in degrees (°). Adapted from Ref. [1].

exothermic. In case of the Walden-methyl-substitution reaction, a transition state forms where the C-C bond elongates and the hydroxyl radical attacks the carbon atom of the ethane molecule from the opposite side of the departing methyl group through its oxygen atom. As the reaction progresses towards its product-channel minimum, the hydrogens undergo an umbrella-like flip, which is characteristic of Walden inversion and simultaneously the departing methyl group adopts a planar configuration resembling that of the methyl radical. Furthermore, it can be observed that both the structure of the transition state and the product-channel minimum exhibit a nearly linear O-C-C bond angle. The Hammond postulate proves true in this scenario as well, as the reaction is exothermic. The validity of the postulate implies that the transition state is more reactant-like as there is a smaller difference in C-C bond distances between the transition state and the ethane molecule compared to the distance between the oxygen and carbon atoms in the transition state and the methanol molecule. As we have seen before, the H-substitution reaction can proceed through two mechanisms: Walden inversion and front-side attack. In both mechanisms, the structure of the transition state involves the attacking hydroxyl radical beginning to bind to one of the carbon atoms in the ethane molecule. However, while in the case of Walden inversion, the departing hydrogen atom from the carbon is on the opposite side of the attacking hydroxyl radical and in the case of front-side attack, the attacking hydroxyl radical and the departing hydrogen are on the same side in the structure of the transition state. In both cases of Walden inversion and front-side attack, a notable feature is that the exiting hydrogen atom is moved to a distance nearly 2.5 times greater as the reaction progresses from the transition state to the minimum of the product channel. In both reaction channels, it can be stated that the transition states are product-like as the O-C bonds of the transition states resemble more closely those in the product ethanol, rather than the C-H bonds of the transition states resemble those in the reactant ethane molecule. Thus, according to the Hammond postulate, the reactions must be endothermic meaning that the postulate holds true in this case as well. Examining the obtained values, it can be concluded that while there is a significant difference between the MP2 and CC methods, the difference between the structural parameters determined at the CCSD(T)-F12b/aug-cc-pVDZ and CCSD(T)-F12b/aug-cc-pVTZ theoretical levels is very small and in some cases, these results are entirely consistent indicating the good basis convergence of the explicitly-correlated methods. **Table 1** and **Table 2** provide a detailed

overview of the energy values obtained at each theoretical level. Looking at the data in **Table 1**, we can see that although there are significant differences of several kcal/mol between the MP2 and CC results, the energies calculated with the CC method (using DZ, TZ, and QZ bases) agree within 1 kcal/mol.

Table 1. Energies of the stationary points of the $OH + C_2H_6$ reaction, expressed in kcal/mol units, relative to the reactants. The table is taken from Ref. [1].

Stationary points	MP2	CCSD(T)-F12b			$\sum\Delta^e$	Classical[f]	Δ_{ZPE}[g]	Adiabatic[h]
	aVDZ[a]	aVDZ[b]	aVTZ[c]	aVQZ[d]				
HA TS	6.21	3.45	3.65	3.70	−0.01	3.69	−1.51	2.18
HA PostMIN	−21.78	−19.28	−19.07	−19.09	+0.03	−19.06	−0.48	−19.54
MS W TS	44.80[k]	40.29	40.21[i]	40.21[i]	−0.32	39.89	−0.29[j]	39.60
MS W PostMIN	−3.14[k]	−2.02	−1.85	−1.89	+0.26	−1.63	−0.95[j]	−2.58
HS W TS	39.89	43.57	43.49[i]	43.51[i]	−0.19	43.32	−1.59[j]	41.73
HS W PostMIN	2.11	7.96	8.62	8.63	+0.21	8.84	−1.67	7.17
HS FS TS	55.68[k]	54.33	54.47	54.53	−0.40	54.13	−1.65[j]	52.48
HS FS PostMIN	2.00[k]	7.90	8.56	8.57	+0.21	8.78	−1.62[j]	7.16
$C_2H_5 + H_2O$	−18.96	−16.64	−16.61	−16.75	+0.05	−16.70	−1.49	−18.19
$CH_3OH + CH_3$	−2.24	−1.16	−1.13	−1.21	+0.27	−0.94	−1.26	−2.20
$C_2H_5OH + H$	2.29	8.29	8.91	8.89	+0.21	9.10	−1.98	7.12

[a] MP2/aug-cc-pVDZ relative energies computed at MP2/aug-cc-pVDZ geometries.

[b] CCSD(T)-F12b/aug-cc-pVDZ relative energies computed at CCSD(T)-F12b/aug-cc-pVDZ geometries.

[c] CCSD(T)-F12b/aug-cc-pVTZ relative energies computed at CCSD(T)-F12b/aug-cc-pVTZ geometries.

[d] CCSD(T)-F12b/aug-cc-pVQZ relative energies computed at CCSD(T)-F12b/aug-cc-pVTZ geometries.

[e] $\sum\Delta = \delta[T] + \delta[(Q)] + \Delta_{core} + \Delta_{rel} + \Delta_{SO}(\text{aug-cc-pVTZ})$.

[f] Benchmark relative classical energy calculated as CCSD(T)-F12b/aug-cc-pVQZ + $\sum\Delta$.

[g] ZPE correction computed at CCSD(T)-F12b/aug-cc-pVTZ (for exemptions see [j]).

[h] Benchmark relative adiabatic energy calculated as classical + Δ_{ZPE}.

[i] Determined at CCSD(T)-F12b/aug-cc-pVDZ.

[j] ZPE correction determined at CCSD(T)-F12b/aug-cc-pVDZ.

[k] Determined with UMP2.

Furthermore, the difference is typically much smaller between the energies calculated using the CCSD(T)-F12b/aug-cc-pVTZ and CCSD(T)-F12b/aug-cc-pVQZ theoretical levels compared to the CCSD(T)-F12b/aug-cc-pVTZ and CCSD(T)-F12b/aug-cc-pVDZ levels indicating the excellent basis convergence of the CCSD(T)-F12b method. Moreover, the energy corrections typically alter the classical/adiabatic energies by a few tenths of a kcal/mol and the most significant effect occurs for the HS FS TS with an absolute value of

0.40 kcal/mol. Regarding the ZPE corrections, it can be noted that they typically take on values around −1.5 kcal/mol, except for 3 cases (HA PostMIN, MS W TS and MS W PostMIN) where the ZPE decreases the classical energies by less than 1 kcal/mol. The results of the correction calculations determined at various theoretical levels are summarized in **Table 2**.

Table 2. Energy corrections for the stationary points of the OH + C_2H_6 reaction, expressed in kcal/mol units, relative to the reactants. The table is taken from Ref. [1].

Stationary points	$\delta[T]$[a]	$\delta[(Q)]$[b]	Δ_{core}[c]	Δ_{rel}[d]	Δ_{SO}[e]		Δ_{ZPE}[f]		
					aVDZ	aVTZ	MP2/DZ	CC/DZ	CC/TZ
HA TS	−0.11	−0.14	0.03	0.02	0.18	0.19	−2.08	−1.74	−1.51
HA PostMIN	−0.04	−0.13	−0.11	0.12	0.18	0.19	−0.08	−0.31	−0.48
MS W TS	−0.48[g]	−0.43[g]	0.39[g]	0.01[g]	0.18[g]	0.19[g]	1.19[h]	−0.29	−
MS W PostMIN	−0.02	−0.12	0.09	0.12	0.18	0.19	−0.84[h]	−0.95	−
HS W TS	−0.27[g]	−0.40[g]	0.24[g]	0.05[g]	0.18[g]	0.19[g]	−1.55	−1.59	−
HS W PostMIN	0.10	−0.20	−0.02	0.14	0.18	0.19	−1.82	−1.69	−1.67
HS FS TS	−0.38	−0.50	0.26	0.03	0.18	0.19	−1.88[h]	−1.65	−
HS FS PostMIN	0.10	−0.20	−0.02	0.14	0.18	0.19	−1.80[h]	−1.62	−
$C_2H_5 + H_2O$	−0.03	−0.12	−0.11	0.12	0.18	0.19	−1.51	−1.47	−1.49
$CH_3OH + CH_3$	−0.02	−0.11	0.09	0.12	0.18	0.19	−1.15	−1.21	−1.26
$C_2H_5OH + H$	0.10	−0.20	−0.02	0.14	0.18	0.19	−2.08	−1.92	−1.98

[a] Eq. (84). [b] Eq. (85). [c] Eq. (86). [d] Eq. (87). [e] Eq. (88).

[f] ZPE correction determined at MP2/aug-cc-pVDZ, CCSD(T)-F12b/aug-cc-pVDZ and CCSD(T)-F12b/aug-cc-pVTZ.

[g] Computed at CCSD(T)-F12b/aug-cc-pVDZ geometries.

[h] Determined with UMP2.

The results of the post-CCSD(T) calculations typically take on negative values except for the HS W PostMIN, HS FS PostMIN minima and H-substitution products where the $\delta[T]$ is consistently 0.10 kcal/mol. The core-correlation correction exhibits variable tendencies decreasing the energy value relative to the reactants in some stationary points while increasing it in others. The most significant change is observed in the case of MS W TS, where its value is 0.39 kcal/mol. Taking the scalar relativistic effect into account, it can be observed that each stationary point possesses a higher relative energy when this effect is considered. Furthermore, it can be concluded that the scalar relativistic effect with a maximum value of 0.14 kcal/mol exerts one of the smallest impacts on the energy among

the five auxiliary corrections. The spin-orbit correction is consistently a positive value in each case with values of 0.18 kcal/mol using the aug-cc-pVDZ basis and 0.19 kcal/mol using the aug-cc-pVTZ basis indicating that this effect is significant only for the reactants. With the help of formation enthalpies obtained from the Active Thermochemical Tables (ATcT), it is possible to calculate reaction enthalpies, which can be compared with the adiabatic energy values calculated by us, as shown in **Table 3**.

Table 3. Comparison between the currently available best "experimental" (ATcT) results and the 0 K reaction enthalpies determined by us for the OH + C_2H_6 reaction. The values are given in kcal/mol units. The table is taken from Ref. [1].

Reaction	Theory[a]	ATcT[b]
$OH + C_2H_6 \rightarrow C_2H_5 + H_2O$	−18.19	−18.35 ± 0.07
$OH + C_2H_6 \rightarrow CH_3OH + CH_3$	−2.20	−2.16 ± 0.05
$OH + C_2H_6 \rightarrow C_2H_5OH + H$	7.12	7.13 ± 0.06

[a] Benchmark relative adiabatic energy calculated in this work.
[b] Data obtained from the Active Thermochemical Tables (ATcT).

Based on **Table 3**, it can be concluded that the relative adiabatic 0 K energies determined in this work are in excellent agreement with the reaction enthalpy values calculated using the ATcT. Moreover, it is worth noting that the compared values coincide within the margin of error in the case of H- and methyl-substitution. Significant energy decrease arises from spin-orbit coupling in the hydroxyl radical prompting us to gain deeper insight into the reaction by calculating 1-dimensional potential energy curves with and without spin-orbit coupling as shown in **Figure 9**. These computations are performed at the MRCI+Q/aug-cc-pVDZ level of theory and the curves are obtained by bringing the reactants closer together while keeping them frozen at their equilibrium structures. Disregarding spin-orbit interaction, the electronic ground state of the OH radical is $^2\Pi$. Yet, when accounting for the spin-orbit effect, it divides into lower and higher energy levels, known as the spin-orbit ground state and the spin-orbit excited state, corresponding to the $^2\Pi_{3/2}$ and $^2\Pi_{1/2}$ levels, respectively. In the orientation shown on the left panel, the OH radical approaches the C_2H_6 molecule aligned with the C-C bond, where an almost 0.8 kcal/mol deep minimum is observed around 3.4 Å. As shown in the small inset, as the C···OH
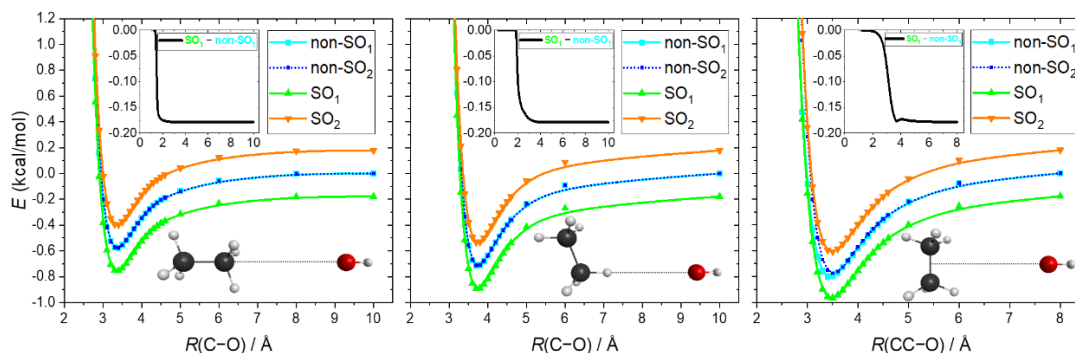
Figure 9. Potential energy curves determined at the MRCI+Q/aug-cc-pVDZ theoretical level for 3 different orientations, while the structures of the reactants are kept frozen at their equilibrium geometries. On the left panel the OH radical approaches C_2H_6 along the C-C bond, on the middle panel the OH radical approaches along one of the C-H bonds of C_2H_6 and on the right panel the OH radical approaches C_2H_6 perpendicular to the C-C bond, each time with its oxygen atom facing ethane. SO_1 and SO_2 shows the spin-orbit ground and excited states, while non-SO_1 and non-SO_2 are the non-relativistic ground and excited electronic states, respectively. The insets denote the distance dependence of the spin-orbit corrections determined as difference between the SO_1 and non-SO_1 energies. Adapted from Ref. [1].

distance decreases to about 1.7-1.8 Å, the energy decrease due to spin-orbit coupling disappears. The middle panel shows the potential energy curve where the OH radical approaches one of the hydrogens of the C_2H_6 molecule along a C-H bond of C_2H_6. In this configuration, there is an approximately 0.9 kcal/mol deep minimum occurring when the CH···OH distance is around 3.7 Å. Less abruptly than in the previous case, at around 4 Å CH···OH distance, the absolute value of the energy decrease from spin-orbit coupling starts to decrease and upon reaching a distance of 2.0 Å, the correction value becomes zero. Lastly, in the right panel, an arrangement is depicted where the OH radical approaches the C-C bond in the C_2H_6 molecule perpendicularly. In this orientation, the deepest minimum is observed with a depth of almost 1 kcal/mol occurring at approximately 3.5 Å. In this case, observing the small inset, we can see that the magnitude of the spin-orbit coupling effect starts to decrease around 3.9 Å, then becomes completely zero at 2 Å.

3.1.2 OH + CH₃NH₂

3.1.2.1 Computational details

For the OH + CH$_3$NH$_2$ reaction, the stationary points are located at the MP2/aug-cc-pVDZ theoretical level, just as in the case of the OH + C$_2$H$_6$ system. Afterwards, geometry optimizations and frequency calculations are carried out using the coupled-cluster method with both aug-cc-pVDZ and aug-cc-pVTZ basis sets. In some cases, the standard Hartree−Fock method did not converge, so we applied the ManyHF method to overcome this issue.[86] To achieve more accurate energies, energy calculations are conducted at the CCSD(T)-F12b/aug-cc-pVQZ theoretical level utilizing the most accurate geometries. For the post-CCSD(T) correlation correction calculations the CCSD(T), CCSDT, and CCSDT(Q) methods are utilized with the cc-pVDZ basis set, described by the following expressions:

$$\delta[T] = CCSDT/cc\text{-}pVDZ - CCSD(T)/cc\text{-}pVDZ \tag{91}$$

and

$$\delta[(Q)] = CCSDT(Q)/cc\text{-}pVDZ - CCSDT/cc\text{-}pVDZ \tag{92}$$

To calculate the core-correlation correction, both all-electron (AE) and frozen-core (FC) computations are performed deriving the core-correlation correction from the difference between these two sets of calculations as follows:

$$\Delta_{core} = AE\text{-}CCSD(T)\text{-}F12b/cc\text{-}pCVTZ\text{-}F12 - FC\text{-}CCSD(T)\text{-}F12b/cc\text{-}pCVTZ\text{-}F12 \tag{93}$$

To account for scalar relativistic effects, second-order Douglas−Kroll (DK) relativistic energies are utilized, which are computed at the AE-CCSD(T)/aug-cc-pwCVTZ-DK level of theory. Non-relativistic calculations are carried out at the AE-CCSD(T)/aug-cc-pwCVTZ level. The scalar relativistic correlation is defined as the difference between these two sets of energies as given by the following equation:

$$\Delta_{rel} = DK\text{-}AE\text{-}CCSD(T)/aug\text{-}cc\text{-}pwCVTZ\text{-}DK - AE\text{-}CCSD(T)/aug\text{-}cc\text{-}pwCVTZ \tag{94}$$

Spin-orbit (SO) coupling corrections are considered using the Breit−Pauli Hamiltonian within the interacting-states framework applying the Davidson-corrected multi-reference configuration interaction (MRCI+Q) method with the aug-cc-pVTZ basis set. In the MRCI calculations, an active space of 21 electrons distributed over 11 spatial orbitals is used,

while all 3 doubly-occupied core orbitals remain closed. The spin-orbit correction is calculated as the difference between the energies of the SO_1-ground-state and the non-SO_1-ground-state as given by:

$$\Delta_{SO} = SO_1(MRCI+Q/aug\text{-}cc\text{-}pVTZ) - non\text{-}SO_1(MRCI+Q/aug\text{-}cc\text{-}pVTZ) \qquad (95)$$

To gain a clearer understanding of the entrance channel, one-dimensional scans are performed at the ManyHF-based MP2/aug-cc-pVDZ and MRCI/aug-cc-pVDZ levels. In these scans, the reactants are maintained in their equilibrium geometries while only the distance between the OH and CH_3NH_2 molecules is adjusted. The benchmark classical energies are calculated using the most accurate single-point energies and all the previously-mentioned corrections. The benchmark relative classical energies are obtained from the following sum:

$$E_{cl} = CCSD(T)\text{-}F12b/aug\text{-}cc\text{-}pVQZ + \delta[T] + \delta[(Q)] + \Delta_{core} + \Delta_{rel} + \Delta_{SO} \qquad (96)$$

except in a few instances where any of the aforementioned terms cannot be utilized due to convergence problems. The benchmark relative adiabatic energies are determined with the following expression:

$$E_{ad} = E_{cl} + \Delta_{ZPE} \qquad (97)$$

where Δ_{ZPE} represents the zero-point energy corrections derived from the CCSD(T)-F12b/aug-cc-pVTZ level of theory. If harmonic frequencies calculated at the CCSD(T)-F12b/aug-cc-pVTZ level are not available, the zero-point energy obtained from the most accurate level (MP2/aug-cc-pVDZ or CCSD(T)-F12b/aug-cc-pVDZ) is added to the classical energy. Finally, the reaction rate coefficients at various temperatures for the H-abstraction reaction are determined using transition state theory (TST) based on the benchmark energy barrier, rotational constants and harmonic vibrational frequencies obtained from the present computations. The rate coefficients are also determined with the tunneling effect taken into account utilizing the Wigner approximation.

3.1.2.2 Results

The entrance channel is investigated using one-dimensional scans considering 11 different orientations of the reactants as **Figure 10** shows. Among these, 4 orientations

involve the OH radical approaching CH₃NH₂ with its H atom as there is a possibility of forming an H-bond between the two molecules.
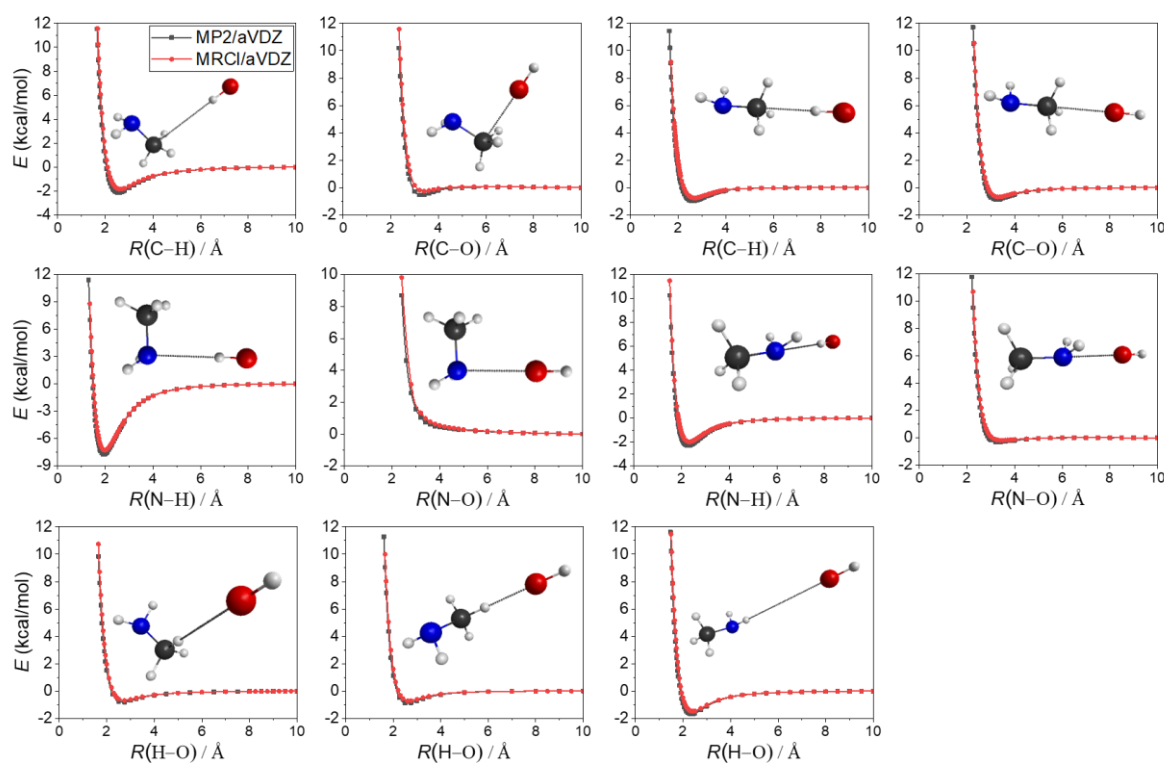

Figure 10. Potential energy curves for the entrance channel, computed in various directions at the MP2/aug-cc-pVDZ (black) and MRCI/aug-cc-pVDZ (red) levels of theory, with the OH and CH₃NH₂ molecules fixed in their equilibrium geometries and only one distance (dotted bond) being modified. Taken from Ref. [6].

Additionally, 7 orientations are considered where the OH radical approaches the CH₃NH₂ molecule with its O atom. With one exception, a minimum can be observed in each orientation except for the case where the OH radical approaches the N atom of the CH₃NH₂ molecule with its O atom forming a 90° angle with the C-N bond. This phenomenon can be attributed to the repulsion between the non-bonding electrons of the N and O atoms. The minima typically occur at distances between 2.0 and 2.5 Å, which can be interpreted as the range for the H-bond length. The depths of these minima are generally shallow with the maximum depths usually around 2 kcal/mol except in one case where a deeper minimum of 8 kcal/mol is observed. This exception occurs when the H side of the OH molecule approaches the N atom perpendicularly to the C–N bond. The performance difference

between the two methods used (MP2 and MRCI) is minimal; the behavior of the curves and the positions of the minima are quite similar.

A total of 6 different product channels are considered for the OH + CH$_3$NH$_2$ reaction. H-abstraction can occur on either side of the CH$_3$NH$_2$ molecule. If the reaction takes place on the CH$_3$ side (CH$_3$ HA), the products are H$_2$O + CH$_2$NH$_2$. Conversely, if the OH radical abstracts an H from the NH$_2$ group (NH$_2$ HA), the products are H$_2$O + CH$_3$NH. When OH and CH$_3$NH$_2$ molecules collide, substitution reactions in addition to abstraction can also occur. Depending on which atom or group is replaced by OH in the CH$_3$NH$_2$ molecule, we distinguish between H-, NH$_2$- and CH$_3$-substitution reactions. In H-substitution reactions, the process can take place on either the CH$_3$ or NH$_2$ groups of the CH$_3$NH$_2$ molecule and the process results in the CH$_3$NHOH + H and CH$_2$OHNH$_2$ + H products, respectively. For H-substitution on the CH$_3$ group, both Walden (CH$_3$ HS W) and front-side (CH$_3$ HS FS) mechanism pathways have been observed. On the other hand, for H-substitution on the NH$_2$ group only the stationary points associated with the Walden (NH$_2$ HS W) mechanism have been identified. Furthermore, if the NH$_2$ (AS) or CH$_3$ group (MS) of the CH$_3$NH$_2$ molecule is replaced by the OH radical, the reaction yields the following products: CH$_3$OH + NH$_2$ and NH$_2$OH + CH$_3$. In the case of NH$_2$-substitution reactions, there is also the possibility that the reaction occurs via either the Walden (AS W) or front-side (AS FS) mechanism.

Figure 11 shows the stationary points and relative energies along the various reaction channels that can occur during the OH + CH$_3$NH$_2$ reaction. Out of the 6 product channels, 3 are exothermic and 3 are endothermic. The most exothermic is the CH$_3$-H-abstraction product channel with a classical(adiabatic) relative energy of −25.58(−26.23) kcal/mol followed by the NH$_2$-H-abstraction channel, where the classical(adiabatic) relative energy of the products is −17.93(−19.32) kcal/mol. The classical(adiabatic) energy barrier for CH$_3$-H-abstraction is −0.09(0.20) kcal/mol and for NH$_2$-H-abstraction, it is −0.72(−1.35) kcal/mol. Therefore, observing only the relative classical energies of the transition states, it can be concluded that both reactions proceed without a barrier. If we consider the relative adiabatic energies, the CH$_3$-H-abstraction has a very slight barrier, while the energy barrier for NH$_2$-H-abstraction decreases further compared to the classical value.
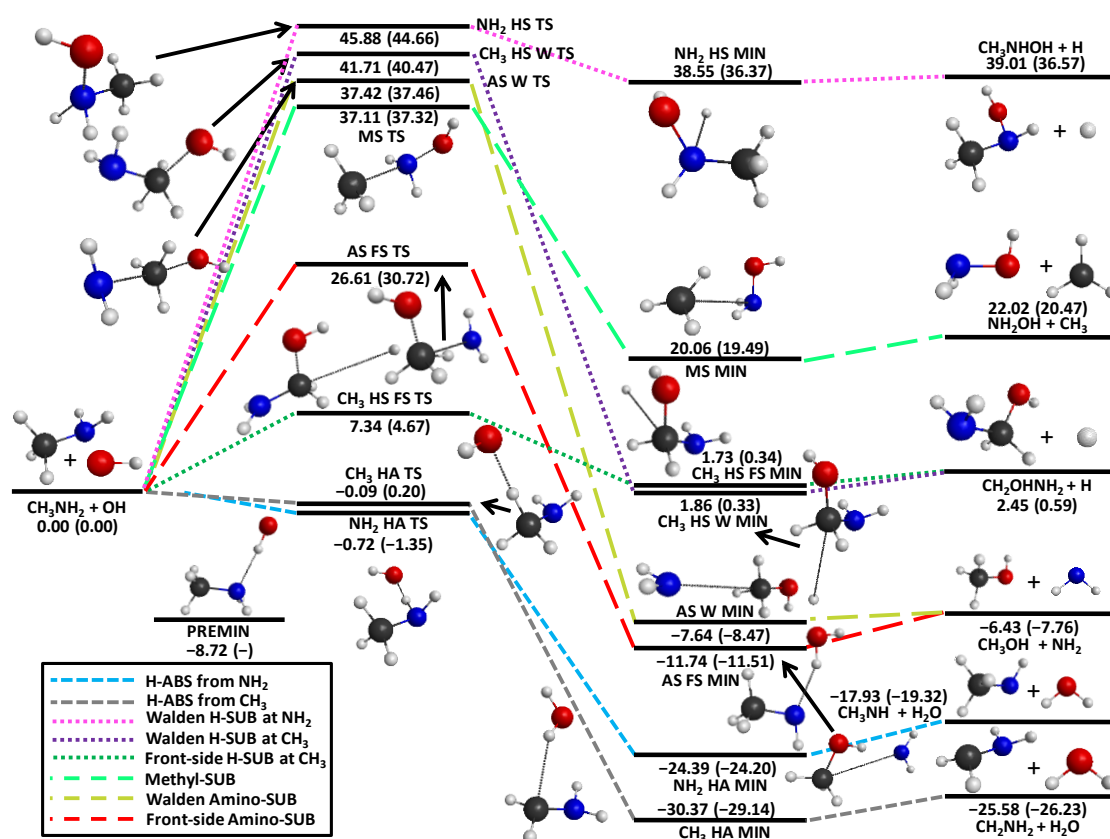
Figure 11. The most accurate optimized geometries and classical(adiabatic) benchmark energies of the lowest-energy conformers relative to the reactants for the OH + CH$_3$NH$_2$ reaction. Taken from Ref. [6].

Based on this, it can be concluded that the H-abstraction channel will be dominant in the OH + CH$_3$NH$_2$ reaction as this reaction is the most favorable both kinetically and thermodynamically. The relative energies of the transition states for substitution reactions are significantly positive in all cases. The H-substitution reaction on the CH$_3$ group via the front-side mechanism has the lowest relative classical(adiabatic) energy barrier with a value of 7.34(4.67) kcal/mol. Following this, the energy barriers in increasing order are as follows: front-side mechanism NH$_2$ substitution, CH$_3$ substitution, Walden mechanism NH$_2$ substitution, Walden mechanism H-substitution on the CH$_3$ group and finally, the highest energy barrier is for H-substitution on the NH$_2$ group. It can be observed that H-substitution on the NH$_2$ group is not only the most kinetically hindered reaction, but also the most thermodynamically hindered. The relative classical(adiabatic) energy of the CH$_3$NHOH + H product channel, which is 39.01(36.57) kcal/mol, significantly exceeds that of the products with the second highest relative energy, which are formed in the CH$_3$-substitution reaction

and their relative classical(adiabatic) energy is 22.02(20.47) kcal/mol. Among the endothermic reaction pathways, the H-substitution reaction on the CH_3 group has the lowest reaction enthalpy. The classical(adiabatic) energy of the resulting CH_2OHNH_2 + H products is 2.45(0.59) kcal/mol above the energy of the reactants. Furthermore, among the exothermic reaction pathways, the least exothermic is the NH_2-substitution, which produces CH_3OH and CH_3 molecules. The classical(adiabatic) energy of these products is 6.43(7.76) kcal/mol below that of the reactants. The energy order of the minima corresponds to the order of the products. Where two mechanisms are possible within a given reaction channel, the front-side mechanism for NH_2-substitution and the Walden mechanism for H-substitution on the CH_3 group result in the post reaction minima with lower relative energy. It can be noted that, in this reaction, the front-side mechanism requires less energy to reach the transition state, whether for H-substitution on the CH_3 group or for NH_2-substitution. In the case of H-substitution on the CH_3 group, the difference in relative classical(adiabatic) energies between the Walden and front-side transition states is 34.37(35.80) kcal/mol. For NH_2-substitution, this difference is 10.81(6.74) kcal/mol. For the H-substitution on the CH_3 group and NH_2-substitution   reactions, the preference for the front-side transition states can be attributed to steric effects and/or hydrogen bond interactions, which are not possible in the Walden configurations.

In this study, several conformers of the transition states, post-reaction complexes, and products are successfully identified. The most accurate optimized geometries along with their classical and adiabatic energies are illustrated in Figure 12-Figure 14. For the transition states except for the CH_3 substitution, NH_2 substitution via the Walden mechanism and CH_3-H substitution via Walden inversion reaction pathways, multiple conformers of the transition states can be observed. The CH_3-H-abstraction reaction pathway exhibits the greatest number of conformer structures. In this scenario, five distinct first-order saddle points are identified on the potential energy surface. The lowest energy conformer has a classical(adiabatic) energy of −0.09(0.20) kcal/mol relative to the reactants. This reaction pathway includes two transition states with energies near that of the lowest-energy conformer and two additional transition states with considerably higher relative energies. The classical(adiabatic) energy difference between the highest- and lowest-energy NH_2 H-abstraction transition state is just 0.06(0.05) kcal/mol.
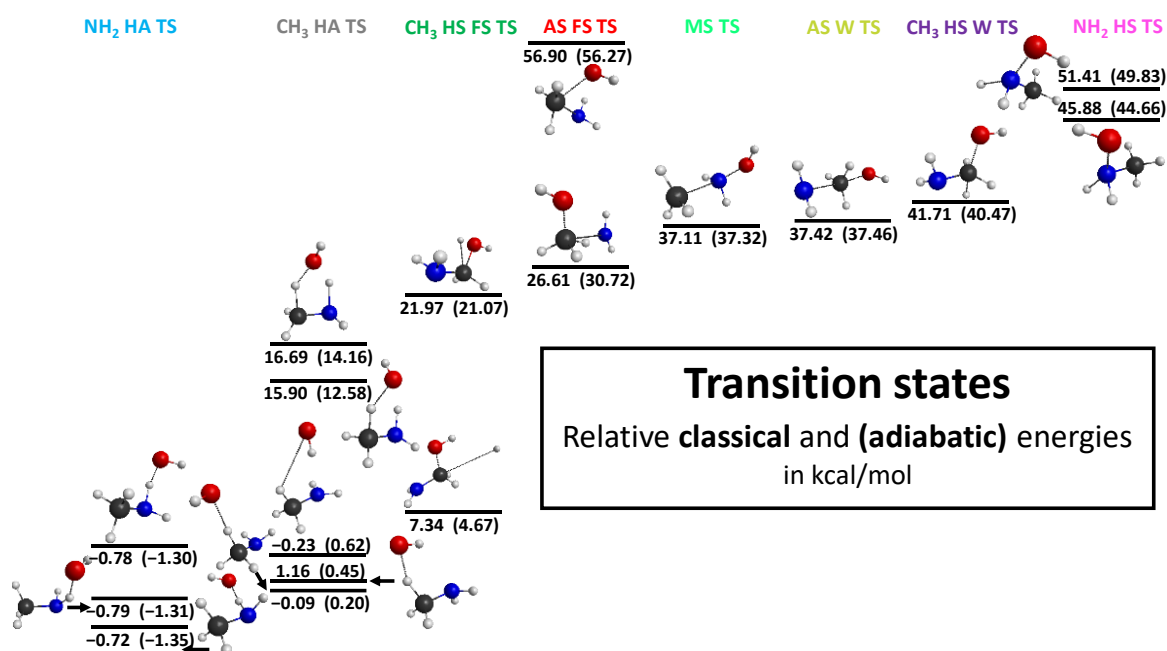
Figure 12. Different transition-state structures for the OH + CH_3NH_2 reaction with a focus on the benchmark classical and adiabatic energies relative to the reactants. Taken from Ref. [6].

Interestingly, the lowest energy CH_3 and NH_2 H-abstraction transition-state structures are very similar differing only in the positioning of the OH group, while the CH_3NH_2 molecule retains the same structure in both cases. Additionally, 2-2-2 conformer structures have been identified for H-substitution via the front-side mechanism on the CH_3 group, NH_2 substitution via the front-side mechanism and H-substitution on the NH_2 group. For these reaction pathways, the transition-state structures for H-substitution via the front-side mechanism on the CH_3 group and NH_2 substitution via the front-side mechanism exhibit relatively larger energy differences, whereas smaller energy differences are observed among the transition states for H-substitution on the NH_2 group. It can be observed that apart from H-abstraction on the NH_2 group two different post-reaction complex structures are obtained for each reaction pathway. The energy differences between the two structures within a reaction pathway are generally small and the energies of the structures corresponding to the minima in the product channel of the Walden inversion NH_2 substitution are identical to the hundredth of a kcal/mol. The largest energy difference is observed in the case of CH_3 substitution, which is 4.22(4.09) kcal/mol classicallly(adiabatically).
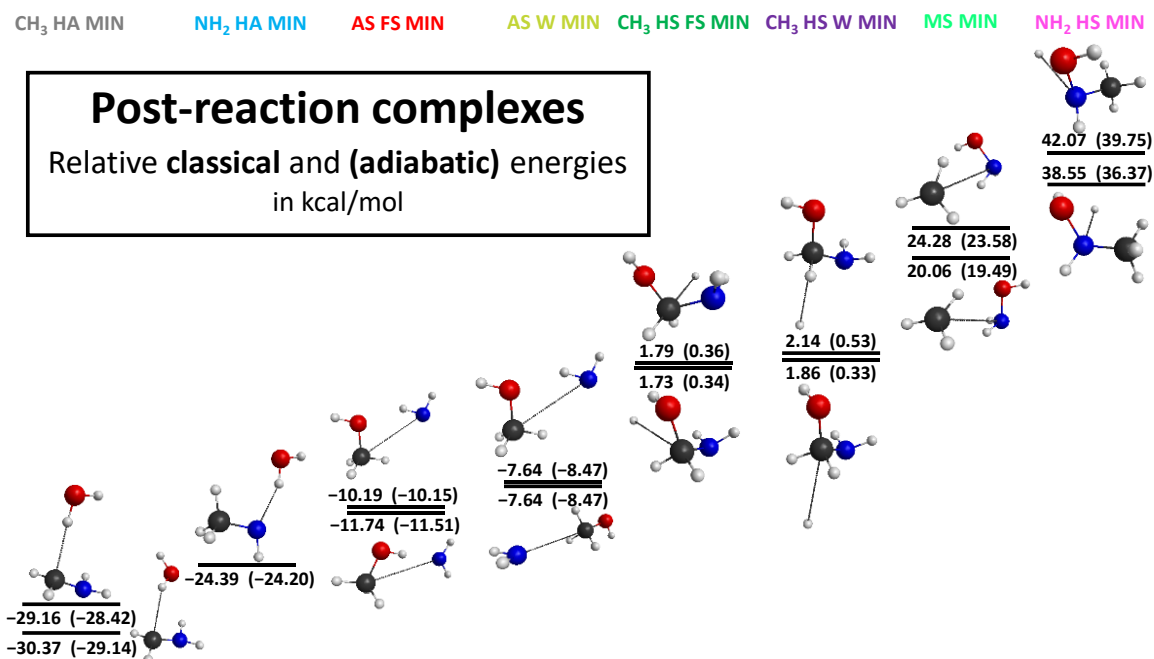
Figure 13. Different post-reaction complex structures for the OH + CH₃NH₂ reaction with a focus on the benchmark classical and adiabatic energies relative to the reactants. Taken from Ref. [6].

The lowest-energy post-reaction complex occurs in the case of H-abstraction on the CH₃ group, which also represents the global minimum of the entire potential energy surface. Additionally, it is interesting to note that the energy order of the transition states and post-reaction complexes differs among the various reaction pathways, and the highest-energy stationary points are observed in both cases for the NH₂ H-substitution reaction pathway. Moreover, conformers are obtained for the NH₂OH + CH₃ and CH₃NHOH + H₂O product channels. For the methyl substitution, both cis and trans conformers of the NH₂OH molecule are distinguished, with the trans structure having the lower energy. The classical(adiabatic) energy difference between the cis and trans structures is 4.22(4.06) kcal/mol. For the H-substitution at the NH₂ group, the orientations of the CH₃ group and the OH part can vary, resulting in an energy difference of 3.49(3.38) kcal/mol classically (adiabatically).

Table *4* summarizes the results of the energy calculations for the stationary points of the OH + CH₃NH₂ reaction at different theoretical levels. The structure optimizations, energy and harmonic frequency computations are performed at three different theoretical levels for the optimized geometries: MP2/aug-cc-pVDZ, CCSD(T)-F12b/aug-cc-pVDZ and

CCSD(T)-F12b/aug-cc-pVTZ. For the subsequent single-point calculations including CCSD(T)-F12b/aug-cc-pVQZ computations and the determination of five energy corrections, the most accurate previously-determined geometries are utilized.
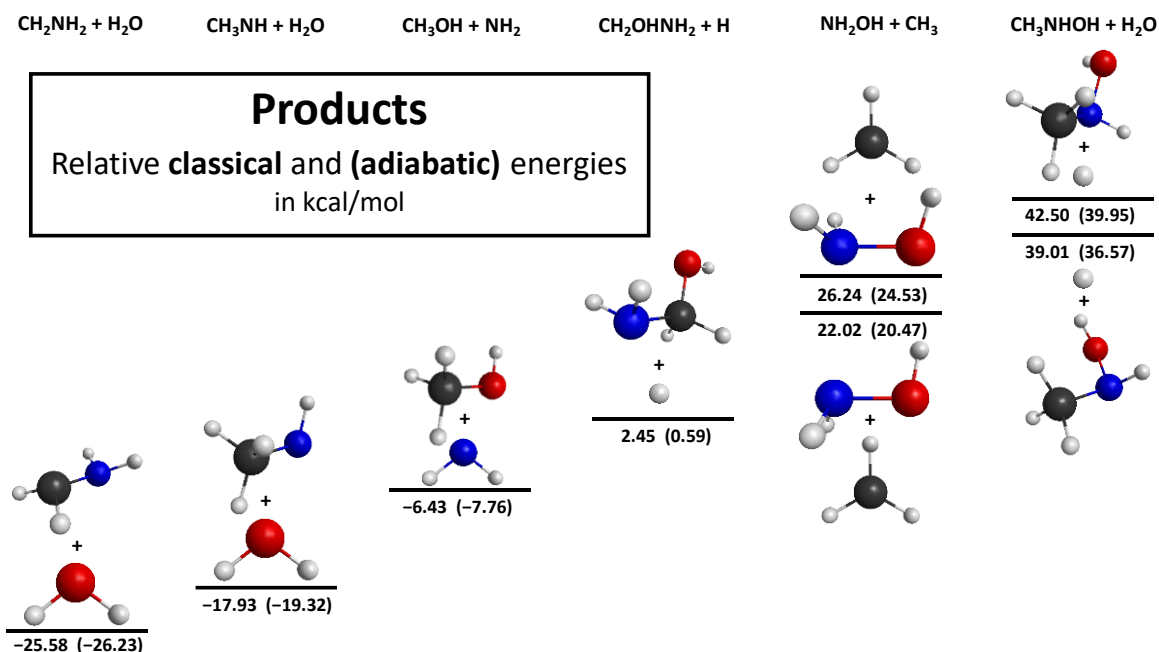

Figure 14. Different product structures for the OH + CH$_3$NH$_2$ reaction with a focus on the benchmark classical and adiabatic energies relative to the reactants. Taken from Ref. [6].

As we transition from the MP2/aug-cc-pVDZ level to the CCSD(T)-F12b/aug-cc-pVTZ level of theory, the energy differences relative to CCSD(T)-F12b/aug-cc-pVQZ decrease. The discrepancies between the CCSD(T)-F12b/aug-cc-pVTZ and CCSD(T)-F12b/aug-cc-pVQZ energies are generally only a few hundredths of kcal/mol indicating the excellent basis set convergence of the CCSD(T)-F12b method. The difference between the MP2/aug-cc-pVDZ and CCSD(T)-F12b/aug-cc-pVQZ results is relatively small, but in some cases, such as CH3 HS FS TS 1, AS FS TS 2, MS TS, CH3 HS FS MIN 1, CH3 HS FS MIN 2, CH3 HS W MIN 1, CH3 HS W MIN 2, NH2 HS MIN 1, NH2 HS MIN 2, CH3NHOH(2) + H and CH2OHNH2 + H, this difference can reach up above 5 kcal/mol. In most instances, the δ[CCSDT] and δ[CCSDT(Q)] values are negative and the absolute magnitudes of these energy contributions are typically small. The core correlation energies (Δcore) typically remain below 0.30 kcal/mol in absolute value with the exceptions being the AS W TS, AS FS TS 2, MS TS, and NH2 HS TS 2

transition states, where the core correlation contributions are 0.48, 0.55, 0.44, and 0.31 kcal/mol, respectively.

Table 4. Energy (kcal/mol) and additional energy contributions (kcal/mol) for the stationary points including the OH + CH$_3$NH$_2$ reaction products relative to the reactants at various computational levels. The table is taken from Ref. [6].

Stationary point	MP2 DZ[a]	CCSD(T)−F12b DZ[b]	TZ[c]	QZ[d]	$\delta[T]$[e]	$\delta[(Q)]$[f]	Δ_{core}[g]	Δ_{rel}[h]	Δ_{SO}[i]	Classical[j]	Δ_{ZPE}[k]	Adiabatic[l]
CH$_3$ HA TS 1	3.69	−0.35	–	−0.10[m]	−0.14[m]	−0.06[m]	−0.01[m]	−0.01[m]	0.19	−0.109	0.29	0.20
CH$_3$ HA TS 2	4.37	1.07	1.25	1.29	−0.17	−0.15	−0.03	0.03	0.19	1.16	−0.71	0.45
CH$_3$ HA TS 3	−0.34	−0.57[m]	–	−0.31[m]	−0.01[m]	−0.02[m]	−0.08[m]	−0.07[m]	0.12	−0.23	0.85	0.62
CH$_3$ HA TS 4	14.83	13.96[m]	–	16.48	−0.21	−0.58	−0.04	0.06	0.19	15.90	−3.32	12.58
CH$_3$ HA TS 5	15.50	–	–	17.24	−0.19	−0.58	−0.03	0.06	0.19	16.69	−2.53	14.16
CH$_3$ HS FS TS 1	0.88	6.56	7.24[m]	7.23	0.10	−0.20	−0.15	0.17	0.19	7.34	−2.67	4.67
CH$_3$ HS FS TS 2	18.53	21.31	21.99	22.09	−0.03	−0.33	0.01	0.04	0.19	21.97	−0.90	21.07
CH$_3$ HS W TS	43.18	–	–	41.82	−0.20	−0.36	0.22	0.04	0.19	41.71	−1.24	40.47
AS W TS	43.83	37.97	38.03	38.15	−0.76	−0.57	0.48	−0.07	0.19	37.42	0.04	37.46
AS FS TS 1	27.23	26.55	26.57	26.60	−0.11	−0.15	−0.05	0.13	0.19	26.61	4.11	30.72
AS FS TS 2	70.29	58.25	58.01	58.49	−1.55	−0.70	0.55	−0.08	0.19	56.90	−0.63	56.27
MS TS	44.66	37.91	37.69	37.76	−0.66	−0.55	0.44	−0.07	0.19	37.11	0.21	37.32
NH$_2$ HA TS 1	−2.17	−0.76[m]	–	−0.37[m]	−0.31[m]	−0.27[m]	0.03[m]	0.01[m]	0.19	−0.72	−0.63	−1.35
NH$_2$ HA TS 2	−2.09	−0.85[m]	–	−0.43[m]	−0.33[m]	−0.27[m]	0.04[m]	0.01[m]	0.19	−0.79	−0.52	−1.31
NH$_2$ HA TS 3	−2.09	−0.85[m]	–	−0.42[m]	−0.33[m]	−0.27[m]	0.04[m]	0.01[m]	0.19	−0.78	−0.52	−1.30
NH$_2$ HS TS 1	46.45	45.68	46.01	46.10	−0.15	−0.52	0.28	−0.02	0.19	45.88	−1.22	44.66
NH$_2$ HS TS 2	51.06	51.16	51.51	51.60	−0.11	−0.54	0.31	−0.04	0.19	51.41	−1.58	49.83
PREMIN	−8.98[m]	−8.71[m]	−8.61[m]	−8.47[m]	−0.12[m]	−0.10[m]	−0.04[m]	0.01[m]	0.01	−8.71	–	–
CH$_3$ HA MIN 1	−32.20	−30.28	−30.22	−30.25	−0.04	−0.17	−0.25	0.15	0.19	−30.37	1.23	−29.14
CH$_3$ HA MIN 2	−30.94	−29.10	−29.00[m]	−29.03	−0.04[m]	−0.17	−0.26	0.15	0.19	−29.16	0.74	−28.42
CH$_3$ HS FS MIN 1	−4.77	0.94	1.56[m]	1.56	0.10	−0.22	−0.03	0.13	0.19	1.73	−1.39	0.34
CH$_3$ HS FS MIN 2	−4.72	1.00	1.62[m]	1.62	0.10	−0.22	−0.03	0.13	0.19	1.79	−1.43	0.36
CH$_3$ HS W MIN 1	−4.68	1.07	1.69[m]	1.69	0.10	−0.22	−0.03	0.13	0.19	1.86	−1.53	0.33
CH$_3$ HS W MIN 2	−4.46	1.35	1.98[m]	1.97	0.10	−0.21	−0.04	0.13	0.19	2.14	−1.61	0.53
AS W MIN 1	−8.59	−8.10[m]	−7.95[m]	−7.90	−0.06	−0.07	0.17	0.03	0.19	−7.64	−0.83	−8.47
AS W MIN 2	−8.57	−8.09	−7.94	−7.90	−0.06	−0.07	0.17	0.03	0.19	−7.64	−0.83	−8.47
AS FS MIN 1	−12.69	−12.24	−12.06[m]	−11.98	−0.06	−0.08	0.14	0.05	0.19	−11.74	0.23	−11.51
AS FS MIN 2	−11.12	−10.60	−10.48	−10.42	−0.06	−0.08	0.14	0.04	0.19	−10.19	0.04	−10.15
MS MIN 1	19.54	19.87	19.92	19.96	−0.05	−0.22	0.13	0.05	0.19	20.06	−0.57	19.49
MS MIN 2	23.89	24.05	24.12	24.16	−0.05	−0.21	0.15	0.04	0.19	24.28	−0.70	23.58
NH$_2$ HA MIN	−25.25	−24.63	−24.46	−24.43	−0.10	−0.09	−0.02	0.06	0.19	−24.39	0.19	−24.20
NH$_2$ HS MIN 1	33.25	37.78	38.39	38.45	0.08	−0.32	0.09	0.06	0.19	38.55	−2.18	36.37
NH$_2$ HS MIN 2	36.91	41.24	41.89	41.94	0.09	−0.31	0.10	0.06	0.19	42.07	−2.32	39.75
CH$_3$NHOH(1)+H	37.20	41.66	42.32	42.37	0.09	−0.31	0.10	0.06	0.19	42.50	−2.55	39.95
CH$_3$NHOH(2)+H	33.51	38.21	38.85	38.90	0.09	−0.31	0.08	0.06	0.19	39.01	−2.44	36.57
NH$_2$OH(1)+CH$_3$	26.12	26.24	26.15	26.09	−0.04	−1.19	0.15	0.04	0.19	26.24	−1.71	24.53
NH$_2$OH(2)+CH$_3$	21.69	22.04	21.94	21.88	−0.04	−1.20	0.14	0.05	0.19	22.02	−1.55	20.47
CH$_2$OHNH$_2$+H	−4.26	1.64	2.29	2.28	0.10	−0.21	−0.04	0.13	0.19	2.45	−1.86	0.59
CH$_3$OH+NH$_2$	−7.07	−6.72	−6.70	−6.71	−0.05	−0.06	0.17	0.03	0.19	−6.43	−1.33	−7.76
CH$_3$NH+H$_2$O	−18.49	−18.03	−17.97	−18.03	−0.09	−0.07	0.03	0.04	0.19	−17.93	−1.39	−19.32
CH$_2$NH$_2$+H$_2$O	−27.04	−25.27	−25.36	−25.50	−0.03	−0.14	−0.24	0.14	0.19	−25.58	−0.65	−26.23

[a] MP2/aug-cc-pVDZ relative energies computed at MP2/aug-cc-pVDZ geometries.

[b] CCSD(T)-F12b/aug-cc-pVDZ relative energies computed at CCSD(T)-F12b/aug-cc-pVDZ geometries.

[c] CCSD(T)-F12b/aug-cc-pVTZ relative energies computed at CCSD(T)-F12b/aug-cc-pVTZ geometries.

[d] CCSD(T)-F12b/aug-cc-pVQZ relative energies computed at most accurate geometries.

[e] Eq. (91). [f] Eq. (92). [g] Eq. (93). [h] Eq. (94). [i] Eq. (95). [j] Eq. (96).

[k] ZPE correction determined at the most accurate (available) theoretical level.

[l] Eq. (97).

[m] The ManyHF method is utilized.

Scalar relativistic effects (Δ_{rel}) are generally positive but can occasionally be negative. Typically, these effects are small ranging from 0.00 to 0.15 kcal/mol. The highest Δ_{rel} value, 0.17 kcal/mol, is observed for the CH_3 HS FS TS 1 transition state. The non-relativistic ground state of the OH radical splits into higher and lower energy levels due to spin-orbit interaction. This causes a decrease in the energy of the reactants while increasing all relative energies by 0.19 kcal/mol due to the spin-orbit correction (Δ_{SO}) except for the CH_3 HA TS 3 and PREMIN stationary points, where Δ_{SO} is only 0.12 kcal/mol and 0.01 kcal/mol respectively. This smaller Δ_{SO} for CH_3 HA TS 3 and PREMIN can be attributed to its reactant-like structure, where the OH is relatively distant from the CH_3NH_2 molecule. Consequently, the spin-orbit interaction has a significant effect at this geometry resulting in a smaller increase in the relative energy. The ZPE corrections are generally negative ranging from 0.0 to −2.5 kcal/mol. The largest ZPE correction is observed for the AS FS TS 1 transition state with a value of 4.11 kcal/mol. **Table 5** provides a comparison between the theoretical adiabatic energies we have obtained and the 0 K reaction enthalpies calculated using the Active Thermochemical Tables (ATcT) data, similar to the comparison made for the OH + C_2H_6 reaction.

Table 5. Comparison between the currently available best "experimental" results and the 0 K reaction enthalpies determined by us for the OH + CH_3NH_2 reaction. The values are given in kcal/mol units. The table is taken from Ref. [6].

Reaction	Theory[a]	ATcT[b]
OH + $CH_3NH_2 \rightarrow CH_2NH_2 + H_2O$	−26.23	−26.35 ± 0.14
OH + $CH_3NH_2 \rightarrow CH_3NH + H_2O$	−19.32	−19.53 ± 0.11
OH + $CH_3NH_2 \rightarrow CH_3OH + NH_2$	−7.76	−7.63 ± 0.07
OH + $CH_3NH_2 \rightarrow NH_2OH$ (trans) + CH_3	20.47	20.53 ± 0.11
OH + $CH_3NH_2 \rightarrow NH_2OH$ (cis) + CH_3	24.53	24.76 ± 0.34

[a] Benchmark relative adiabatic energy calculated in this work.
[b] Data obtained from the Active Thermochemical Tables (ATcT).

It can be observed that the reaction enthalpies derived from the ATcT heats of formation match our benchmark adiabatic energies very closely with three cases ($CH_2NH_2 + H_2O$,

NH₂OH(trans) + CH₃ and NH₂OH(cis) + CH₃) showing exact agreement within the margin of error.

Table 6. Comparison of the rate coefficients calculated by us with the theoretical and experimental data available in the literature. The table is taken from Ref. [6].

	This work		Tian[a]			Atkinson at al.[b]	Carl and Crowley[c]	Butkovskaya and Setzer[d]	Onel at al.[e]
T / K	TST	TST + W. T. Correction	TST	ICVT	ICVT/SCT				
295	6.71×10^{-12}	1.03×10^{-11}					$(1.73 \pm 0.11) \times 10^{-11}$		
298	6.61×10^{-12}	1.01×10^{-11}						$(2.00 \pm 0.40) \times 10^{-11}$	$(1.97 \pm 0.11) \times 10^{-11}$
299	6.58×10^{-12}	1.00×10^{-11}	2.15×10^{-10}	1.36×10^{-11}	2.98×10^{-11}	$(2.20 \pm 0.22) \times 10^{-11}$			
300	6.55×10^{-12}	9.95×10^{-12}	2.14×10^{-10}	1.37×10^{-11}	2.96×10^{-11}				
353.9	5.56×10^{-12}	7.45×10^{-12}	1.87×10^{-10}	1.39×10^{-11}	2.56×10^{-11}	$(1.94 \pm 0.20) \times 10^{-11}$			
400	5.26×10^{-12}	6.56×10^{-12}	1.80×10^{-10}	1.42×10^{-11}	2.40×10^{-11}				
426.1	5.22×10^{-12}	6.31×10^{-12}	1.75×10^{-10}	1.42×10^{-11}	2.28×10^{-11}	$(1.75 \pm 0.18) \times 10^{-11}$			
500	5.39×10^{-12}	6.13×10^{-12}	1.78×10^{-10}	1.48×10^{-11}	2.16×10^{-11}				
550	5.68×10^{-12}	6.29×10^{-12}	1.84×10^{-10}	1.54×10^{-11}	2.14×10^{-11}				
600	6.07×10^{-12}	6.59×10^{-12}	1.94×10^{-10}	1.61×10^{-11}	2.16×10^{-11}				
650	6.55×10^{-12}	7.00×10^{-12}	2.06×10^{-10}	1.70×10^{-11}	2.21×10^{-11}				
700	7.11×10^{-12}	7.51×10^{-12}	2.21×10^{-10}	1.80×10^{-11}	2.28×10^{-11}				
800	8.43×10^{-12}	8.77×10^{-12}	2.56×10^{-10}	2.05×10^{-11}	2.49×10^{-11}				
900	1.00×10^{-11}	1.03×10^{-11}	3.00×10^{-10}	2.37×10^{-11}	2.78×10^{-11}				
1000	1.19×10^{-11}	1.22×10^{-11}	3.55×10^{-10}	2.76×10^{-11}	3.17×10^{-11}				
1050	1.30×10^{-11}	1.33×10^{-11}	3.81×10^{-10}	2.94×10^{-11}	3.35×10^{-11}				
1250	1.81×10^{-11}	1.83×10^{-11}	5.19×10^{-10}	3.93×10^{-11}	4.33×10^{-11}				
1500	2.64×10^{-11}	2.66×10^{-11}	7.46×10^{-10}	4.41×10^{-11}	4.67×10^{-11}				
1750	3.73×10^{-11}	3.75×10^{-11}	1.04×10^{-9}	5.94×10^{-11}	6.17×10^{-11}				
2000	5.11×10^{-11}	5.14×10^{-11}	1.40×10^{-9}	7.81×10^{-11}	8.05×10^{-11}				
2200	6.45×10^{-11}	6.47×10^{-11}	1.74×10^{-9}	9.56×10^{-11}	9.81×10^{-11}				
2400	8.01×10^{-11}	8.04×10^{-11}	2.15×10^{-9}	1.12×10^{-10}	1.14×10^{-10}				
2500	8.88×10^{-11}	8.91×10^{-11}	2.36×10^{-9}	1.20×10^{-10}	1.22×10^{-10}				
2800	1.19×10^{-10}	1.19×10^{-10}	3.10×10^{-9}	1.45×10^{-10}	1.47×10^{-10}				
3000	1.42×10^{-10}	1.42×10^{-10}	3.67×10^{-9}	1.65×10^{-10}	1.67×10^{-10}				

[a] Ref 33. [b] Ref 35. [c] Ref 36. [d] Ref 37. [e] Ref 38.

Table 6 presents the rate coefficients determined by us along with theoretical and experimental values found in the literature. A straightforward comparison of the TST calculations reveals that our determined rate coefficients differ by more than one order of magnitude from those calculated by Tian and coworkers. Additionally, the experimentally-determined values differ by about one order of magnitude from those we obtained. At this point, it is important to note that the rate coefficients provided by Tian and colleagues may

not be reliable, as the data in their article lacks consistency between the figures and the tables. When we account for the tunneling effect in our calculation of the rate coefficients, we observe a reasonably close agreement between our theoretical predictions and the experimental values. Furthermore, our calculated rate coefficients reflect the decreasing trend reported by Atkinson and colleagues over the temperature range of 299-426.1 K, though our results indicate a more pronounced decline.

3.1.3   OH + glycine: H-abstraction

3.1.3.1   Computational details

Initially, the stationary points are identified utilizing chemical intuition employing MP2/3-21G level of theory. This smaller basis set is used to ensure quick calculations and the obtained geometries are then used as starting points for higher-quality computations. Three distinct reaction pathways — CH, NH and COOH — are identified based on the functional group from which the hydrogen atom is abstracted. After at least one minimum (except for COOH) and one saddle point are found for each reaction channel, a systematic mapping is carried out to obtain the conformers of the stationary points. The method for this systematic search is depicted in **Figure 15**.

$$CH-TS \qquad CH-MIN \qquad NH-TS \qquad NH-MIN \qquad COOH-TS$$
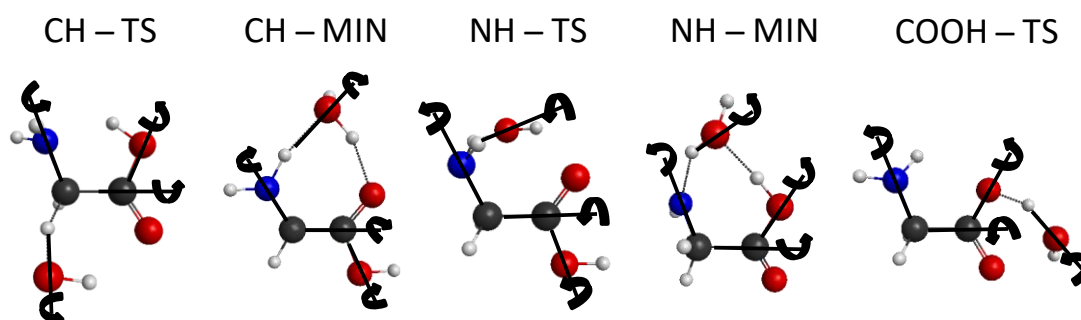
Figure 15. Generation of the initial 1296 geometries by rotating the structures in 60-degree increments around 4 axes. Taken from Ref. [3].

Starting from the lowest-energy conformer of each previously-obtained saddle point and minimum, 6^4 = 1296 initial geometries are generated by varying 4 torsion angles in 60° increments between 0° and 360°. These geometries are then optimized with the MP2 method utilizing the 3-21G basis set. Next, each MP2/3-21G conformer is optimized using the MP2/aug-cc-pVDZ level of theory. Following this, further optimization of the MP2/aug-

cc-pVDZ structures is carried out using the CCSD(T)-F12b/aug-cc-pVDZ level of theory. Additionally, harmonic vibrational frequencies are computed at the two most accurate levels of theory. Single-point energy calculations are carried out using the CCSD(T)-F12b method with two different basis sets, aug-cc-pVTZ and aug-cc-pVQZ, based on the geometries optimized at the CCSD(T)-F12b/aug-cc-pVDZ level. The post-CCSD(T) correlation corrections are calculated utilizing the CCSD(T), CCSDT, and CCSDT(Q) methods with the 6-31G basis set. These corrections are derived from the following equations:

$$\delta[T] = CCSDT/6\text{-}31G - CCSD(T)/6\text{-}31G \tag{98}$$

$$\delta[(Q)] = CCSDT(Q)/6\text{-}31G - CCSDT/6\text{-}31G. \tag{99}$$

Both all-electron (AE) and frozen-core (FC) computations are carried out using the CCSD(T)-F12b/cc-pCVTZ-F12 level of theory. The core-correction is obtained by subtracting the FC energies from the AE ones as follows:

$$\Delta_{core} = AE\text{-}CCSD(T)\text{-}F12b/cc\text{-}pCVTZ\text{-}F12 - FC\text{-}CCSD(T)\text{-}F12b/cc\text{-}pCVTZ\text{-}F12. \tag{100}$$

Scalar relativistic effects are considered by calculating second-order Douglas–Kroll (DK) relativistic energies at the AE-CCSD(T)/aug-cc-pwCVTZ-DK level of theory, while non-relativistic energies are obtained at the AE-CCSD(T)/aug-cc-pwCVTZ level. The scalar relativistic correction Δ_{rel} is determined by subtracting the non-relativistic energies from the relativistic ones:

$$\Delta_{rel} = DK\text{-}AE\text{-}CCSD(T)/aug\text{-}cc\text{-}pwCVTZ\text{-}DK - AE\text{-}CCSD(T)/aug\text{-}cc\text{-}pwCVTZ. \tag{101}$$

Spin-orbit (SO) corrections are derived using the Breit–Pauli Hamiltonian within the interacting-states approach and the Davidson-corrected multi-reference configuration interaction (MRCI+Q) method with the aug-cc-pVTZ basis set. The MRCI calculations involve an active space of 49 electrons in 25 spatial orbitals, while the $1s^2$ core electrons of the three O, two C, and one N atoms are held fixed. The spin-orbit correction is obtained by computing the difference between the SO_1-ground-state energies and the non-SO_1-ground-state energies as follows:

$$\Delta_{SO} = SO_1(MRCI+Q/aug\text{-}cc\text{-}pVTZ) - non\text{-}SO_1(MRCI+Q/aug\text{-}cc\text{-}pVTZ). \tag{102}$$

To characterize the entrance channel, MRCI calculations are conducted with the geometries of the reactants fixed at their equilibrium configurations. These calculations utilize the 3-21G, aug-cc-pVDZ and aug-cc-pVTZ basis sets as well as the previously-specified active space. To obtain the benchmark classical energies, the most accurate single-point energies are combined with the previously-mentioned energy corrections. These classical energies are defined using the following expression:

$$E_{cl} = \text{CCSD(T)-F12b/aug-cc-pVQZ} + \delta[T] + \delta[(Q)] + \Delta_{core} + \Delta_{rel} + \Delta_{SO}, \qquad (103)$$

except in a few instances where convergence issues prevent obtaining any of the aforementioned terms. The benchmark adiabatic relative energies are calculated by adding the zero-point energy corrections (Δ_{ZPE}) to the benchmark classical energies as follows:

$$E_{ad} = \text{CCSD(T)-F12b/aug-cc-pVQZ} + \delta[T] + \delta[(Q)] + \Delta_{core} + \Delta_{rel} + \Delta_{SO} + \Delta_{ZPE}, \qquad (104)$$

where the zero-point energy corrections are computed using the CCSD(T)-F12b method with the aug-cc-pVDZ basis set.

3.1.3.2 Results

Figure 16 displays the number of initial structures that converged to each specific conformer as labeled by the CCSD(T)-F12b/aug-cc-pVDZ geometry. Using systematic mapping at the MP2/3-21G level, 7 different conformers for the CH saddle points are identified within a 4 kcal/mol relative energy range, which are reduced to 3 conformers at the CCSD(T)-F12b/aug-cc-pVDZ level. Additionally, two more CH saddle points, III_{CH}^{TS} and V_{CH}^{TS}, are identified through chemical intuition. By optimizing the MP2/3-21G geometries at the MP2/aug-cc-pVDZ level, 3 + 2 different CH saddle points are determined. These correspond to the CCSD(T)-F12b/aug-cc-pVDZ conformers, labeled with Roman numerals according to their energy ranking.

Figure 17 illustrates the structures of the CCSD(T)-F12b/aug-cc-pVDZ CH saddle points, arranged according to their increasing classical CCSD(T)-F12b/aug-cc-pVDZ energy. The lowest-energy structure, I_{CH}^{TS}, exhibits the greatest intermolecular stabilization
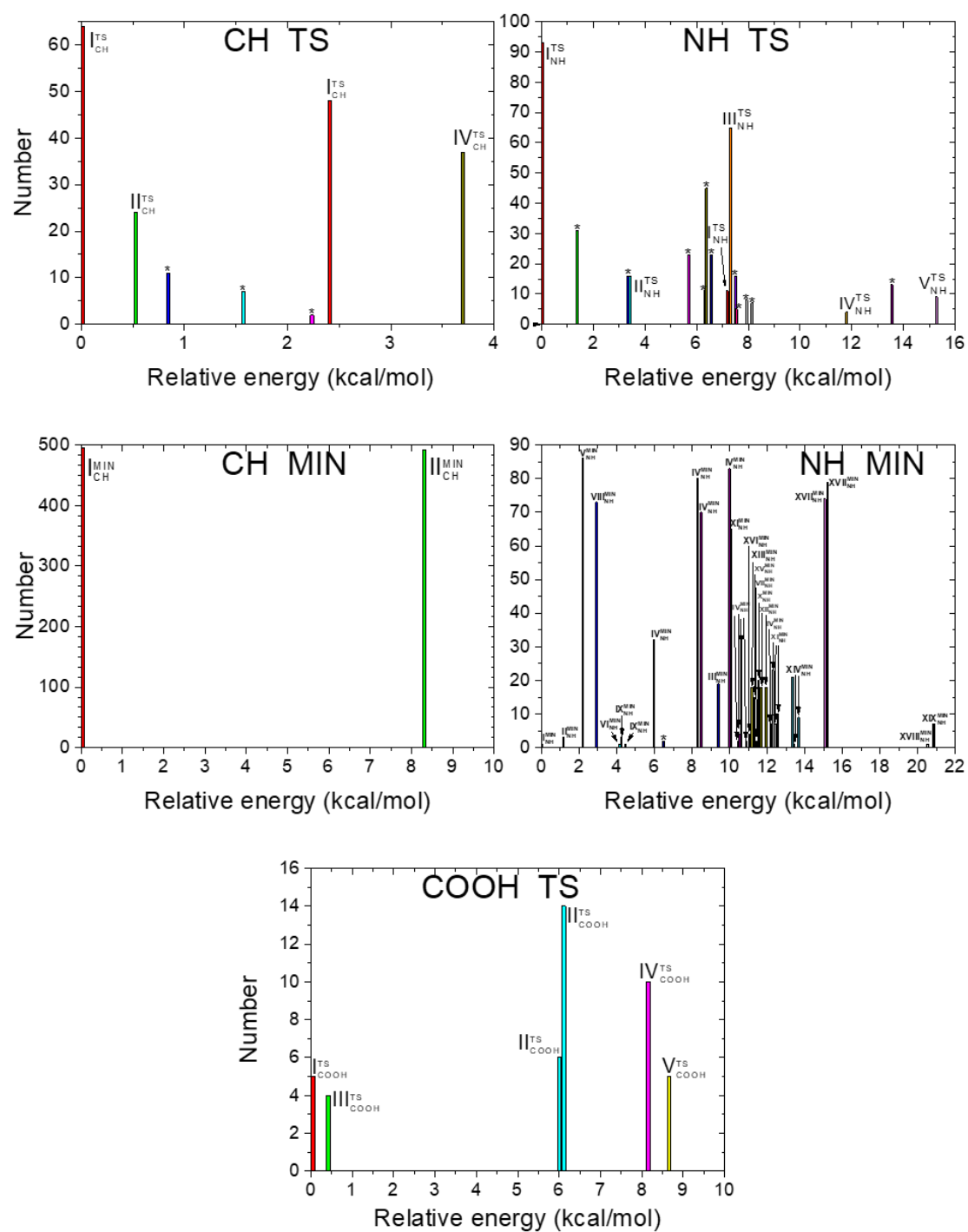
66

Figure 16. The number of initial structures converging to specific conformers at the MP2/3-21G level of theory as a function of the relative energies of transition-state and minimum conformers along various reaction pathways. These conformers are labeled according to their energy order at the CCSD(T)-F12b/aug-cc-pVDZ level. Conformers marked with an asterisk (*) indicate those that do not converge during further optimizations at higher levels of theory. Adapted from Ref. [3].

featuring a trans conformation of the carboxyl group and two hydrogen bonds: one between the amino-N and carboxyl-H and another between the carboxyl-O and hydroxyl-
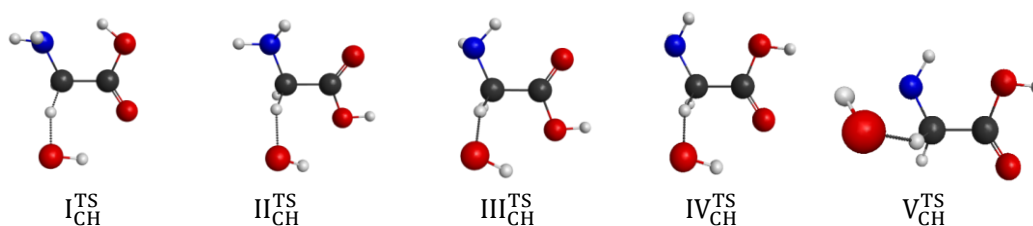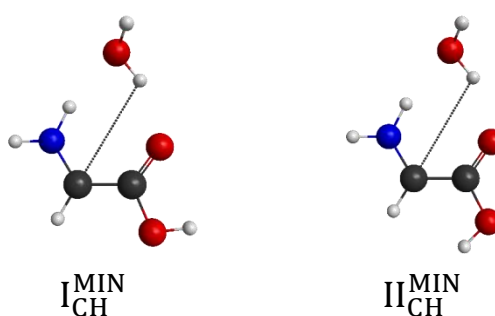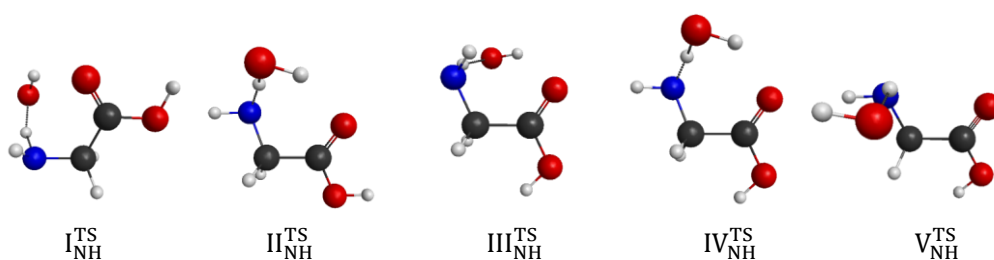

Figure 17. Transition-state structures for H-abstraction from the CH_2 group of glycine computed using the CCSD(T)-F12b/aug-cc-pVDZ theoretical method. Taken from Ref. [3].

H. The second CH saddle point, II_{CH}^{TS}, is higher in energy due to the cis conformation of the carboxyl group. III_{CH}^{TS} also has a cis carboxyl group, but a different positioning of the amino group results in increased energy. Although IV_{CH}^{TS} has a cis-configured carboxyl group, the carbonyl side of this group is positioned closer to the attacking hydroxyl group, similar to the lowest-energy CH saddle point. The V_{CH}^{TS} conformer, having the most unfavorable arrangement, features a cis carboxyl conformation and a hydroxyl-H positioned closer to the amino group, which contributes to its higher energy. When comparing the glycine conformers (Fig. 1), it can be stated that I_{CH}^{TS} bears the closest resemblance to the IIn glycine conformer, while II_{CH}^{TS} aligns with the lowest-energy Ip glycine conformer. Among the CH saddle-point conformers, II_{CH}^{TS} is the one most similar to the lowest-energy product conformer. For the CH minima, the systematic mapping yields just two distinct conformers with comparable probabilities and the number of these stationary points remains consistent with additional optimizations.

Figure 18. Post-reaction complex structures for H-abstraction from the CH_2 group of glycine computed using the CCSD(T)-F12b/aug-cc-pVDZ theoretical method. Taken from Ref. [3].

As depicted in **Figure 16**, there is an energy difference of approximately 8.2 kcal/mol between the two MP2/3-21G minima. **Figure 18** displays the CH minima structures optimized at the CCSD(T)-F12b/aug-cc-pVDZ level. Ultimately, five unique NH saddle points are determined through CCSD(T)-F12b/aug-cc-pVDZ optimization. At the MP2/3-21G level of theory, the NH saddle points span an energy range of 15.2 kcal/mol. The benchmark CCSD(T)-F12b/aug-cc-pVDZ geometries of the NH saddle points are depicted in **Figure 19**.

I_{NH}^{TS} $\quad$ II_{NH}^{TS} $\quad$ III_{NH}^{TS} $\quad$ IV_{NH}^{TS} $\quad$ V_{NH}^{TS}

Figure 19. Transition-state structures for H-abstraction from the NH_2 group of glycine computed using the CCSD(T)-F12b/aug-cc-pVDZ theoretical method. Taken from Ref. [3].

In this instance, NH saddle points with cis-carboxyl groups are more stable than those with trans-isomers. This increased stability is due to the positioning of the C-hydrogens and the carboxyl-hydrogen. The V_{NH}^{TS} conformer is the highest-energy saddle point lacking any stabilizing effects, whereas the first four transition states are stabilized by an H-bond between the reactant-OH and the carbonyl O. The two lowest-energy NH saddle points resemble the Ip glycine conformer and correspond to the Ip_{NH} and IVp_{NH} product conformers. III_{NH}^{TS} and IV_{NH}^{TS} closely match the VIp and VIIIn glycine isomers, respectively and these transition states are most similar to the two highest-energy product conformers in terms of carboxyl group conformation. The highest-energy NH TS is comparable to the VIp and VIIIp glycine conformers, but the amino group of the saddle point is different from that of glycine. Based on the outgoing position of H and the carboxyl group conformation, the highest-energy NH saddle point is most similar to the $VIIp_{NH}$ product conformer. The NH minima exhibit the highest number of conformers. Through the systematic mapping at the MP2/3-21G level of theory, 35 unique structures are identified. Subsequent optimizations yield 19 different conformers at the MP2/aug-cc-pVDZ and CCSD(T)-F12b/aug-cc-pVDZ levels of theory, respectively. The highest-energy MP2/3-21G NH

minimum is 22.7 kcal/mol higher than the lowest-energy conformer. The CCSD(T)-F12b/aug-cc-pVDZ conformers of the NH minima are displayed in **Figure 20**.
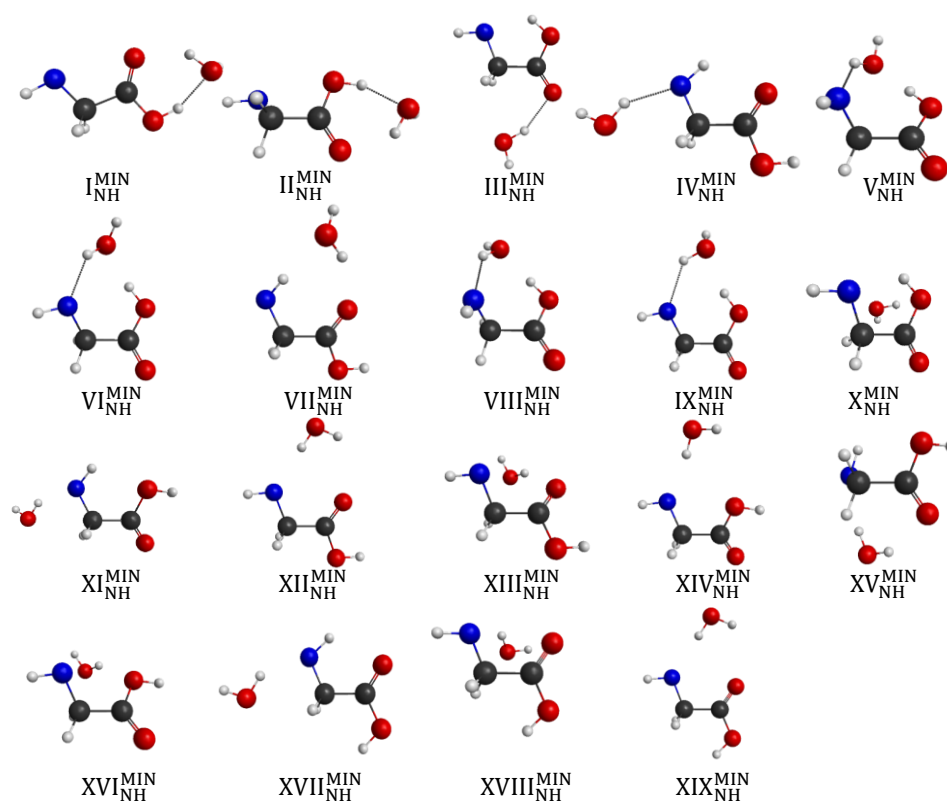

Figure 20. Post-reaction complex structures for H-abstraction from the NH_2 group of glycine computed using the CCSD(T)-F12b/aug-cc-pVDZ theoretical method. Taken from Ref. [3].

In these instances, the H_2O molecule does not consistently position itself near the amino group. For example, in the lowest-energy NH minimum (I_{NH}^{MIN}), the H_2O molecule forms an H-bond with the OH side of the carboxyl group. This arrangement, where the H_2O molecule is closer to the carboxyl group rather than the dehydrogenated amino group, leads to a more stable structure. The two lowest-energy NH minima, I_{NH}^{MIN} and II_{NH}^{MIN}, show significant similarity to the IVn/IVp$_{NH}$ and Vn/Vn$_{NH}$ conformers of glycine/product, respectively. At the MP2/3-21G level, the systematic mapping reveals six distinct saddle points in the carboxyl region, which span an energy range of 8.6 kcal/mol, as illustrated in **Figure 16**. These initial geometries lead to the identification of five different conformers when they are further optimized with higher levels of theory. The CCSD(T)-F12b/aug-cc-pVDZ geometries of these COOH saddle points are shown in Figure 21. In the structure of the lowest-energy conformer, the hydrogens of the CH_2 group are positioned close to the hydroxyl-O, which

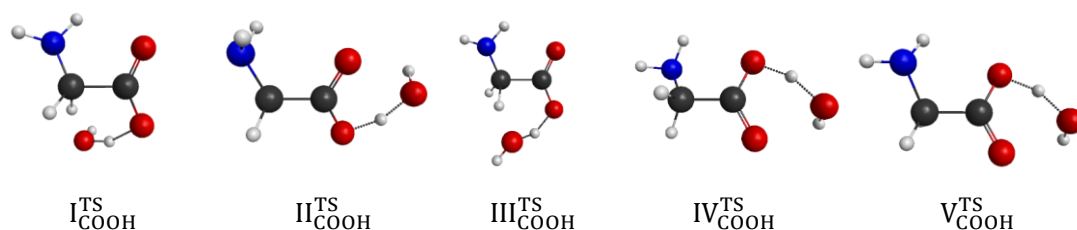may enhance the stabilization provided by the hydrogen bond between the amino-H and one of the carboxyl oxygens.

I_{COOH}^{TS} II_{COOH}^{TS} III_{COOH}^{TS} IV_{COOH}^{TS} V_{COOH}^{TS}

Figure 21. Transition-state structures for H-abstraction from the COOH group of glycine computed using the CCSD(T)-F12b/aug-cc-pVDZ theoretical method. Taken from Ref. [3].

For the COOH saddle points, the hydrogen bond interaction consistently occurs between the amino-H and one of the carboxyl oxygens; no geometries are found where the hydrogen from the reactant OH radical bonds to the amino-N. It is noted that the II_{COOH}^{TS} saddle point resembles the lowest-energy glycine conformer, while the IV_{COOH}^{TS} saddle point is more similar to the Vn glycine conformer. Based on the position of the amino group, it can be anticipated that II_{COOH}^{TS} leads to the Ip_{COO} product isomer. Product-channel complexes for COOH abstraction are not identified due to significant UHF convergence issues in this region.

      Figure 22 depicts the schematic potential energy surface of the OH + glycine H-abstraction reaction showcasing the lowest-energy conformers along with the benchmark classical and adiabatic relative energies. It can be concluded that no matter which functional group undergoes H abstraction in glycine, the reaction is exothermic in all three scenarios. However, the extent of the exothermicity varies significantly among the cases: the CH_2-H-abstraction is nearly 2.3 times more exothermic than the NH_2-H-abstraction and approximately 7.4 times more exothermic than the COOH-H-abstraction. When considering only the classical energies, the COOH-dehydrogenation pathway shows a minor barrier of 1.02 kcal/mol. However, after accounting for zero-point energies, the transition states for all reaction channels are found to be lower in energy than the reactants. The NH_2-H-abstraction has the lowest classical(adiabatic) energy barrier, which is −1.91(−2.48) kcal/mol. This is followed by the CH_2-H-abstraction with an energy barrier of −0.37(−0.95) kcal/mol. The COOH-H-abstraction transition state has the highest energy compared to the

reactants. The energy difference is significant for the post-reaction complexes as well, just as it is for the products.
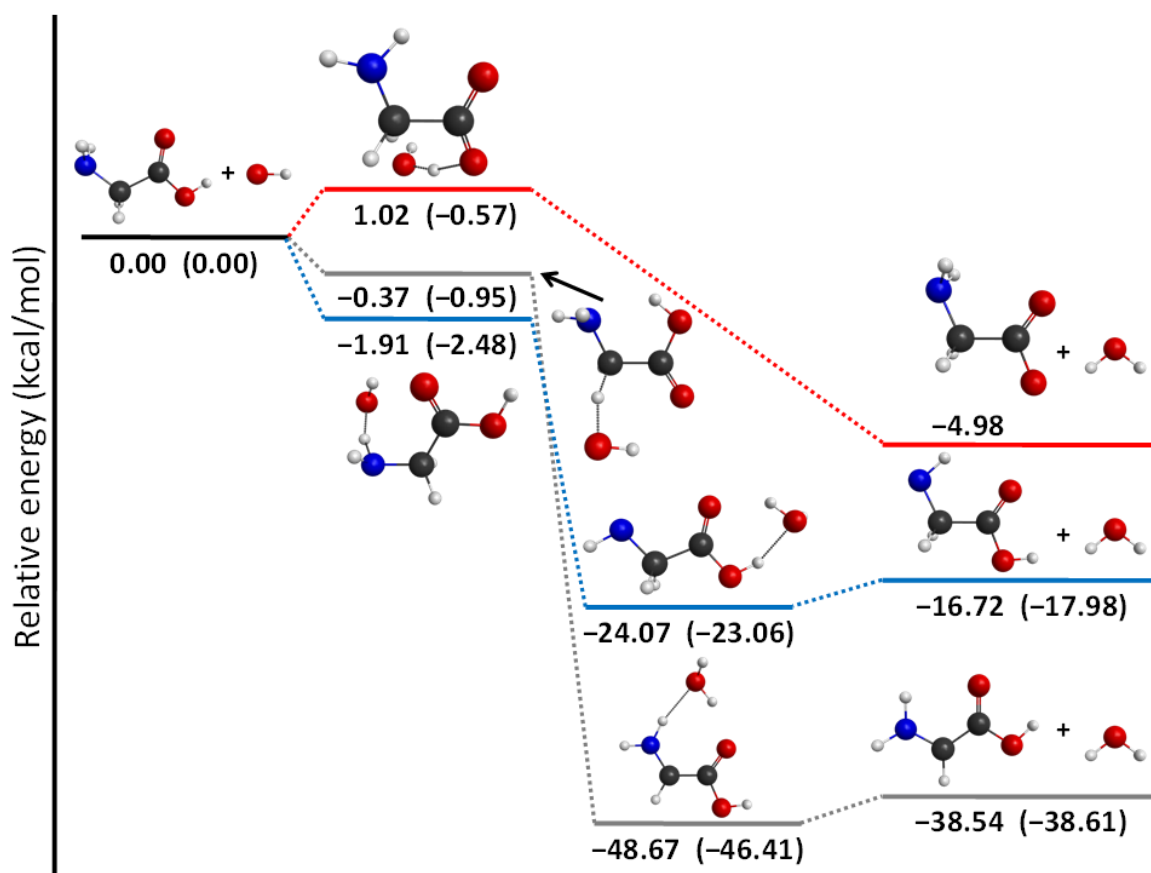

Figure 22. The energetics of the OH + glycine abstraction reaction highlighting the most accurate classical(adiabatic) relative energies of the lowest-energy conformers at the stationary points along the various reaction channels. Taken from Ref. [3].

Specifically, the CH_2-H-abstraction post-reaction complex has a classical(adiabatic) energy that is 24.60(23.55) kcal/mol lower than that of the NH_2-H-abstraction post-reaction complex. The global minimum of the potential energy surface for the OH + glycine H-abstraction reaction is provided by the CH_2-H-abstraction post-reaction complex, which has a classical(adiabatic) relative energy of −48.67(−46.61) kcal/mol. It can also be observed that the energy order of the CH_2- and NH_2-H-abstraction transition states and post-reaction complexes is reversed during the reaction. While the NH_2-H-abstraction reaction channel provides the lowest-energy barrier for the transition states, the CH_2-H-abstraction post-reaction complex has the lower energy. Under thermodynamic control, CH_2-abstraction is markedly preferred, while the different reaction pathways show no clear kinetic advantage.

The entrance channel is examined separately due to the spin-orbit effect. In this study, we provide one-dimensional potential energy curves obtained from MRCI/3-21G, MRCI/aug-cc-pVDZ and MRCI/aug-cc-pVTZ computations at seven different reactant orientations as illustrated in **Figure 23**. The orientations investigated can essentially be categorized into two groups, depending on whether the OH radical approaches the glycine molecule with its hydrogen end or its oxygen end. All of the one-dimensional potential curves exhibit a minimum with the exception of two orientations: those where the oxygen end of the OH radical approaches either the oxygen atom of the carbonyl group or the nitrogen atom in the glycine molecule. This behavior can be explained by the repulsion between the non-bonding electrons of the oxygen and nitrogen atoms. In five scenarios: (1) when the oxygen of the OH radical approaches the CH_2 group, (2) when the hydrogen side of the OH radical nears the nitrogen atom of the glycine molecule, (3) when the oxygen side of the OH radical comes close to the H at the NH_2 group of glycine, (4) when the oxygen side of the OH radical is near the carboxyl-OH and (5) when the hydrogen side of the OH radical is close to the carbonyl-O, the minima occur at H-bond distances of approximately 2–2.5 Å. When using the smaller 3-21G basis set with the MRCI method, the minima obtained are significantly deeper compared to those derived from the larger MRCI/aug-cc-pVDZ and MRCI/aug-cc-pVTZ computations. For orientations where the oxygen side of the OH radical approaches the CH, NH and COOH groups of the glycine molecule, the well depths are 1.0, 1.6, and 3.3 kcal/mol, respectively at the highest MRCI/aug-cc-pVTZ level of theory. In contrast, for orientations where the H-side of the OH radical approaches, the minima are significantly deeper with depths of 5.9 and 5.2 kcal/mol due to the formation of N···HO and carbonyl-O···HO hydrogen interactions. These deeper wells may cause the reactants to deviate from a reactive orientation giving the reaction an indirect character. The right side of **Figure 23** displays the potential curves for the two lowest spin-orbit (SO) and non-spin-orbit (non-SO) electronic states of the OH + glycine system in the entrance channel. The experimentally-observed spin-orbit effect of 0.2 kcal/mol is closely matched with the 0.18 kcal/mol effect calculated at the MRCI+Q/aug-cc-pVDZ level. This effect is apparent at large distances between the reactants but diminishes and disappears as the distance decreases and the SO_1 and non-SO_1 potentials converge to each other at shorter interfragment distances. Given the small size of the spin-orbit splitting, its impact on the entrance-channel properties discussed is minimal. The detailed numerical results for the

73

saddle points and minima are provided in **Table 7**, while **Table 8** contains the results for the product channels.
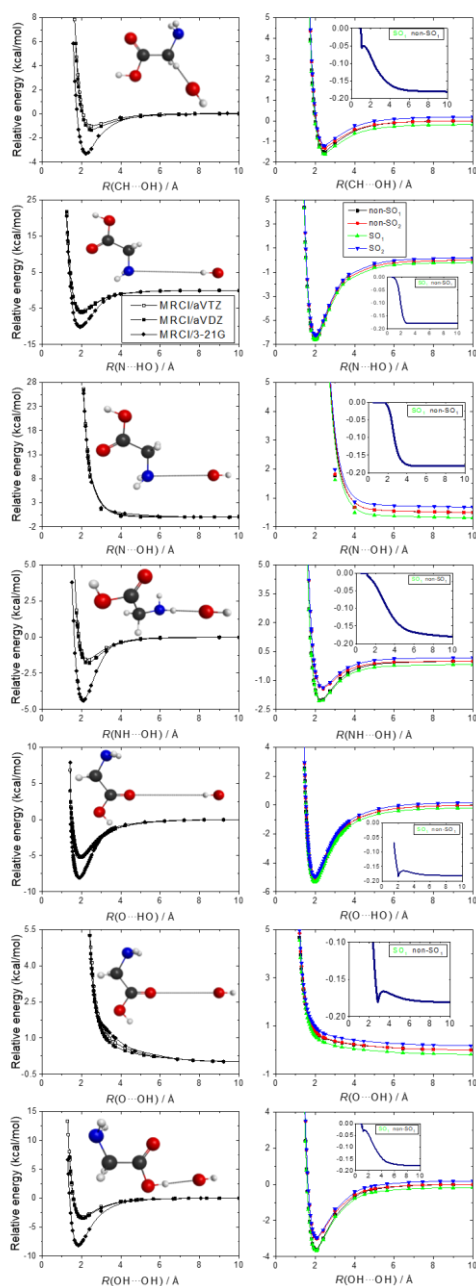

Figure 23. One-dimensional potential energy curves for the entrance-channel of the OH + glycine system obtained by MRCI/3-21G, MRCI/aug-cc-pVDZ and MRCI/aug-cc-pVTZ computations with the glycine and OH geometries fixed at their equilibrium structures. The terms SO_1 and SO_2 represent the spin-orbit ground and excited states, respectively, while non-SO_1 and non-SO_2 correspond to the non-relativistic ground and excited states determined at the MRCI+Q/aug-cc-pVDZ level of theory. The insets illustrate the spin-orbit corrections as a function of distance, shown as the energy differences between SO_1 and non-SO_1 states. Adapted from Ref. [3].

Table 7. The energies (in kcal/mol) and additional corrections (in kcal/mol) for the saddle points and minima of the OH + glycine (Ip) H-abstraction reaction at various levels of theory. The table is adapted from Ref. [3].

Stationary point	MP2 DZ^a	CCSD(T)–F12b DZ^b	TZ^c	QZ^d	$\delta[T]^e$	$\delta[(Q)]^f$	Δ_{core}^g	Δ_{rel}^h	Δ_{SO}^i	Classical^j	Δ_{ZPE}^k	Adiabatic^l
I_{CH}^{TS}	3.00	−0.66	−0.40	−0.27	−0.12	−0.18	−0.02	0.03	0.19	−0.37	−0.58	−0.95
II_{CH}^{TS}	3.34	−0.19	–	–	–	–	–	–	0.19	0.00^m	−0.09	−0.09
III_{CH}^{TS}	4.88	1.29	1.50	1.62	−0.13	−0.11	−0.04	0.03	0.19	1.56	−0.66	0.90
IV_{CH}^{TS}	6.00	2.45	2.67	2.77	−0.12	−0.15	−0.03	−0.21	0.19	2.45	−1.09	1.36
V_{CH}^{TS}	5.82	2.61	2.87	2.98	−0.11	−0.13	−0.01	0.03	0.19	2.95	−0.85	2.10
I_{CH}^{MIN}	−49.53	−48.19	−48.20	−48.26	−0.14	−0.21	−0.45	0.20	0.19	−48.67	2.26	−46.41
II_{CH}^{MIN}	−44.05	−43.05	−43.07	−43.11	−0.23	−0.21	−0.43	0.20	0.19	−43.59	1.99	−41.60
I_{NH}^{TS}	3.06	−1.71	–	–	−0.14	−0.25	–	–	0.19	$−1.91^n$	−0.57	−2.48
II_{NH}^{TS}	6.30	1.37	–	–	–	–	–	–	0.19	1.56^m	−1.17	0.39
III_{NH}^{TS}	7.90	3.11	–	–	−0.18	−0.25	–	–	0.19	2.87^n	−0.97	1.90
IV_{NH}^{TS}	11.71	6.77	–	–	–	–	–	–	0.19	6.96^m	−1.23	5.73
V_{NH}^{TS}	13.74	8.56	–	–	–	–	–	–	0.19	8.75^m	−1.23	7.52
I_{NH}^{MIN}	−24.92	−24.50	−24.25	−24.16	−0.07	−0.10	0.00	0.07	0.19	−24.07	1.01	−23.06
II_{NH}^{MIN}	−24.66	−24.24	−24.01	−23.89	−0.06	−0.10	−0.01	0.07	0.19	−23.80	1.13	−22.67
III_{NH}^{MIN}	−24.54	−24.08	−24.93	−23.84	−0.11	−0.11	−0.05	0.07	0.19	−23.85	1.53	−22.32
IV_{NH}^{MIN}	−23.90	−23.28	−23.11	−23.05	−0.07	−0.11	−0.03	0.06	0.19	−23.01	0.54	−22.47
V_{NH}^{MIN}	−22.82	−22.86	−22.57	−22.41	−0.18	−0.17	0.00	0.07	0.19	−22.50	1.76	−20.74
VI_{NH}^{MIN}	−22.85	−22.56	−22.28	−22.14	−0.14	−0.13	−0.04	0.08	0.19	−22.18	1.10	−21.08
VII_{NH}^{MIN}	−23.00	−22.54	−22.32	−22.22	−0.07	−0.09	0.01	0.06	0.19	−22.12	0.78	−21.34
$VIII_{NH}^{MIN}$	−22.05	−22.17	−21.91	−21.75	−0.19	−0.17	0.00	0.08	0.19	−21.84	1.64	−20.20
IX_{NH}^{MIN}	−22.24	−21.88	−21.62	−21.49	−0.13	−0.12	−0.04	0.08	0.19	−21.51	0.83	−20.68
X_{NH}^{MIN}	−21.82	−21.14	−20.82	−20.70	−0.11	−0.11	−0.02	0.06	0.19	−20.69	0.27	−20.42
XI_{NH}^{MIN}	−21.70	−21.00	−20.81	−20.74	−0.09	−0.12	−0.01	0.06	0.19	−20.71	0.60	−20.11
XII_{NH}^{MIN}	−21.38	−20.78	−20.53	−20.45	−0.08	−0.10	0.00	0.05	0.19	−20.39	0.44	−19.95
$XIII_{NH}^{MIN}$	−20.98	−20.12	−19.82	−19.72	−0.07	−0.10	0.03	0.05	0.19	−19.62	0.38	−19.24
XIV_{NH}^{MIN}	−20.31	−19.65	−19.39	−19.30	−0.08	−0.11	0.00	0.05	0.19	−19.25	0.48	−18.77
XV_{NH}^{MIN}	−19.56	−19.09	−18.87	−18.77	−0.10	−0.15	0.06	0.04	0.19	−18.73	1.00	−17.73
XVI_{NH}^{MIN}	−19.81	−18.98	−18.64	−18.52	−0.07	−0.11	0.03	0.05	0.19	−18.43	0.12	−18.31
$XVII_{NH}^{MIN}$	−19.31	−18.74	−18.54	−18.47	−0.11	−0.11	−0.01	0.06	0.19	−18.45	0.51	−17.94
$XVIII_{NH}^{MIN}$	−15.63	−14.83	−14.46	−14.32	−0.13	−0.10	0.04	0.05	0.19	−14.27	0.27	−14.00
XIX_{NH}^{MIN}	−15.27	−14.77	−14.51	−14.42	−0.12	−0.10	0.02	0.05	0.19	−14.38	0.49	−13.89
I_{COOH}^{TS}	−2.72	1.51	1.52	1.61	−0.13	−0.56	−0.21	0.12	0.19	1.02	−1.59	−0.57
II_{COOH}^{TS}	7.77	1.57	1.48	1.62	–	–	0.04	−0.01	0.19	1.84^o	−0.10	1.74
III_{COOH}^{TS}	−2.29	2.07	2.09	2.19	−0.14	−0.57	−0.20	0.12	0.19	1.59	−1.67	−0.08
IV_{COOH}^{TS}	8.91	2.62	2.53	2.70	−0.35	−0.56	0.04	−0.01	0.19	2.01	0.09	2.10
V_{COOH}^{TS}	9.23	2.96	2.86	3.03	–	–	0.04	−0.01	0.19	3.25^o	0.00	3.25

[a] MP2/aug-cc-pVDZ relative energies computed at MP2/aug-cc-pVDZ geometries.

[b] CCSD(T)-F12b/aug-cc-pVDZ relative energies computed at CCSD(T)-F12b/aug-cc-pVDZ geometries.

[c] CCSD(T)-F12b/aug-cc-pVTZ relative energies computed at CCSD(T)-F12b/aug-cc-pVDZ geometries.

[d] CCSD(T)-F12b/aug-cc-pVQZ relative energies computed at CCSD(T)-F12b/aug-cc-pVDZ geometries.

[e] Eq. (98). [f] Eq. (99). [g] Eq. (100). [h] Eq. (101). [i] Eq. (102). [j] Eq. (103).

[k] ZPE correction determined at the CCSD(T)-F12b/aug-cc-pVDZ level of theory.

[l] Eq. (104).

m The benchmark classical relative energy is determined as CCSD(T)-F12b/aug-cc-pVDZ + Δ_{SO}, due to convergence issues with the other energy computations.

n The benchmark classical relative energy is determined as CCSD(T)-F12b/aug-cc-pVDZ + $\delta[T]$ + $\delta[(Q)]$ + Δ_{SO}, due to convergence issues with the other energy computations.

o The benchmark classical relative energy is determined as CCSD(T)-F12b/aug-cc-pVDZ + Δ_{core} + Δ_{rel} + Δ_{SO}, due to convergence issues with the other energy computations.

Table 8. The energies (in kcal/mol) and additional corrections (in kcal/mol) for the products of the OH + glycine (Ip) H-abstraction reaction at various levels of theory. The table is adapted from Ref. [3].

Stationary point	MP2 DZ^a	CCSD(T)—F12b DZ^b	TZ^c	QZ^d	$\delta[T]$^e	$\delta[(Q)]$^f	Δ_{core}^g	Δ_{rel}^h	Δ_{SO}^i	Classical^j	Δ_{ZPE}^k	Adiabatic^l
$H_2O + I_n^{CH}$	−38.35	−37.75	−37.90	−38.11	−0.21	−0.20	−0.39	0.18	0.19	−38.54	−0.07	−38.61
$H_2O + II_n^{CH}$	−36.04	−36.23	−36.33	−36.54	−0.26	−0.21	−0.38	0.18	0.19	−37.02	−0.09	−37.11
$H_2O + III_n^{CH}$	−32.56	−32.49	−32.64	−32.84	−0.31	−0.21	−0.37	0.17	0.19	−33.37	−0.29	−33.66
$H_2O + IV_n^{CH}$	−26.51	−27.98	−28.05	−28.20	−0.39	−0.22	−0.29	0.15	0.19	−28.76	−0.20	−28.96
$H_2O + I_p^{NH}$	−17.06	−16.74	−16.70	−16.75	−0.10	−0.12	0.02	0.04	0.19	−16.72	−1.26	−17.98
$H_2O + II_p^{NH}$	−16.25	−15.99	−15.92	−15.96	−0.23	−0.15	−0.01	0.05	0.19	−16.11	−0.98	−17.09
$H_2O + III_n^{NH}$	−15.28	−14.84	−14.77	−14.81	−0.08	−0.11	0.05	0.04	0.19	−14.72	−1.11	−15.83
$H_2O + IV_p^{NH}$	−14.07	−13.49	−13.35	−13.41	−0.11	−0.11	0.04	0.04	0.19	−13.36	−1.48	−14.84
$H_2O + V_p^{NH}$	−13.98	−13.44	−13.31	−13.35	−0.07	−0.10	0.05	0.04	0.19	−13.24	−1.36	−14.60
$H_2O + VI_p^{NH}$	−12.03	−11.77	−11.70	−11.74	−0.16	−0.13	0.04	0.04	0.19	−11.76	−1.46	−13.22
$H_2O + VII_p^{NH}$	−8.05	−7.58	−7.43	−7.47	−0.16	−0.11	0.07	0.03	0.19	−7.45	−1.66	−9.11
$H_2O + I_p^{COO}$	–	–	−4.80^m	−4.93^n	–	–	−0.22	−0.02	0.19	−4.98	–	–
$H_2O + II_p^{COO}$	–	–	–	–	−0.68	−0.65	–	–	0.19	–	–	–
$H_2O + III_p^{COO}$	–	–	–	–	–	–	–	0.02	0.19	–	–	–
$H_2O + IV_n^{COO}$	–	–	–	–	–	–	–	–	0.19	–	–	–

a MP2/aug-cc-pVDZ relative energies computed at MP2/aug-cc-pVDZ geometries.

b CCSD(T)-F12b/aug-cc-pVDZ relative energies computed at CCSD(T)-F12b/aug-cc-pVDZ geometries.

c CCSD(T)-F12b/aug-cc-pVTZ relative energies computed at CCSD(T)-F12b/aug-cc-pVDZ geometries.

d CCSD(T)-F12b/aug-cc-pVQZ relative energies computed at CCSD(T)-F12b/aug-cc-pVDZ geometries.

e Eq. (98). f Eq. (99). g Eq. (100). h Eq. (101). i Eq. (102). j Eq. (103).

k ZPE correction determined at the CCSD(T)-F12b/aug-cc-pVDZ level of theory.

l Eq. (104).

m MRCI/aug-cc-pVDZ geometries are employed for these product radicals, because energy computations fail to converge in many instances.

It is evident that MP2 computations yield significantly different energies compared to coupled-cluster theory, particularly for transition states. In certain instances, the MP2 method can result in energy values that are up to 5 kcal/mol higher than those obtained using the more accurate CCSD(T)-F12b method. For example, a difference of 6.19 and 6.27

kcal/mol is observed between the MP2/aug-cc-pVDZ and CCSD(T)-F12b/aug-cc-pVDZ energies for the IV_{CH}^{TS} and V_{CH}^{TS}, respectively. However, MP2 typically provides relative energies for the products with an accuracy of 0.5 − 1.0 kcal/mol. The energy differences among CCSD(T)-F12b calculations with different basis sets are typically less than 1.1 kcal/mol. The largest difference occurs between the CCSD(T)-F12b/aug-cc-pVTZ and CCSD(T)-F12b/aug-cc-pVQZ energies for III_{NH}^{MIN} with a value of 1.09 kcal/mol. The $\delta[T]$ and $\delta[(Q)]$ corrections are consistently negative and of comparable magnitude. In most cases, their combined effect results in a reduction of relative energy by 0.2–0.3 kcal/mol. For the COOH TSs, larger absolute corrections are observed: specifically, the $\delta[(Q)]$ corrections are −0.56 kcal/mol for I_{COOH}^{TS}, −0.57 kcal/mol for III_{COOH}^{TS}, and −0.56 kcal/mol for IV_{COOH}^{TS}. The core correlation and scalar relativistic corrections typically have effects measured in only a few hundredths or in some cases a few tenths of a kcal/mol. The most significant corrections are observed for the products of the CH abstraction channel and the associated product complexes. The spin-orbit correction is uniformly 0.19 kcal/mol across all stationary points, which aligns closely with the experimental value of 0.20 kcal/mol. To obtain experimentally-relevant energies, zero-point energy corrections need to be applied. Typically, these corrections are between 1 and 2 kcal/mol. Interestingly, all minima in the product channel show positive Δ_{ZPE} values, whereas both the products and saddle points exhibit negative ZPE corrections. When ZPE corrections are included, the energy ordering of some conformers may change in certain instances. It can be clearly stated that the I_{CH}^{MIN} conformer represents the global minimum of the potential energy surface.

3.2 THE DEVELOPMENT AND CHARACTERIZATION OF THE PESS

As mentioned earlier, to gain insight into the atomic-level mechanisms of reactions, it is essential to have a well-defined PES. In my research, global, full-dimensional analitycal *ab initio* PESs are constructed with the help of the ROBOSURFER program package for the OH + C_2H_6 and OH + glycine systems, which are discussed in the subsequent sections of the chapter.

3.2.1 OH + C₂H₆

3.2.1.1 Computational details

As the first step in potential energy surface development, an initial geometry set is generated during which the Cartesian coordinates of minima and transition states are randomly displaced by 0-0.32 Å and for reactants and products the individual fragments are randomly scattered around each other within distances of 3-10 Å, while their Cartesian coordinates are also randomly displaced by 0-0.20 Å. To compute the energies, a composite method is chosen, where a basis-set correction is added to the unrestricted explicitly-correlated coupled-cluster singles, doubles, and perturbative triples (UCCSD(T)-F12b) method applied with the aug-cc-pVDZ basis set. Regarding the basis set correction, we employ the restricted explicitly-correlated second-order Møller-Plesset (RMP2-F12) method in conjunction with aug-cc-pVDZ and aug-cc-pVTZ bases sets. Thus, the energy expression is formulated as follows:

$$E_{OH + C_2H_6} = \text{UCCSD(T)-F12b/aug-cc-pVDZ} + (\text{RMP2-F12/aug-cc-pVTZ} - \text{RMP2-F12/aug-cc-pVDZ}). \quad (105)$$

After the energy computations, the development is commenced with 2393 energy points on board. The energy points are fitted within the framework of the monomial symmetrization approach (MSA) of the permutationally invariant polynomial method, where we employ a full-dimensional analytic function of Morse-type variables ($y_{ij} = \exp(-r_{ij}/a)$) with the parameter a chosen to be 2 bohrs. In the early stages of the development due to the insufficient number of energy points for a fifth-order fit, the fitting process is initiated with a fourth-order fit. Once a dataset with adequate number of energy points was reached, we have transitioned to fitting with a fifth-order polynomial. The fourth-order expansion involves 715 coefficients, while the fifth-order expansion entails 3285 coefficients. The coefficients are calculated through a weighted linear least-squares fitting method applied to the ab initio data utilizing a weight-function of $E_0/(E + E_0)$, where E represents the potential energy relative to the minimum of the dataset and E_0 is fixed at 0.05 hartree (31.4 kcal/mol). New structures from QCT simulations are assimilated into the existing geometry set within a range of −30 to 150 kcal/mol relative to the reactants in order to enhance the potential. Simulations are run at $b = 0.0, 0.5, 1.0, 1.5$, and 2.0 bohr values with 5 trajectories executed for a specific impact parameter resulting

in a total of 25 QCT calculations performed in one iteration. The initial collision energy for the development is set to $E_{coll} = 10$ kcal/mol. Upon reaching the desired quality of the PES, which can be achieved by reducing the occurrence of invalid trajectories below 1-3%, the collision energy is systematically increased by increments of 10 kcal/mol until it reaches $E_{coll} = 60$ kcal/mol. From the 1946th iteration onwards, the development proceeds from the direction of the H_2O + C_2H_5 product channel with a collision energy of $E_{coll} = 30$ kcal/mol with the aim of enhancing the quality of the PES even further. In this reverse direction, a total of 18 iterations are executed involving the addition of 458 energy points. The development is completed by the 1964th iteration resulting in a final PES consisting of 12544 energy points.

3.2.1.2 Results

Table 9 provides a summary of the fitting quality across different energy ranges presenting the root-mean-square (RMS) values and the corresponding number of energy points within each range.

Table 9. The fitting errors (kcal/mol) and the number of energy points for each energy range (kcal/mol) for the final PES of the OH + C_2H_6 system.

Energy range (kcal/mol)	Fitting error (kcal/mol)	Number of energy points
0.00 - 31.38	0.63	4895
31.38 - 62.75	0.87	5467
62.75 - 156.88	1.09	2142
156.88 <	0.76	40

It can be stated that in chemically-relevant energy ranges (0.00 - 62.75 kcal/mol) the RMS values are below 1 kcal/mol, which is considered as chemical accuracy. Additionally, in the range of 62.76 - 156.88 kcal/mol, the fitting error barely exceeds 1 kcal/mol. The low RMS in the energy range above 156.88 kcal/mol is due to the fact that this range contains only 40 points.

The quality of the PES can be characterized by the number of invalid trajectories generated during dynamics simulations, which is further detailed in **Figure 24**.
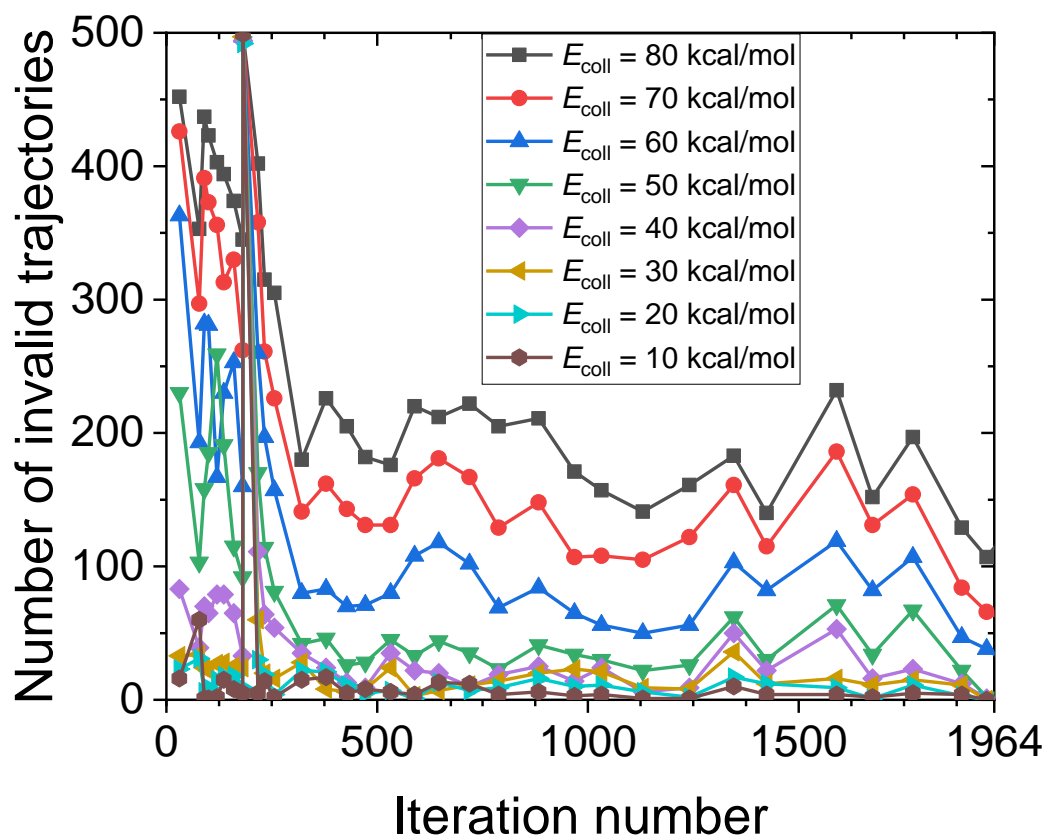
Figure 24. The fluctuation in the number of invalid trajectories from 500 during the PES development of the OH + C_2H_6 system across iterations.

To test the quality of the PES at a given moment, we run 500 trajectories at each of the collision energies 10, 20, 30, 40, 50, 60, 70, and 80 kcal/mol. The development proceeds with a collision energy of 10 kcal/mol in fourth order and at this point the number of invalid trajectories is high. Reaching the 90th iteration, the collision energy is increased by 10 kcal/mol, as at this point, the number of invalid trajectories has decreased at the previous (10 kcal/mol) collision energy. Here we can observe that as the development starts at a collision energy of 20 kcal/mol, the number of invalid trajectories spikes at every test collision energy, then steadily decreases until the 218th iteration, where the number of invalid trajectories suddenly increases significantly. This can be explained by the switch from the fourth to the fifth order at this point. As the order increases, the fitted analytical function becomes much more flexible, which greatly contributes to further improving the quality of the PES. Subsequently, at the 257th iteration, the collision energy is set to 30

kcal/mol followed by increases to 40 kcal/mol at the 590th iteration, to 50 kcal/mol at the 1425th iteration, and to 60 kcal/mol at the 1888th iteration. It can be observed that each increment in collision energy typically results in a slight increase in the number of invalid trajectories. Moreover, it is noticeable that increasing the collision energy from 40 to 50 kcal/mol requires more iterations, which can be explained by the fact that substitution reactions open up at this point. The development of the PES concludes with the 1964th iteration, where we can observe that the potential is suitable for studying the OH + C_2H_6 reaction as the number of invalid trajectories remains negligible up to 50 kcal/mol collision energy. Searching for the stationary points on the final PES and comparing their energies with the previously-determined benchmark results also demonstrates the quality of the PES.

Figure 25 illustrates the comparison between the previously-determined relative benchmark energies and the relative energies calculated using the PES.
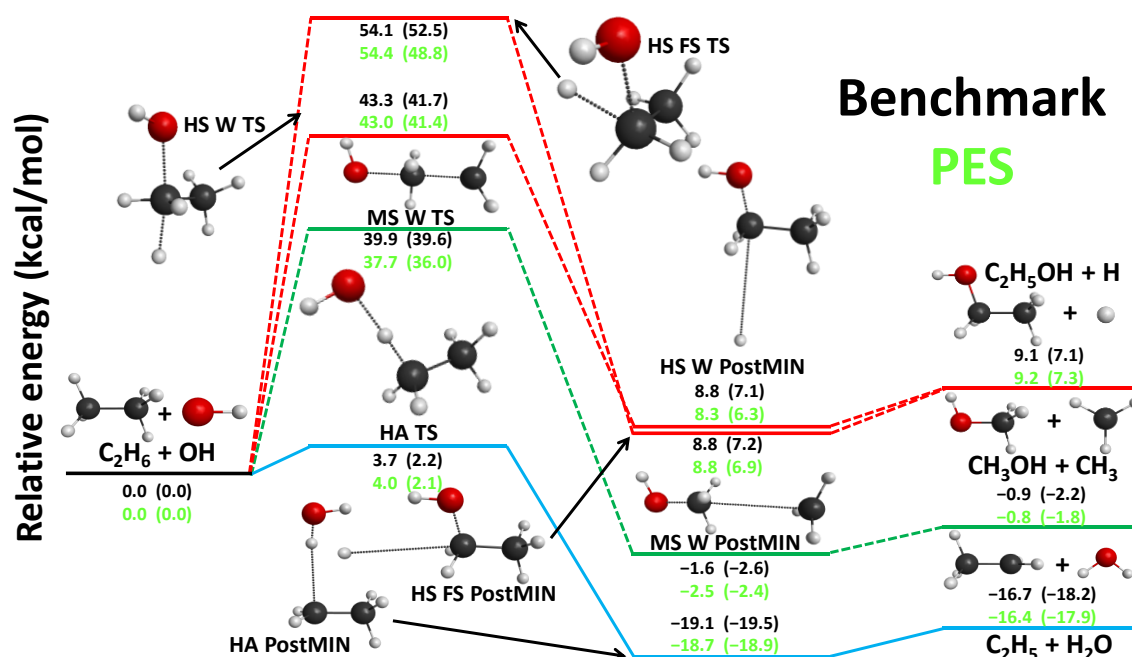
Figure 25. Graphical representation of the schematic potential energy landscape for the OH + C_2H_6 reaction depicting in black the previously-determined benchmark classical(adiabatic) energies and in green the classical(adiabatic) relative energies calculated using the PES. Adapted from Ref. [2].

It can be seen that the benchmark results and the energies calculated on the PES show very good agreement and considering the H-abstraction reaction pathway these differences are

0.6 kcal/mol or less for both classical and adiabatic energies. These small differences indicate the high quality of the developed potential. Furthermore, it is observable for the stationary points of the Walden-inversion H-substitution reaction that the energy differences are extremely small, only in the case of the product-channel minimum experiencing a larger difference of 0.8 kcal/mol between the benchmark and the adiabatic energies calculated on the PES.

3.2.2   OH + glycine

3.2.2.1   Computational details

The first step in potential development involves generating an initial set of geometries. This process entails randomly displacing the Cartesian coordinates of minima and transition states by 0-0.32 Å. For reactants and products, the fragments are randomly scattered around each other at distances of 3-10 Å with their Cartesian coordinates also being randomly displaced by 0-0.20 Å. During the development, all previously-mapped stationary points were used to create the initial geometry set. Specifically, we consider 8 conformer structures for the reactants, 5 conformer structures for CH transition states, 5 conformer structures for NH transition states, 5 conformer structures for COOH transition states, 2 conformer structures for CH minima, 19 conformer structures for NH minima, 4 product conformer structures for H-abstraction at the CH_2 group, 7 product conformer structures for H-abstraction at the NH_2 group, and 4 product conformer structures for H-abstraction at the COOH group. To compute the energies, a composite method is selected, which involves adding a basis-set correction to the unrestricted explicitly-correlated coupled-cluster singles, doubles, and perturbative triples (UCCSD(T)-F12a) method used with the cc-pVDZ basis set. For the basis-set correction, we employ the restricted explicitly-correlated second-order Møller-Plesset (RMP2-F12) method using cc-pVDZ-F12 and cc-pVTZ-F12 basis sets. Consequently, the energy expression is given as follows:

$$E_{\text{OH+ Gly}} = \text{UCCSD(T)-F12a/cc-pVDZ} + (\text{RMP2-F12/cc-pVTZ-F12} - \text{RMP2-F12/cc-pVDZ-F12}). \qquad (106)$$

After the energy computations, the development begins with a total of 5693 energy points. These points are fitted using the monomial symmetrization approach (MSA) of the permutationally invariant polynomial method. In this process, a Morse-type variable ($y_{ij} = \exp(-r_{ij}/a)$) is used with the parameter a set to 2 bohrs. The order of the fitting was 4,

82

which corresponds to 4466 coefficients. The coefficients are determined using a weighted linear least-squares fitting method applied to the *ab initio* data with a weight function of $E_0/(E + E_0)$, where E is the potential energy relative to the minimum of the dataset and E_0 is a fixed value. Until the 141st iteration, the development used $E_0 = 0.05$ hartree (31.4 kcal/mol). However, due to the exothermic nature of the reaction, the value of this parameter was increased to 0.15 hartree (94.1 kcal/mol) starting from the 142nd iteration. New structures obtained from QCT simulations are integrated into the current geometry set within a range of −60 to 1000 kcal/mol relative to the reactants to improve the potential. Simulations are carried out at b values ranging from 0.0 to 5.1 bohr with increments of 0.3 bohr and involve running 5 trajectories for each specific impact parameter. This results in 90 QCT calculations performed in each iteration. Each iteration employs a different glycine conformer for the QCT simulations. The development begins with an initial collision energy of $E_{coll} = 1$ kcal/mol. Once the PES reaches the desired accuracy indicated by having less than 1-3% invalid (unphysical) trajectories, the collision energy is increased. During the development, the following collision energies are applied after the initial 1 kcal/mol: 10, 20, and 30 kcal/mol. The development concludes after the 181st iteration resulting in a final potential energy surface with 13 663 energy points.

3.2.2.2   Results

Table 10 summarizes the fitting quality across various energy ranges, presenting the root-mean-square (RMS) values along with the number of energy points within each range.

Table 10. The fitting errors (kcal/mol) and the number of energy points for each energy range (kcal/mol) for the final PES of the OH + glycine system.

Energy range (kcal/mol)	Fitting error (kcal/mol)	Number of energy points
0.0 - 94.1	2.82	8306
94.1 – 188.3	5.34	2681
188.3 – 470.3	8.19	2236
470.3 <	18.70	443

For the H-abstraction reaction, the most relevant energy region is between 0.0 and 94.1 kcal/mol, where the fitting error is 2.82 kcal/mol. This nearly 3 kcal/mol inaccuracy can be attributed to the complexity of the reaction as the OH + glycine system consists of 12 atoms resulting in $3 \times 12 - 6 = 30$ degrees of freedom making the potential energy surface 30-dimensional. It is also worth noting that the fitting error could be reduced by increasing the order of the fitting, but the current number of energy points does not allow for a fifth-order fitting.

The quality of the PES is reflected in the number of invalid trajectories produced during dynamics simulations, just like in case of the OH + C_2H_6 reaction, as further illustrated in **Figure 26**.
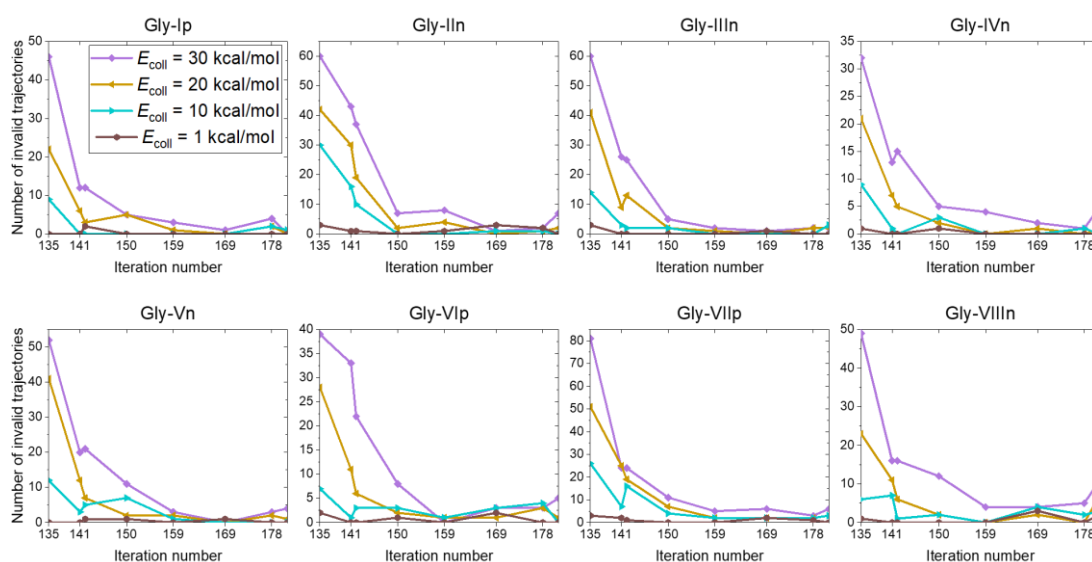
Figure 26. The fluctuation in the number of invalid trajectories from 300 during the PES development of the OH + glycine system across iterations for each reactant conformer.

To check the quality of the PES throughout the process, we run 300 trajectories at collision energies of 1, 10, 20 and 30 kcal/mol for each reactant conformer. This testing process begins from the 135th iteration. It can be seen that at the 135th and 141st iterations, the number of invalid trajectories is still high regardless of which glycine conformer collides with the OH radical during the QCT simulation. It can be observed that from the 141st to the 142nd iteration, the number of invalid trajectories does not change significantly indicating that altering the E_0 fitting parameter does not have a substantial impact on this

count. Furthermore, starting the test simulations with the glycine conformer IIn shows that the number of invalid trajectories continues to decrease at collision energies of 10, 20 and 30 kcal/mol. At a collision energy of 1 kcal/mol, the already low value (1) remains unchanged. Tests conducted at the 150th iteration reveal that the quality of the PES has significantly improved at this stage with the most notable improvement seen for simulations starting with the glycine conformer VIIp. In this case, the number of invalid trajectories decreases from 1 to 0 at a collision energy of 1 kcal/mol, from 16 to 4 at 10 kcal/mol, from 19 to 7 at 20 kcal/mol and from 24 to 11 at 30 kcal/mol. Subsequently, the number of invalid trajectories changes only slightly and by the final iteration, the number of invalid trajectories remains below 3% for each glycine conformer with the exception of the conformer VIIIn, where the value is 11, which corresponds to 3.67%.

Table 11 and **Table 12** compare the previously-determined relative benchmark energies with those calculated using the PES. For the CH TSs, the largest difference between the previously-determined benchmark and PES-calculated energy values is observed for II_{CH}^{TS} with a value of 0.79 kcal/mol. The differences in adiabatic energies are generally more significant. The largest discrepancy, which is 1.8 kcal/mol, appears for II_{CH}^{TS}. Looking at the energies of the CH MINs, we find that the differences between the benchmark and PES energies are consistently below 1.0 kcal/mol. In fact, for adiabatic energies, these differences are less than 0.30 kcal/mol for both CH MIN cases. Furthermore, the energy order of the individual conformers remains unchanged for the stationary points in the case of H-abstraction on the CH_2 group of the glycine molecule. For the amino-region stationary points, the smallest classical energy difference between the benchmark and PES-calculated values is 0.14 kcal/mol for V_{NH}^{TS}, while the largest difference is 0.99 kcal/mol for III_{NH}^{TS}. In the adiabatic case, the differences are somewhat larger exceeding 1.0 kcal/mol in three instances (I_{NH}^{TS}, IV_{NH}^{TS}, V_{NH}^{TS}). For the NH MINs, relatively larger differences are observed in both classical and adiabatic cases. In fact, the second-lowest energy NH MIN shows one of the largest differences when considering all stationary points. For the stationary points in the amino region, it can be concluded that the energy order remains consistent for transition states, but the energy order of the post-reaction minima shows significant changes compared to the earlier benchmark order when considering the PES-calculated values.

Table 11. Comparison of the benchmark classical and adiabatic relative energies of the transition states and post-reaction minima with the values obtained using the PES (all data are given in kcal/mol).

Stationary point	Classical		Adiabatic	
	Benchmark	PES	Benchmark	PES
I_{CH}^{TS}	−0.37	−0.92	−0.95	0.66
II_{CH}^{TS}	0.00	0.79	−0.09	1.71
III_{CH}^{TS}	1.56	1.10	0.90	1.53
IV_{CH}^{TS}	2.45	2.20	1.36	2.58
V_{CH}^{TS}	2.95	3.60	2.10	3.87
I_{CH}^{MIN}	−48.67	−49.93	−46.41	−46.63
II_{CH}^{MIN}	−43.59	−44.36	−41.60	−41.90
I_{NH}^{TS}	−1.91	−1.39	−2.48	−0.80
II_{NH}^{TS}	1.56	0.65	0.39	0.90
III_{NH}^{TS}	2.87	1.88	1.90	2.89
IV_{NH}^{TS}	6.96	6.14	5.73	6.78
V_{NH}^{TS}	8.75	8.61	7.52	9.70
I_{NH}^{MIN}	−24.07	−25.74	−23.06	−24.73
II_{NH}^{MIN}	−23.8	−28.91	−22.67	−29.13
III_{NH}^{MIN}	−23.85	−25.53	−22.32	−23.92
IV_{NH}^{MIN}	−23.01	−24.96	−22.47	−23.55
V_{NH}^{MIN}	−22.50	−24.54	−20.74	−21.49
VI_{NH}^{MIN}	−22.18	−24.01	−21.08	−22.15
VII_{NH}^{MIN}	−22.12	−23.89	−21.34	−22.91
$VIII_{NH}^{MIN}$	−21.84	−24.52	−20.20	−21.37
IX_{NH}^{MIN}	−21.51	−23.21	−20.68	−21.59
X_{NH}^{MIN}	−20.69	−21.94	−20.42	−20.46
XI_{NH}^{MIN}	−20.71	−23.66	−20.11	−22.04
XII_{NH}^{MIN}	−20.39	−21.77	−19.95	−20.59
$XIII_{NH}^{MIN}$	−19.62	−23.34	−19.24	−21.43
XIV_{NH}^{MIN}	−19.25	−21.10	−18.77	−20.19
XV_{NH}^{MIN}	−18.73	−21.47	−17.73	−19.75
XVI_{NH}^{MIN}	−18.43	−20.81	−18.31	−19.71
$XVII_{NH}^{MIN}$	−18.45	−20.35	−17.94	−18.86
$XVIII_{NH}^{MIN}$	−14.27	−16.58	−14.00	−14.48
XIX_{NH}^{MIN}	−14.38	−16.61	−13.89	−15.32
I_{COOH}^{TS}	1.02	0.90	−0.57	−1.56
II_{COOH}^{TS}	1.84	−2.80	1.74	−1.52
III_{COOH}^{TS}	1.59	0.33	−0.08	−1.99
IV_{COOH}^{TS}	2.01	−1.63	2.10	−1.24
V_{COOH}^{TS}	3.25	−3.68	3.25	−2.69

In the carboxyl region, the transition states show that both classically and adiabatically, the largest energy difference is observed for V_{COOH}^{TS}. The PES-calculated energy values for this conformer are significantly more negative compared to the benchmark values. Consequently, this indicates that V_{COOH}^{TS}, which is identified as the highest-energy COOH TS in the benchmark study, is not only the lowest-energy COOH TS but also the lowest-energy transition state when considering all three reaction channels (CH, NH, COOH) across the entire PES.

Table 12. Comparison of the benchmark classical and adiabatic relative energies of the products with the values obtained using the PES (all data are given in kcal/mol).

Stationary point	Classical		Adiabatic	
	Benchmark	PES	Benchmark	PES
$H_2O + I_n^{CH}$	−38.54	−39.13	−38.61	−37.87
$H_2O + II_n^{CH}$	−37.02	−39.35	−37.11	−37.75
$H_2O + III_n^{CH}$	−33.37	−36.29	−33.66	−35.39
$H_2O + IV_n^{CH}$	−28.76	−37.49	−28.96	−35.85
$H_2O + I_p^{NH}$	−16.72	−18.00	−17.98	−18.30
$H_2O + II_p^{NH}$	−16.11	−16.51	−17.09	−16.66
$H_2O + III_n^{NH}$	−14.72	−16.39	−15.83	−16.62
$H_2O + IV_p^{NH}$	−13.36	−15.01	−14.84	−15.55
$H_2O + V_p^{NH}$	−13.24	−15.10	−14.60	−15.19
$H_2O + VI_p^{NH}$	−11.76	−14.25	−13.22	−14.97
$H_2O + VII_p^{NH}$	−7.45	−9.47	−9.11	−10.50
$H_2O + I_p^{COO}$	−4.98	−11.06	–	−12.45
$H_2O + II_n^{COO}$	–	−4.51	–	−6.33
$H_2O + III_p^{COO}$	–	−11.27	–	−12.69
$H_2O + IV_n^{COO}$	–	−9.84	–	−9.64

Comparing the benchmark energies of the product conformers corresponding to the H-abstraction reaction at the CH_2 group of the glycine molecule with the values determined using the PES, it is evident that for the first three conformers the difference between the two sets of values falls within the fitting error of 2.82 kcal/mol. However, for IV_n^{CH}, the energy calculated with the PES is approximately 7 kcal/mol lower in both classical and adiabatic cases. For the products formed during the H-abstraction at the amino group of the glycine molecule, the best agreement between the benchmark and PES-calculated energy values in both classical and adiabatic cases is observed for the I_p^{NH} product conformer. For the other conformers, while the differences are larger, they still remain

within the fitting error range. For the H-abstraction at the carboxyl group only the first conformer allows for a comparison between the benchmark and PES-calculated classical energy values, where an approximate difference of 6 kcal/mol is observed. Note that the benchmark energy for the carboxyl-dehydrogenated glycine conformers might be less accurate than the value determined using the PES. The possible inaccuracy arises from the benchmark geometry being determined only at the MRCI/aug-cc-pVDZ level, and the post-CCSD(T) correction calculations failing to converge, thereby excluding them from the benchmark energy.

3.3 REACTION DYNAMICS

Following the development of the PES, it becomes possible to study the atomic-level mechanisms of reactions, which I have done for the OH + C_2H_6 and OH + glycine systems during my research. This chapter first presents the computational background of the quasi-classical trajectory computations followed by the conclusions drawn from the simulations in each section. I would note that for the OH + C_2H_6 reaction, we examine the dynamics in two ways: first, with the reactants in their vibrational ground state ($v = 0$), and second, by exciting a selected vibrational mode by one quantum in the OH/C_2H_6 molecule ($v = 1$).

3.3.1 OH + C_2H_6 ($v = 0$)

3.3.1.1 Computational details

For the OH + C_2H_6 system in the vibrational ground state, we investigate the dynamics of the reaction at five different collision energies: 10, 20, 30, 40, and 50 kcal/mol. The vibrational ground state of the reactants is ensured by normal mode sampling and their rotational angular momentum is set to zero. The orientations of the reactants are randomly rotated. The initial distance between the center of masses of the reactants is given by $\sqrt{x^2 + b^2}$, where x = 18.90 bohrs (10 Å) and the impact parameter b is adjusted in increments of 0.5 bohr ranging from 0 to 8 bohrs. At each combination of collision energy and impact parameter, we conduct 1000 trajectories resulting in a total of 85 000 simulations. Trajectories are run with a time step of 0.0726 fs and cease when the maximum interatomic distance surpasses the largest initial distance by one bohr.

3.3.1.2   Results

The results presented hereinafter pertain solely to the H-abstraction reaction, as QCT simulations indicate that H- and methyl-substitution products are produced only in very small quantities as their integral cross sections are 0.03 and 0.02 bohr^2 at 50 kcal/mol collision energy, respectively. Therefore, extrapolating significant results from the limited number of trajectories may lead to erroneous conclusions.

Figure 27 illustrates how the integral cross section for the H-abstraction channel changes with increasing collision energy.
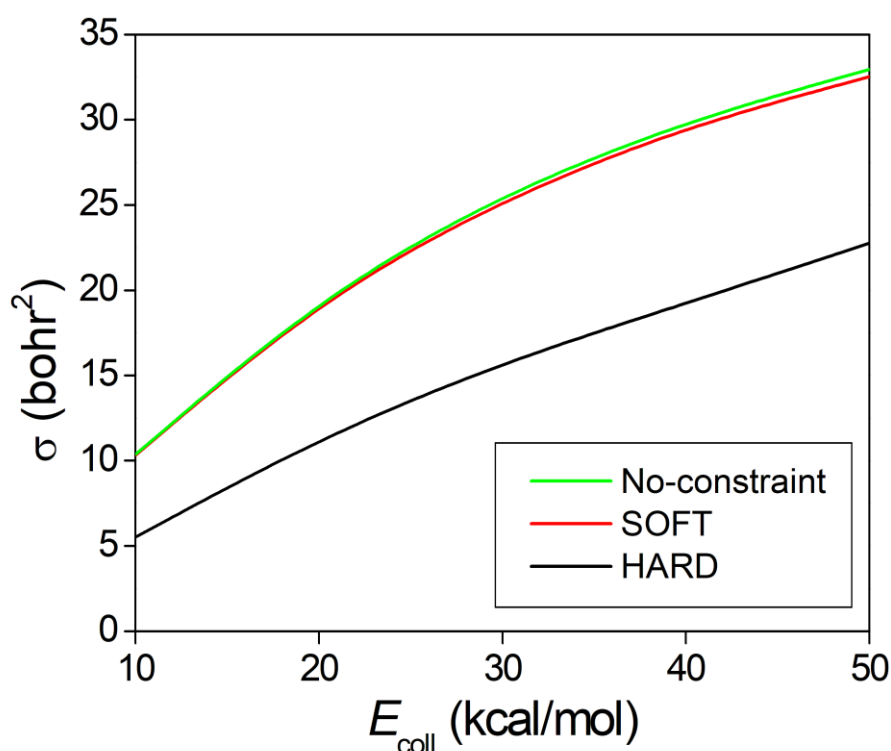
Figure 27. Integral cross sections for the ground-state OH + C$_2$H$_6$ H-abstraction reaction as a function of collision energy both with and without SOFT and HARD ZPE constraints. Taken from Ref. [2].

It can be observed that with the increase in collision energy, the ICS values also increase. While the SOFT constraint has no significant effect on the cross sections, applying the HARD approach results in ICS values decreasing by approximately half. The relatively minor collision energy dependence of the ZPE violation implies that there is no significant energy

transfer between the initial translational energy and the final vibrational states or this energy transfer is independent of collision energy.

Figure 28 illustrates reaction probabilities for H-abstraction as a function of impact parameters referred to as opacity function.
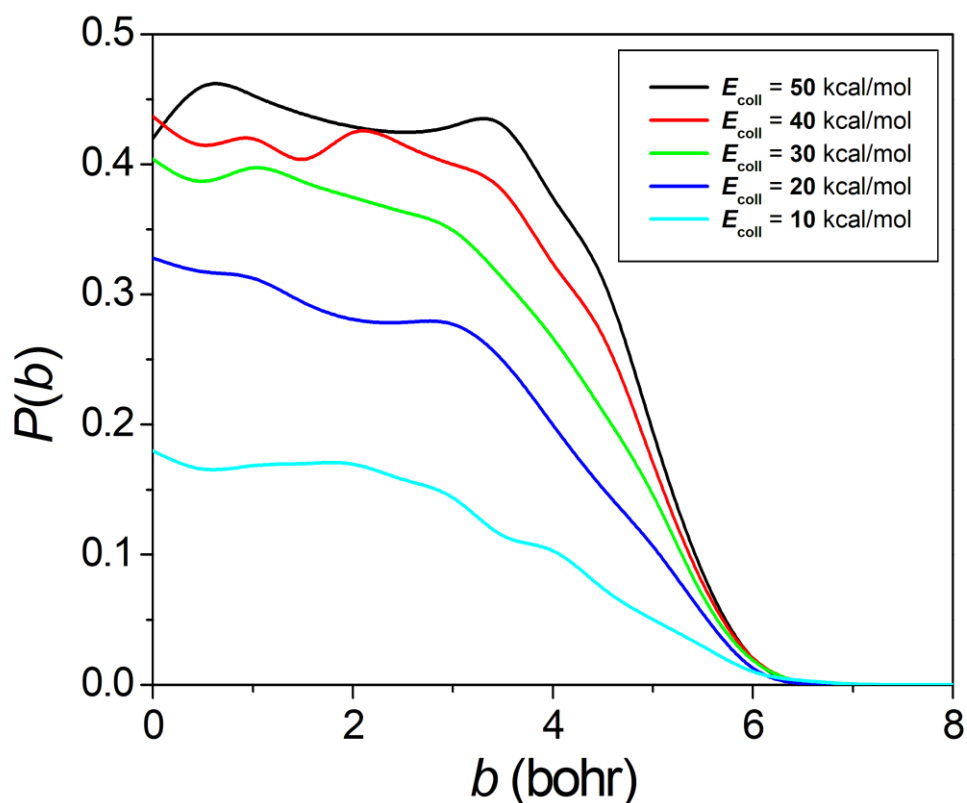
Figure 28. Reaction probabilities for the ground-state OH + C_2H_6 H-abstraction reaction as a function of the impact parameter at collision energies of 10, 20, 30, 40, and 50 kcal/mol. Taken from Ref. [2].

It can be concluded that the maximum impact parameter value, above which no reactive trajectory can be observed, is located at 6.5 bohr, which is independent of collision energy. Observing the reaction probabilities for a head-on collision ($b = 0$), it can be seen that when the collision energy increases from 10 to 20 kcal/mol, the quantity of H-abstraction products roughly increases by a factor of 1.8. However, with an additional 10 kcal/mol increase in collision energy, this kind of reactivity enhancement becomes much smaller as the reaction probability increases by only an additional 7% (from approximately $P = 33\%$ to

40%). Subsequently, the reaction probabilities do not significantly differ within the 30-50 kcal/mol collision energy range. The increasing cross section values shown earlier (**Fig. 27**) can be explained by the shape of the opacity curves as at low collision energy (E_{coll} = 10 kcal/mol), the reaction probability decreases nearly monotonically as the impact parameter increases, while at higher collision energies (E_{coll} = 20-50 kcal/mol), the reaction probability remains nearly constant up to b = 4 bohr, then suddenly decreases. Thus as collision energy increases, higher impact parameter values come into play more prominently. This implies that at low collision energies, the direct-rebound mechanism favoring smaller impact parameter values, prevails, whereas as collision energy increases, the dominance shifts towards the direct-stripping mechanism, which prefers larger b values. **Figure 29** displays the scattering angle distributions at various collision energies, which corroborates the earlier observation.
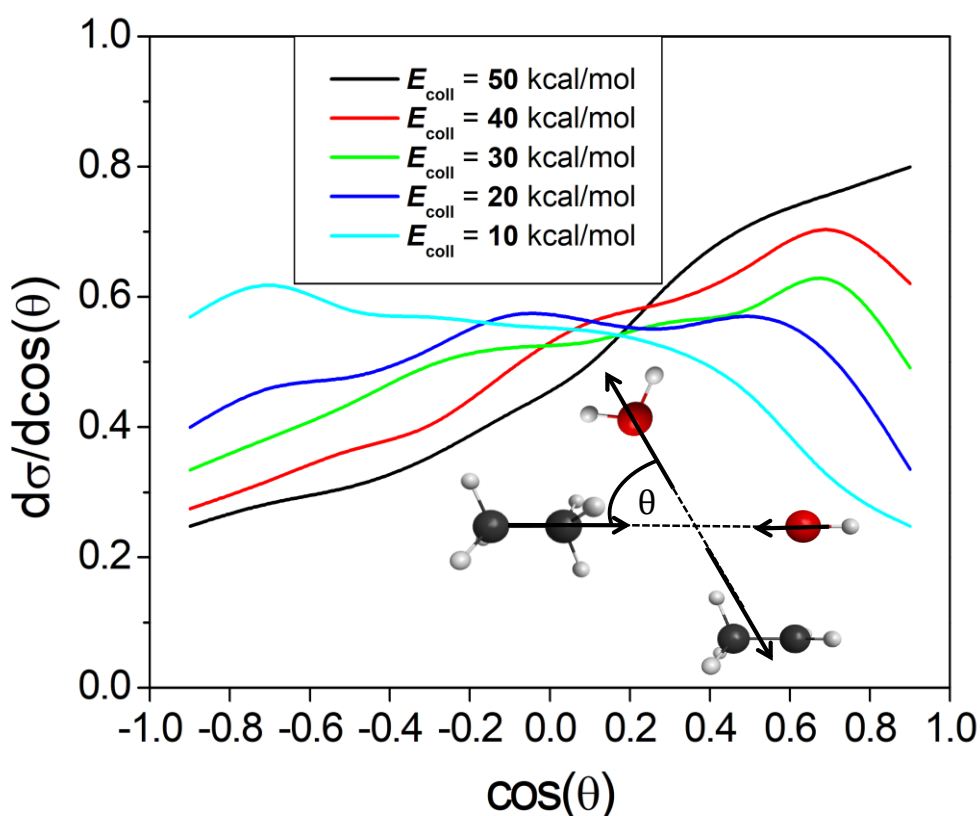
Figure 29. Normalized scattering angle distributions for the ground-state OH + C_2H_6 H-abstraction reaction at collision energies of 10, 20, 30, 40 and 50 kcal/mol. Taken from Ref. [2].

It can be seen that as we progress from 10 kcal/mol collision energy towards 50 kcal/mol, the phenomenon of forward scattering becomes increasingly prominent. Thus, while at lower collision energies the direct rebound mechanism is more significant, at higher collision energies the direct stripping mechanism becomes more preferred. Furthermore, an isotropic distribution is most notably observed at 10 kcal/mol collision energy, indicating complex formation during the reaction, thereby also suggesting the indirect nature of the reaction. The initial attack angle distributions for the two reactants are illustrated in **Figure 30** across different collision energies.
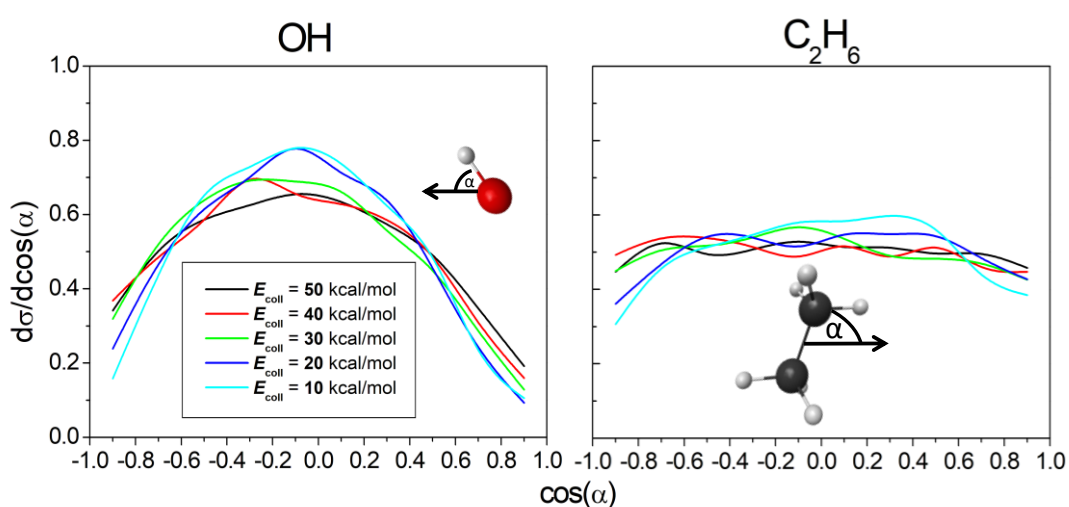
Figure 30. Normalized initial attack angle distributions for the ground-state OH + C_2H_6 H-abstraction reaction at collision energies of 10, 20, 30, 40 and 50 kcal/mol. Taken from Ref. [2].

When $\cos(\alpha) = -1$, it indicates that the OH radical approaches the ethane molecule with its oxygen atom facing, while for $\cos(\alpha) = 1$, the OH radical approaches the ethane molecule with its hydrogen atom facing. The distributions indicate a preference for the O-side attack of the OH radical over the H-side attack, as anticipated, due to the formation of an O–H bond during the abstraction process. However, this preference for O-side attack is not particularly pronounced. Surprisingly, a side-on attack of the OH radical is notably favored compared to both the O-side and H-side attacks, with the distributions peaking at $\alpha = 90°$, particularly at low collision energies. This observation can be explained by the structure of the transition state (HA TS) of the reaction, as the angle of the H–O–H bond at the TS is close to 90°. Examining the attack angle distributions of the C_2H_6 reactant, a slight inclination toward a side-on attack is indeed observed, particularly at lower collision

energies, consistent with the earlier observations. However, as collision energy increases, the attack angle distribution of C_2H_6 becomes increasingly isotropic, suggesting that the C_2H_6 molecule behaves as if it were spherical. Furthermore, it is worth mentioning that reflecting the symmetry of the C_2H_6 molecule, the attack angle distribution should be symmetric in terms of back-side–front-side, as can be seen in the right panel of **Figure 30** within the statistical accuracy.

Figure 31 illustrates the relative translational energy distributions of the products ($H_2O + C_2H_5$) at various collision energies.
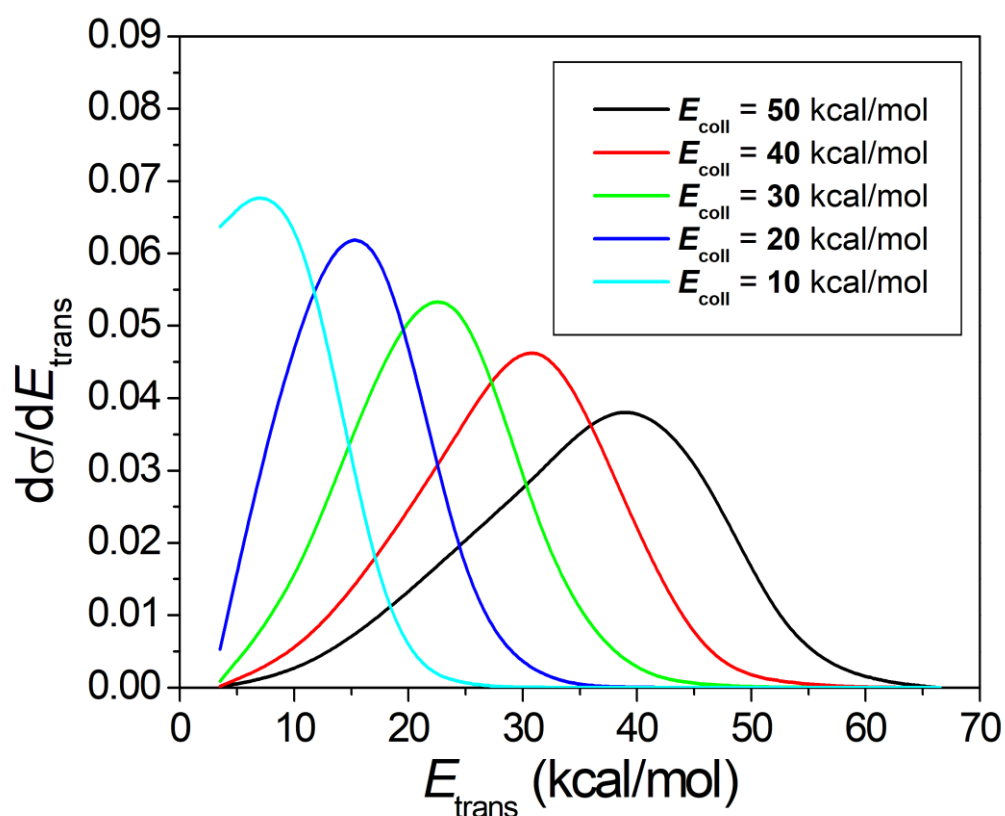
Figure 31. Normalized distributions of the product relative translational energy for the ground-state OH + C_2H_6 H-abstraction reaction at collision energies of 10, 20, 30, 40 and 50 kcal/mol. Taken from Ref. [2].

It can be observed that as collision energy increases the distributions shift towards higher translational energies and become broader. Additionally, the displacement of the distribution peaks corresponds to the magnitude of the collision energy increase suggesting

efficient translational energy transfer between reactants and products. Observing the shape of the distributions, it can be seen that the curves broaden and shift towards higher translational energies as collision energy increases indicating that with the increase in collision energy the direct nature of the reaction becomes more prominent, which is consistent with the scattering angle distributions.

Figure 32 illustrates the internal energy distributions of the H_2O and C_2H_5 products along with their decompositions into vibrational and rotational components. It can be observed that relative to the ZPE, the internal energy distribution for H_2O is much hotter compared to that of C_2H_5. Additionally, while only minor ZPE violation is noticed in the case of H_2O, it is much more significant for C_2H_5. The displacement of the peak of the vibrational energy distribution of H_2O towards higher vibrational energies compared to the ZPE suggests the formation of vibrationally-excited H_2O during the reaction, which can be explained by the elongated O-H bond in the reactant-like transitional state. Moreover, it can be observed that the vibrational energy distributions undergo a slight broadening and their peaks shift slightly towards lower vibrational energies as collision energy increases. This suggests that only a marginal amount of collision energy is transferred into the internal degrees of freedom of the products. It is worth noting that the vibrational energy distributions of H_2O are colder by approximately 10 kcal/mol compared to the internal energy distributions and the magnitude of the collision energy dependence is smaller and opposite in direction in the two cases. In contrast to the vibrational energy distribution of the H_2O product, we observe that in the case of rotational energy distribution as the collision energy increases, the peaks of the distributions shift towards higher rotational energies. From this, we can infer that the slight blue-shift observed in the internal energy distribution of H_2O arises from translational-rotational energy transfer. In the case of the C_2H_5 rotational energy distribution, it can be observed that similar to the co-product H_2O, as the collision energy increases the distributions shift towards higher rotational energies, although to a lesser extent. The vibrational energy distribution of C_2H_5 shows a reduced dependence on collision energy with peaks shifting towards lower vibrational energies more prominently than in the case of the internal energy distributions. The conclusions drawn thus far align with the impact of ZPE constraints on cross-sections.
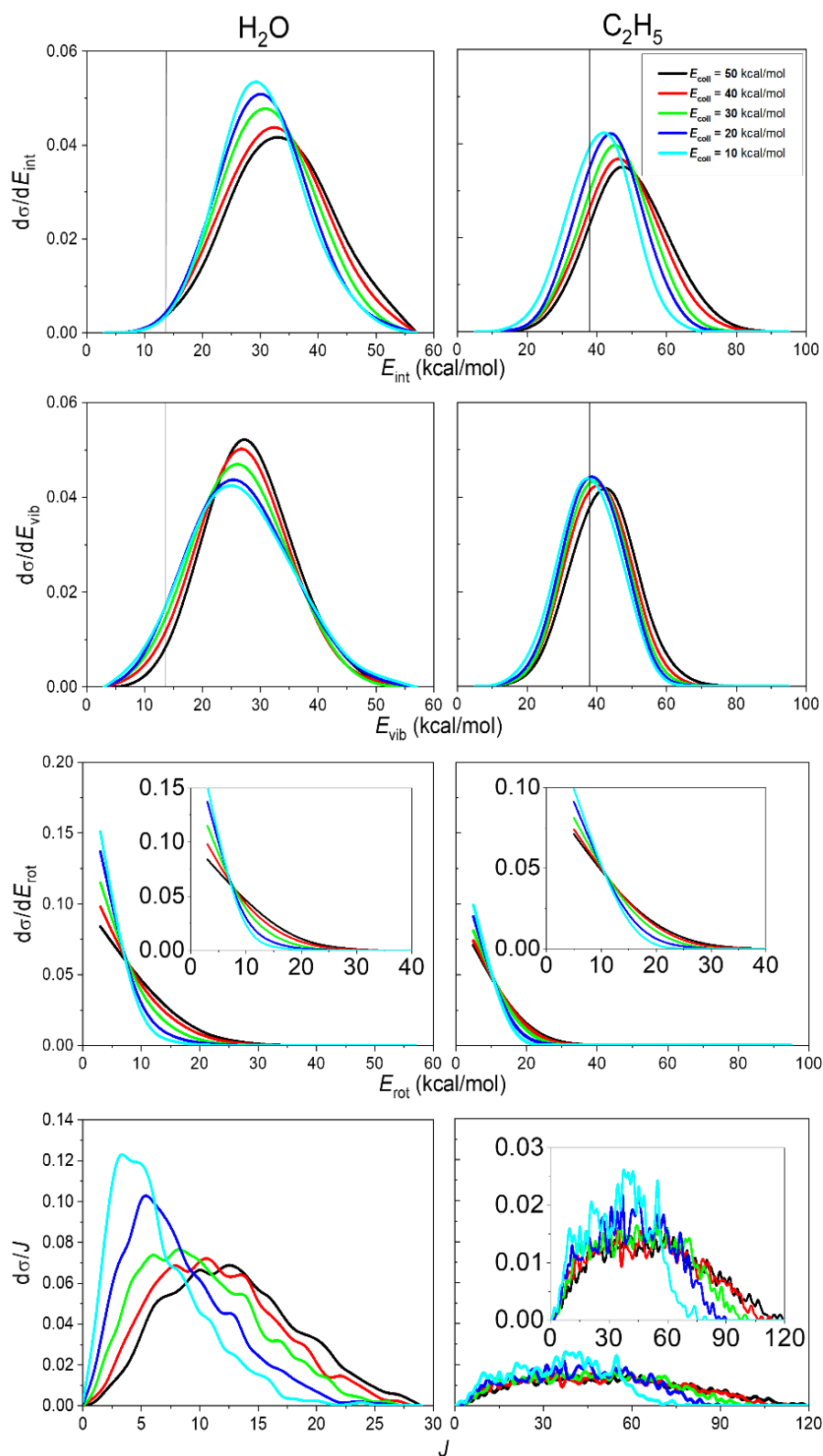
Figure 32. Distributions of the normalized internal energy (E_{int}), vibrational energy (E_{vib}), rotational energy (E_{rot}) and rotational quantum number (J) values for the H_2O and C_2H_5 products resulting from the OH + C_2H_6 H-abstraction reaction at various collision energies obtained without ZPE constraint. Vertical lines denote the ZPEs of the products. Taken from Ref. [2].

The vibrational excitation of H_2O can compensate for the ZPE violation observed in the vibrational energy distribution of C_2H_5 and conversely, in some cases, the reverse may also occur, thus the SOFT constraint only minimally affects the ICS values. Since the vibrational energy distribution of C_2H_5 exhibits significant ZPE violation applying the HARD constraint results in a much more drastic decrease in the ICS values as under the HARD constraint the vibrational energy of each product species must individually exceed its associated ZPE. Furthermore, it can be seen that the rotational quantum number value (J) distributions for both H_2O and C_2H_5 broaden and the peaks shift towards higher J values as the collision energy increases reflecting the observations made for the rotational energy distributions. For H_2O, the J values range from 0 to 30, while for C_2H_5, this range extends wider with values ranging from 0 to 120. This discrepancy can be explained by the fact that C_2H_5 possesses much greater moments of inertia compared to H_2O.

3.3.2 OH + C_2H_6 ($v = 1$)

3.3.2.1 *Computational details*

The OH + C_2H_6 reaction is studied by conducting QCT computations, where for each simulation at the beginning one of the five selected vibrational modes of the ethane molecule or the single vibrational mode of the OH radical is excited with one quantum. Just like in the ground-state reaction, QCT simulations are executed at collision energies of 10, 20, 30, 40, and 50 kcal/mol. The initial vibrational states of the OH and C_2H_6 molecules are determined through normal mode sampling. The orientations of the reactants undergo random rotations. The initial distance between the center of masses of the reactants is calculated as $\sqrt{x^2 + b^2}$, where x = 18.90 bohrs (10 Å) and the impact parameter b is varied in increments of 0.5 bohr spanning from 0 to 8 bohrs. We carry out 1000 simulations for each collision energy and impact parameter combination repeating the process for every normal mode excitation resulting in a total of 510 000 trajectories to comprehensively study the system. The trajectories are propagated until the largest interatomic distance exceeds the initial maximum by one bohr employing a time step of 0.0726 fs.

3.3.2.2 *Results*

As mentioned earlier, for the OH + C_2H_6 system, we also conduct QCT simulations where one of the reactants is excited in a selected vibrational mode by one quantum. In

Figure 33, the five selected vibrational modes for C_2H_6 and one for OH are depicted, which are excited at the beginning of the trajectories by one quantum.
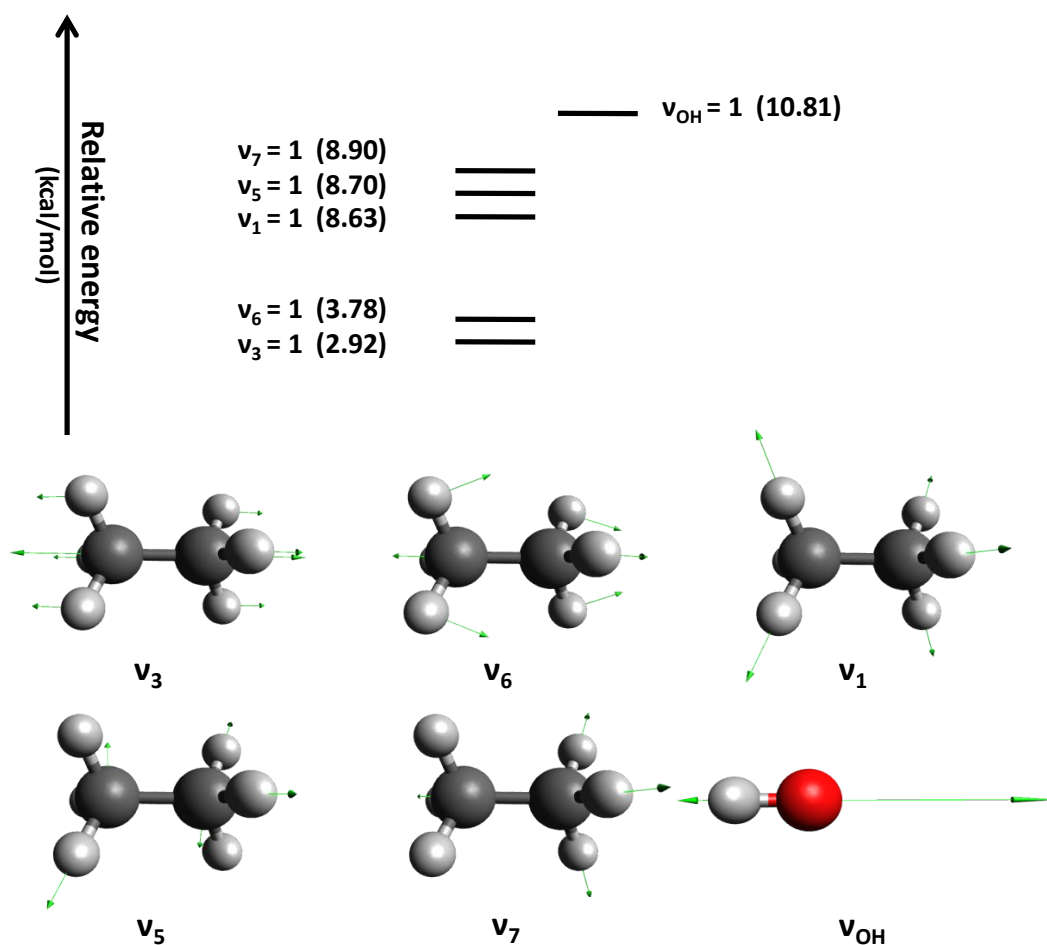

Figure 33. Representation of the normal-mode vibrations of C_2H_6 and OH. These include: ν_3 = C-C stretching, ν_6 = CH_3 deformation, ν_1 = symmetric CH stretching, ν_5 = asymmetric CH stretching, ν_7 = degenerate CH stretching and ν_{OH} = OH stretching labeled according to the standard Mulliken notations, where ν_x [x = 1, 3, 5, 6, 7]. Adapted from Ref. [4].

Among the vibrational modes of C_2H_6, the C–C stretching (ν_3), the CH_3 deformation (ν_6), and three types of CH stretching are considered: symmetric (ν_1), asymmetric (ν_5), and degenerate (ν_7). For the OH radical, the single vibrational mode (ν_{OH}) of the molecule is excited before we begin the simulations.

Figure 34 depicts the integral cross sections for the OH + C_2H_6 H-abstraction reaction, showing variations with total (E_{tot} = initial translational + vibrational) and collision

energy (E_{coll}). Furthermore, the ratios of ICSs between excited and unexcited initial states as a function of collision energy with and without the presence of soft and hard constraints are illustrated.
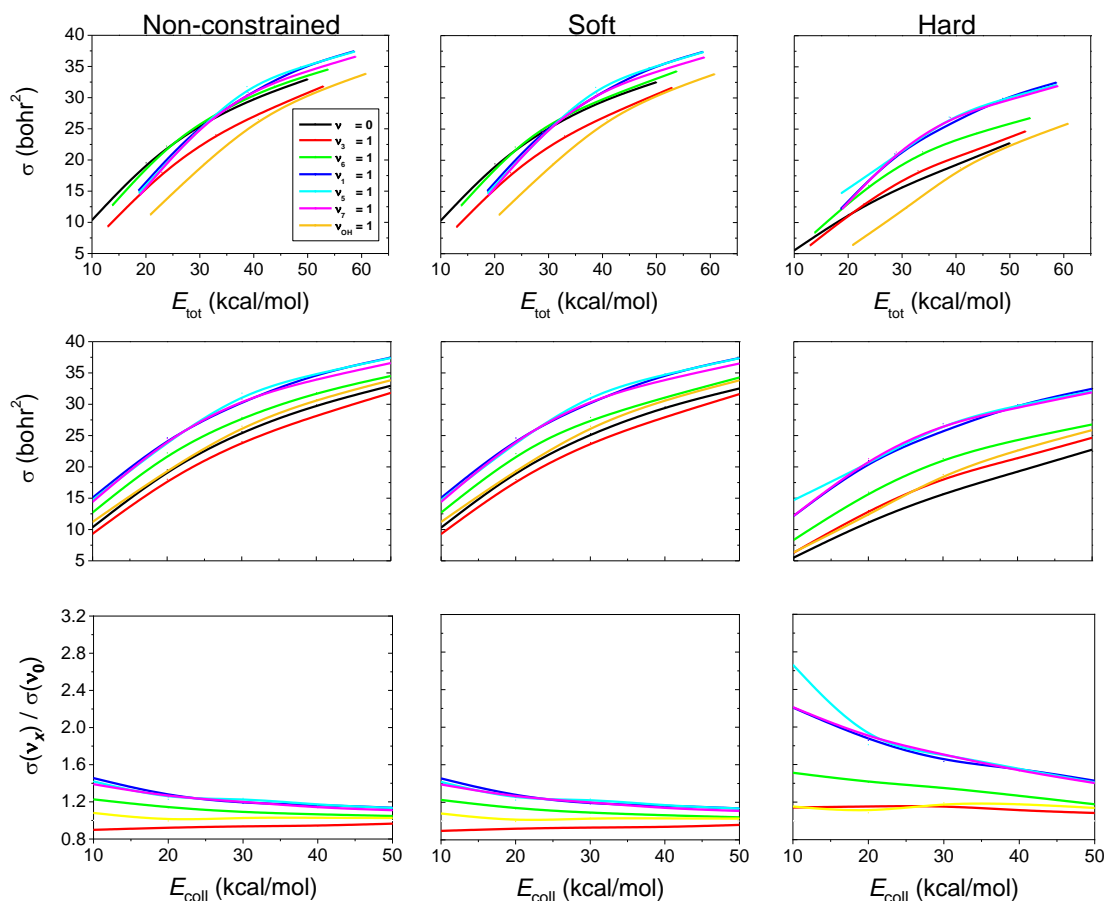
Figure 34. Integral cross sections of the OH + C_2H_6 H-abstraction reaction in terms of total energy (E_{tot} = collision energy + vibrational excitation energy, upper panels) and collision energy (E_{coll}) (middle panels). Additionally, the ratios of integral cross sections for reactions involving OH(ν_{OH} = 0) + C_2H_6(ν_x = 1) and OH(ν_{OH} = 1) + C_2H_6(ν = 0), where x = 3, 6, 1, 5, 7, are shown relative to the ground-state OH(ν_{OH} = 0) + C_2H_6(ν = 0) reaction as a function of collision energy (lower panels). These results are obtained both without and with soft and hard ZPE constraints. Taken from Ref. [4].

It can be observed that for each initial normal mode excitation, the ICS values continuously increase as the collision energy increases. Analyzing the relationship between the cross sections and total energy in the absence of ZPE constraints and under SOFT constraints, it

can be stated that except for the excitation of the C−C and O−H stretching modes, each vibrational mode exhibits higher reactivity compared to the unexcited reaction. When applying HARD constraints on ZPE, only the excitation of the vibrational mode of the OH radical leads to reduced reactivity. Considering the collision energy dependence of the cross section, it can be concluded that pre-excitation of the stretching mode of OH molecule barely alters the reactivity. This can be explained by the fact that this vibrational mode only plays a spectator role since the bond within OH does not break during the H-abstraction reaction. Moreover, when observing the collision energy dependence of the cross sections in the non-constrained and SOFT cases, it can be concluded that except for the pre-excitation of the C−C stretching the reactivity is higher compared to the unexcited case. Under HARD constraint, exciting any normal mode leads to increased reactivity relative to the unexcited state. While the impact of SOFT constraint is minor, HARD constraint cause a significant decrease in ICS. It can be observed that the greater increase in reactivity is induced by the pre-excitation of three types of C−H stretching (ν_1, ν_5 and ν_7), which is particularly noticeable under HARD ZPE constraints, whether we consider the dependence on total or collision energy of the cross section. This is not surprising as in the H-abstraction reaction an H atom bonded to a C atom is abstracted by the OH radical. It is worth mentioning that pre-excitation of the CH_3 deformation mode of the C_2H_6 molecule also noticeably enhances reactivity, although to a lesser extent compared to pre-excitation of the C−H stretching modes only about half as much. The validity of Polanyi rules can be ascertained through the dependence of cross sections on total energy. As illustrated in **Figures 7**, **8** and **25**, the transition state associated with the OH + C_2H_6 H-abstraction reaction pathway bears greater resemblance to the reactants. Thus, according to the Polanyi rules, we expect that increasing reactivity can be more efficiently achieved by raising collision energy rather than by exciting certain vibrational modes of the reactants. This implies that at a given total energy, where the collision energy is maximal, the highest reactivity is expected to be attained. In the case of this particular reaction this holds true if we excite either the C−C bond in the C_2H_6 molecule (ν_3) or the single bond in the OH radical (ν_{OH}). However, contradictory results are obtained with respect to the Polanyi rules when exciting the other vibrational normal modes (ν_1, ν_5, ν_6 and ν_7), as in these cases greater increases in reactivity are achieved by pre-excitation of the reactants. The deviations from the Polanyi rules can be attributed to the fact that these rules are formulated for A + BC

type reactions, *i.e.*, reactions involving an atom and a diatomic molecule. However, in our case, the OH + C_2H_6 reaction represents a much more complex system, where factors such as the orientation of reactants at the moment of collision can influence the reaction kinetics and product formation to a greater extent than simply described by the Polanyi rules.

In **Figure 35**, the reaction probabilities pertaining to the OH + C_2H_6 hydrogen-abstraction reaction are depicted as functions of impact parameter. Below them are the normalized scattering angle distributions followed by the normalized initial attack angle distributions for the reactant OH and C_2H_6 and finally, the distributions of product relative translational energies at various collision energies. The opacity functions indicate that the maximum impact parameter is around 6.5 bohr regardless of any dependence on collision energy or initial vibrational excitation of the normal modes of the reactants. It can be observed that the red curve is always below the black one for every collision energy showing that the excitation of C−C vibrations (ν_3) decreases the probability of H-abstraction reaction compared to the unexcited reaction. At $b = 0$, the reaction probability values progressively increase as E_{coll} rises until reaching 30 kcal/mol. Beyond this threshold, there is no significant further increase in the reaction probability. Furthermore, the excitation of C−H stretching modes (ν_1, ν_5, and ν_7) evidently enhances the probabilities of the OH + C_2H_6 H-abstraction reaction. It is worth noting that all previous observations regarding the opacity functions are in excellent agreement with the information derived from the excitation functions (**Figure 34**). As discussed in the preceding chapter, there is a close relationship between the scattering angle distributions and the opacity functions. At the lowest collision energy, the reaction probabilities exhibit a continuous decrease as the impact parameter increases until around $b = 4$ bohrs, after which the curves sharply decline. With increasing collision energy larger b values become more favorable. Consequently, the rebound mechanism, which favors smaller b values, prevails at lower collision energies. As collision energy rises, the direct stripping mechanism, which favors larger b values, becomes increasingly prominent. Consistent with the pattern observed in the opacity functions, backward scattering appears at low collision energies, particularly around $E_{coll} = 10$ kcal/mol indicating the presence of the direct rebound mechanism.
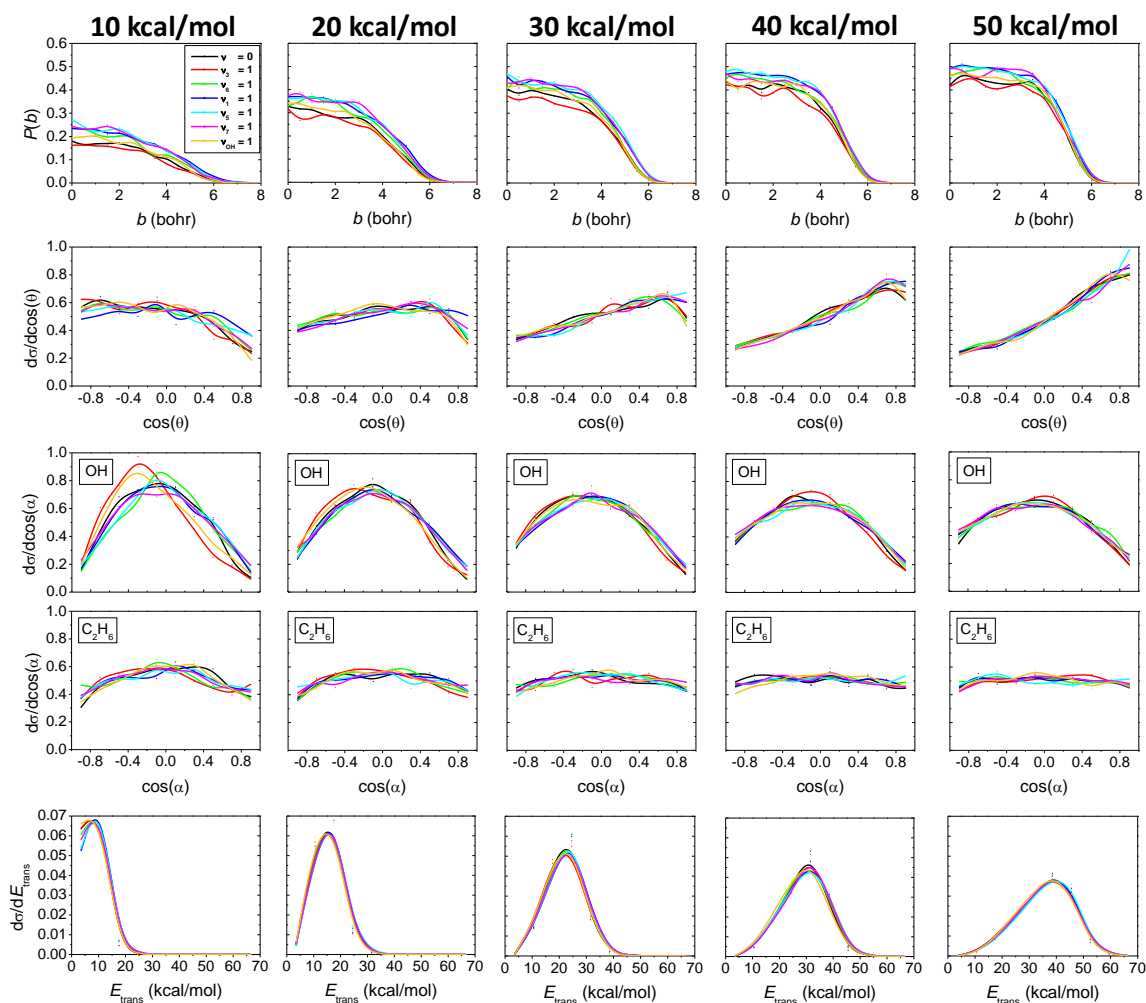
Figure 35. Arranged in a top-to-bottom fashion: reaction probabilities as a function of impact parameter, normalized scattering angle distributions, normalized initial attack angle distributions for the reactant OH and C_2H_6 molecules and normalized product relative translational energy distributions for the OH(ν_{OH} = 0) + C_2H_6(ν_x = 0, 1), x = 3, 6, 1, 5, 7 and OH(ν_{OH} = 1) + C_2H_6(ν = 0) reactions at 10, 20, 30, 40 and 50 kcal/mol collision energies. Taken from Ref. [4].

As we move to higher collision energies, forward scattering becomes increasingly common indicating the prevalence of direct stripping. Furthermore, there are slight indications of isotropic scattering, primarily observed at collision energies of 10 and 20 kcal/mol. This suggests an indirect nature for the OH + C_2H_6 H-abstraction reaction promoting complex formation through the process. There are no discernible mode-specific features in the scattering angle distributions. Taking a look at the initial attack angle distributions, we can say that for each preliminary normal mode excitation, just like in the case of the unexcited reaction, the OH radical tends to approach the C_2H_6 molecule more with its O-end than

with its H-end. This behavior, as discussed earlier, can be explained by the fact that in the H-abstraction reaction the OH radical removes a hydrogen from C_2H_6, thus forming a new O−H bond. Although the OH radical predominantly approaches the C_2H_6 molecule in a side-on manner, this can be explained by the nearly 90° H−O−H bond angle present in the transition state structure (HA TS) as mentioned previously. In the case of the initial attack angle distribution of the OH radical, at 10 kcal/mol collision energy slight mode-specific features are observed when the O−H bond in the OH radical (ν_{OH}) and the C−C bond in C_2H_6 (ν_3) are preliminarily excited as in these cases the peaks of the distributions shift towards O-end attack. Mode-specific behavior is absent at higher collision energies and the distributions become more and more isotropic as the collision energy increases. The attack angle distributions of the C_2H_6 molecule indicate a slight inclination towards side-on attack at collision energies of 10 and 20 kcal/mol. However, with increasing collision energy, the distributions become predominantly isotropic implying that the C_2H_6 molecule behaves like a spherical object. There is no mode-specific behavior evident in the initial attack angle distributions of C_2H_6. In the case of the relative translational energy distribution of the products, it can be stated that by exciting any vibrational normal mode of the reactants, as collision energy increases, the distributions widen progressively and shift towards higher translational energies indicating efficient translational energy transfer between the reactants and products. Moreover, it is observable that with increasing collision energy, the peaks of the distributions shift towards the highest attainable translational energies. This trend suggests a more direct reaction behavior as collision energy rises aligning well with the scattering angle distributions. The relative translational energy distributions of the products do not exhibit any discernible vibrational mode-specific characteristics. This suggests that the initial vibrational excitation energy primarily transfers into the internal degrees of freedom of the products.

Figure 36 and Figure 37 illustrate the distributions of internal, vibrational and rotational energies as well as the distributions of rotational quantum numbers for the H_2O and C_2H_5 products, respectively at various collision energies. First, the results related to H_2O are presented followed by those pertaining to C_2H_5.
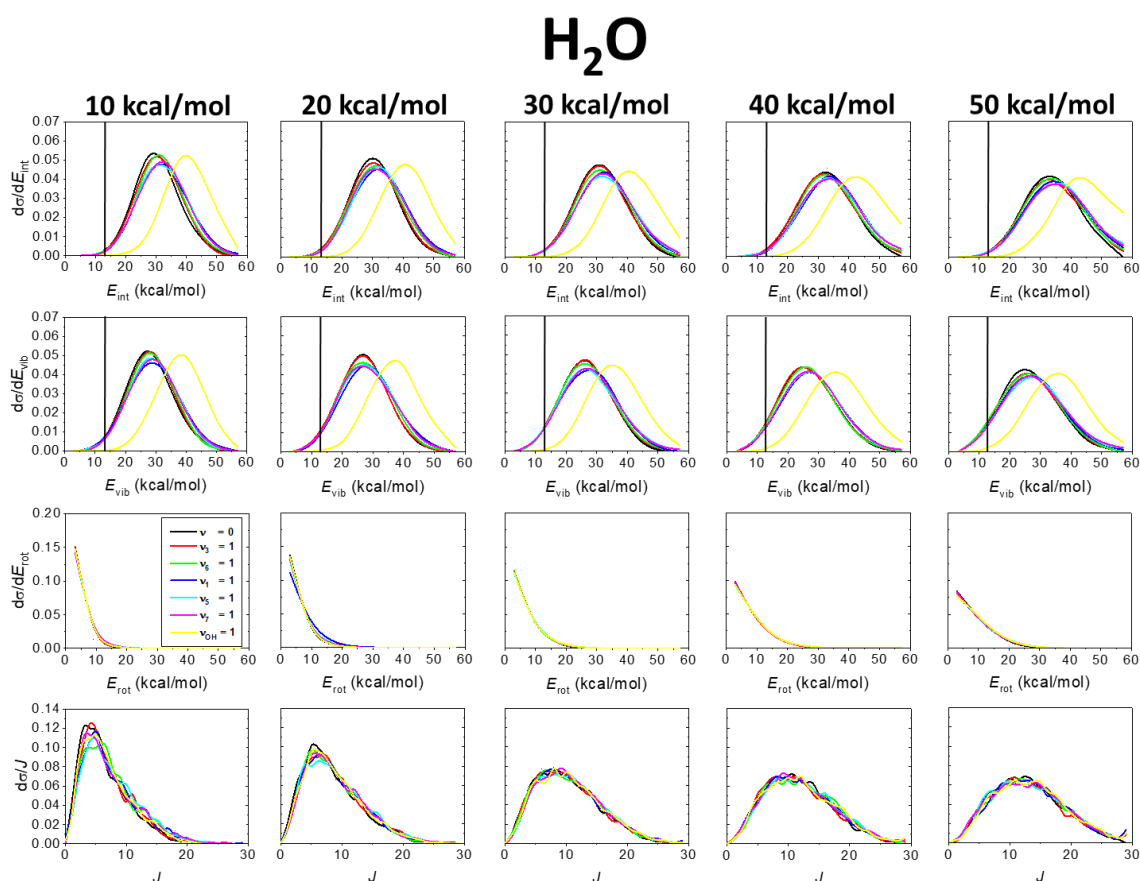
H₂O

Figure 36. Normalized distributions of the internal energy (E_{int}), vibrational energy (E_{vib}), rotational energy (E_{rot}) and rotational quantum number (J) values for the H_2O product resulting from reactions $OH(\nu_{OH} = 0) + C_2H_6(\nu_x = 0, 1)$, where x = 3, 6, 1, 5, 7, and $OH(\nu_{OH} = 1) + C_2H_6(\nu = 0)$ at 10, 20, 30, 40 and 50 kcal/mol collision energies. The vertical lines indicate the ZPE of the H_2O molecule. Taken from Ref. [4].

In the internal and vibrational energy distributions of the H_2O molecule, mode-specific characteristics clearly emerge as when the bond in the OH molecule is excited, the distributions shift towards higher energies. The extent of this shift is approximately 10 kcal/mol compared to other cases, which roughly corresponds to the excitation energy of the OH radical. This implies that the single vibrational mode present in the OH radical merely acts as a spectator in the context of the H-abstraction reaction or at the very least the energy of the initial vibrational excitation of the OH radical remains within the H_2O product. The H-abstraction reaction generates vibrationally-excited H_2O molecules, particularly when the initial OH stretching is excited. There is only a minor ZPE violation observed in the internal and vibrational energy distributions of H_2O. Furthermore, it is

103

characteristic of the internal and vibrational energy distributions of H_2O that as collision energy increases, the distributions exhibit only a slight widening and their peaks remain unchanged rather than shifting. This indicates inefficient collision energy transfer into the internal degrees of freedom of the H_2O product, which is consistent with the significant collision energy dependence observed in the translational energy distributions (**Fig. 35**). The rotational energy and rotational quantum number value distributions for the H_2O molecule slightly widen and shift towards higher energies as we progress to higher collision energies. Moreover, in the case of the rotational energy and rotational quantum number value distributions for the H_2O molecule, no mode-specific behavior is observed upon pre-excitation of any vibrational mode. For any vibrational excitation, the values of J cover the range of 0 to 30 for H_2O. Based on **Figure 37**, it can be observed that the excitation of C−H bonds in the C_2H_6 molecule results in the internal and vibrational energy distributions shifting towards higher internal and vibrational energies. This indicates that upon excitation of the C−H stretching modes, the initial vibrational excitation energy of the C_2H_6 molecule transfers into the internal degrees of freedom of C_2H_5, which is also consistent with the translational energy distributions (**Fig. 35**). For the C_2H_5 product, a more pronounced ZPE violation is observed compared to H_2O, both in terms of internal and vibrational energy distributions. Furthermore, similar to the H_2O molecule, as collision energy increases the internal and vibrational energy distributions only slightly broaden and their peaks do not shift. This also indicates that the collision energy transfer into the internal motions of the C_2H_5 product is inefficient. Regarding the rotational energy and rotational quantum number value distributions, similar to the case of H_2O, the distributions noticeably broaden and shift towards higher energies with increasing collision energy. There is no mode-specific behavior observed in the distributions of rotational energy and rotational quantum number values for the C_2H_5 product, just like in the case of H_2O. For C_2H_5, the values of J range from 0 to 120. For the H_2O molecule, the mode-specific population of individual vibrational states is also determined as shown in **Figure 38**. It can be stated that in the case of bending, the most populated vibrational state is the ground state. As collision energy increases, the initial approximately 65% population of the ground state decreases slightly dropping to around 55% at a collision energy of 50 kcal/mol.
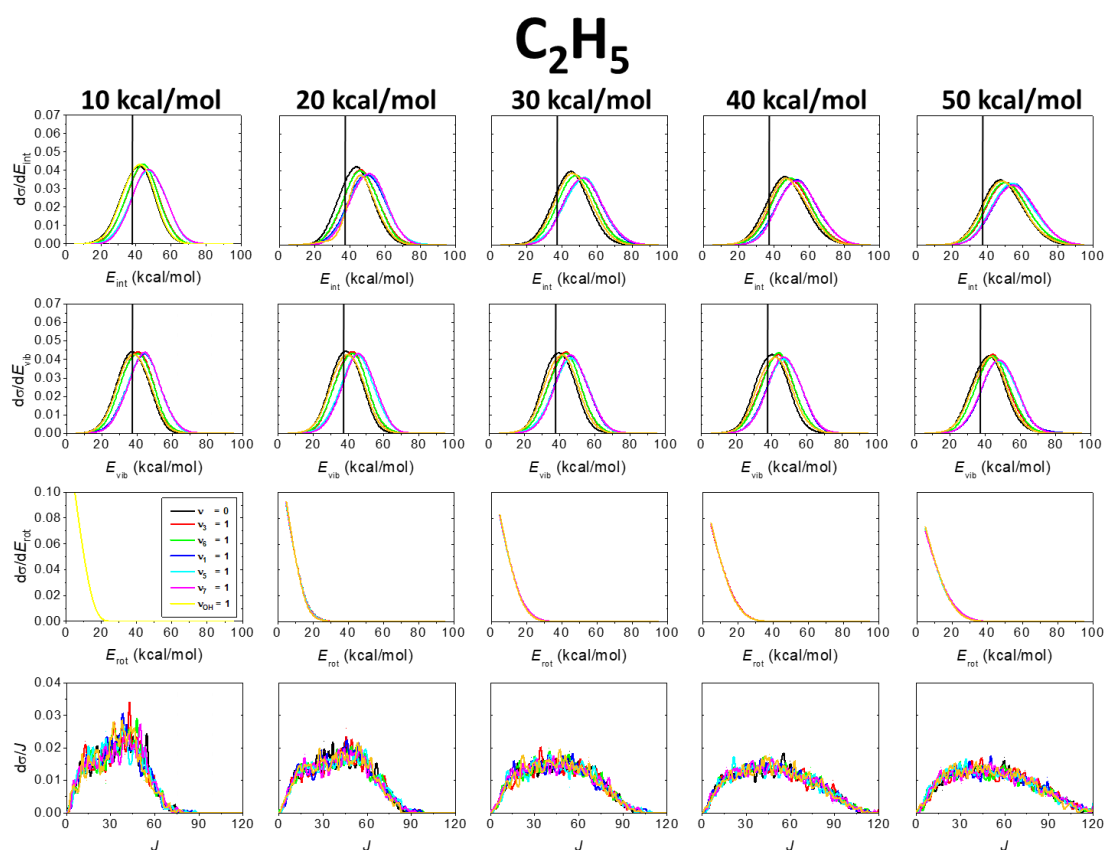
Figure 37. Normalized distributions of the internal energy (E_{int}), vibrational energy (E_{vib}), rotational energy (E_{rot}) and rotational quantum number (J) values for the C_2H_5 product resulting from reactions $OH(\nu_{OH} = 0) + C_2H_6(\nu_x = 0, 1)$, where $x = 3, 6, 1, 5, 7$, and $OH(\nu_{OH} = 1) + C_2H_6(\nu = 0)$ at 10, 20, 30, 40 and 50 kcal/mol collision energies. The vertical lines indicate the ZPE of the C_2H_5 radical. Taken from Ref. [4].

The population of the other vibrational states does not change significantly with increasing collision energy. For symmetric stretching at 10 kcal/mol collision energy, the populations of the ground and first-excited states are the highest and nearly equal, around 38-38%. As collision energy increases, the population of the ground state increases while the populations of the other vibrational states decrease slightly indicating that with increasing collision energy a lesser degree of vibrational excitation is achieved. In the case of asymmetric stretching, similar to bending, the ground state remains the most dominant. However, the difference between the populations of the ground state and the first-excited state is smaller compared to bending at all collision energies. The population of the ground state is approximately 50% at 10 kcal/mol collision energy.
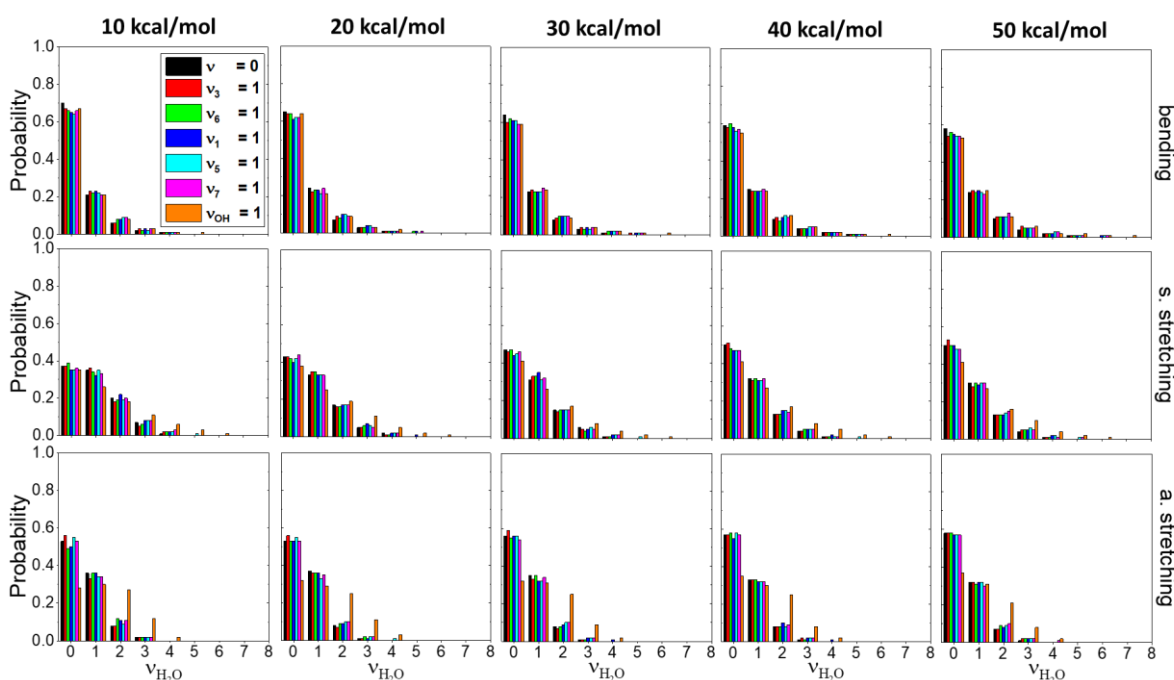
Figure 38. Mode-specific vibrational state distributions for the H_2O product resulting from the $OH(\nu_{OH} = 0) + C_2H_6(\nu_x = 0, 1)$, where x = 3, 6, 1, 5, 7, and $OH(\nu_{OH} = 1) + C_2H_6(\nu = 0)$ reactions at 10, 20, 30, 40 and 50 kcal/mol collision energies. Each distribution is normalized per mode and integrated over the other two modes. Taken from Ref. [4].

At 50 kcal/mol collision energy, it increases to around 58%, while simultaneously the population of the first-excited state remains approximately 37% and does not change significantly as we reach the highest collision energy. Upon initial excitation of the OH bond, mode-specific features become evident in the distributions of the asymmetric stretching mode, particularly notable in the $\nu = 2$ and $\nu = 3$ vibrational states. This is characterized by a decrease in the population of $\nu = 0$ and an increase in $\nu = 2$ and 3. Across all types of motion within the H_2O molecule, vibrational states are typically excited with 0, 1, 2, 3, or 4 quanta.

3.3.3 OH + glycine: H-abstraction

3.3.3.1 Computational details

The reaction dynamics of the OH + glycine system is studied at five different collision energies: 1, 5, 10, 15, and 20 kcal/mol. The reactants are initialized in their vibrational ground state through normal mode sampling with their rotational angular momentum set to zero. The orientations of the reactants are randomly rotated. The initial distance

between the centers of mass of the reactants is determined by $\sqrt{x^2 + b^2}$, where x is set to 18.90 bohrs (10 Å). The impact parameter b is incremented by 1 bohr, ranging from 0 to 18 bohr at collision energy of 1 kcal/mol, and from 0 to 10 bohr at other collision energies. For each combination of collision energy and impact parameter, we perform 1000 trajectories leading to a total of 504 000 simulations. Trajectories are computed with a time step of 0.0726 fs and are terminated when the maximum interatomic distance exceeds the largest initial distance by one bohr.

3.3.3.2 Results

In mapping the potential energy surface for the OH + glycine H-abstraction reaction, we initially considered three potential product channels. Nonetheless, the dynamics simulations reveal that when H-abstraction occurs at the carboxyl group the resulting dehydrogenated glycine molecule is susceptible to further decomposition. As a result, the reaction can ultimately yield CO_2, CH_2NH_2 and H_2O as final products. **Figure 39** provides a schematic representation of the potential energy surface highlighting the H-abstraction reaction taking place at the carboxyl group of glycine. The figure clearly shows that the energy of the new products revealed by the QCT simulations is significantly below that of the reactants. Considering the benchmark calculations, their classical(adiabatic) relative energies are −26.8(−32.2) kcal/mol. In contrast, when using the PES-calculated values their classical(adiabatic) energies are 26.5(27.5) kcal/mol below the reactant energies. This indicates that this product channel is thermodynamically highly favored. Furthermore, when accounting for the H-abstraction pathways involving the CH_2 and NH_2 groups, this three-fragment product channel emerges as the second most exothermic reaction pathway. Additionally, comparing the benchmark values with those derived from the PES shows that the developed potential provides a good description of the energy for the H_2O + CH_2NH_2 + CO_2 products excluding zero-point energy corrections. Specifically, the discrepancy between the benchmark and PES-calculated relative energies is only 0.3 kcal/mol in the classical sense, and higher at 3.7 kcal/mol in the adiabatic context.
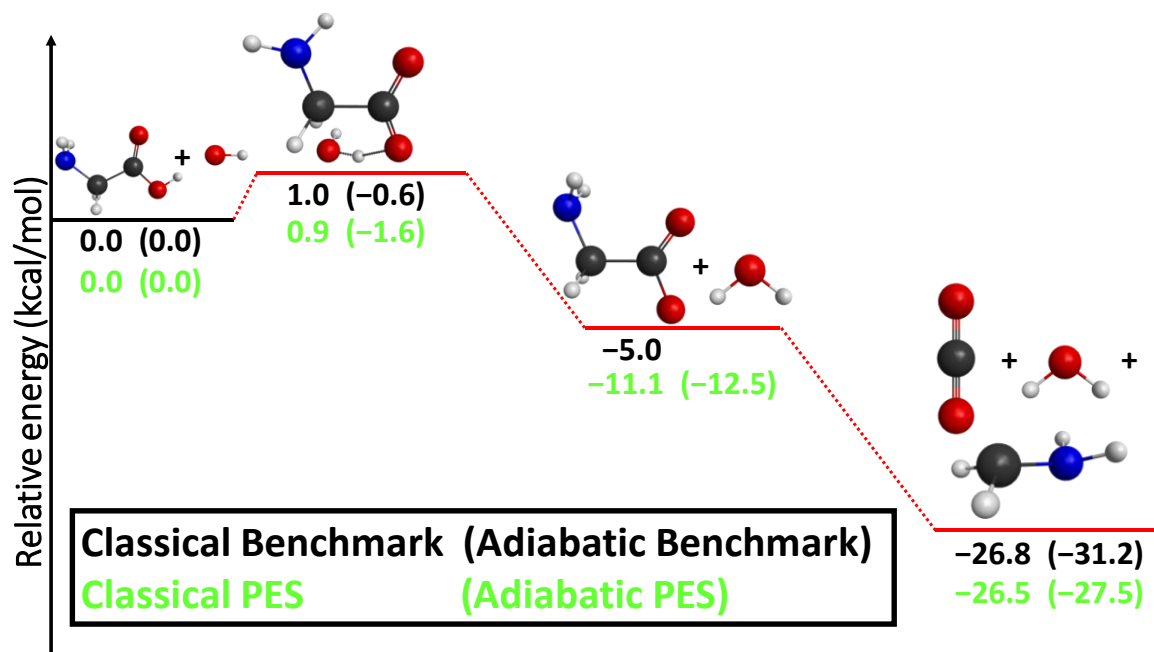
Figure 39. Schematic of the potential energy landscape for the OH + glycine H-abstraction reaction via the carboxyl group contrasting the previously-determined benchmark classical(adiabatic) energies shown in black and the classical(adiabatic) relative energies calculated from the PES depicted in green. This representation focuses solely on the energies and structures of the lowest-energy conformers.

Figure 40 depicts the variation in integral cross sections for the OH + glycine H-abstraction reactions as collision energy increases based on the different reactant conformers employed in the QCT simulations. Based on **Figure 40**, it is immediately apparent that when the H-abstraction occurs at the carboxyl group, the reaction almost always concludes with the decomposition of the dehydrogenated glycine molecule resulting in CO_2 and CH_2NH_2 products along with the H_2O molecule. It is clear that no matter which glycine conformer is utilized to start the trajectories, the curves exhibit a very similar pattern in all eight scenarios. At collision energy of 1 kcal/mol, the dominant product channel is H_2O + CH_2NH_2 + CO_2. Between approximately 5 and 10 kcal/mol collision energies, this reaction pathway reaches a minimum ICS value followed by a roughly constant reactivity. For the H-abstraction reactions occurring at the CH_2 and NH_2 groups, the reactivity increases with rising collision energy.
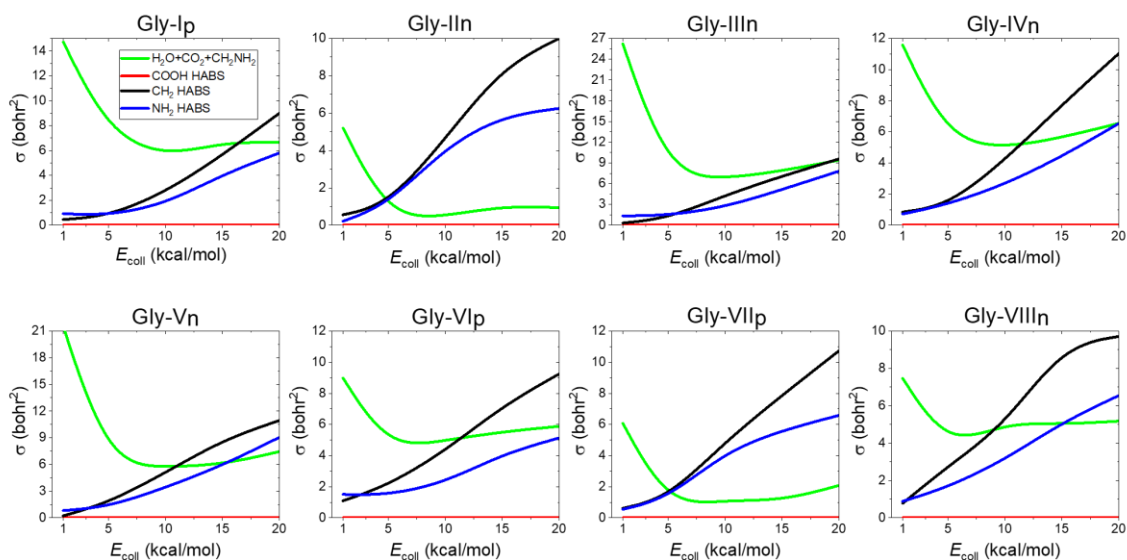
Figure 40. The integral cross sections for the OH + glycine H-abstraction reaction as a function of collision energy presented without any constraints.

In the case of the reaction at the CH_2 group, by the time the collision energy reaches 20 kcal/mol the ICS values exceed the reactivity of the three-fragment product channel for all glycine conformers. Furthermore, it can be observed that at collision energy of 1 kcal/mol the reactivity of the H-abstraction occurring at the amino group is slightly higher than that of the reaction at the CH_2 group. However, as the collision energy increases, the CH_2 H-abstraction gradually becomes more dominant for all reactant conformers.

Figure 41 shows the reaction probabilities for the OH + glycine H-abstraction reaction as a function of impact parameters. For the CH_2 and NH_2 H-abstraction reactions regardless of the reactant conformer, the maximum impact parameter is consistently around 7.5-8 bohr independent of the collision energy. In contrast, for the three-fragment product channel, the maximum impact parameter is dependent on collision energy with its value increasing as the collision energy rises. In this case, the maximum impact parameter value for each reactant conformer is estimated to be around 17-18 bohr at a collision energy of 1 kcal/mol. This value decreases significantly as the maximum impact parameter appears at approximately 9-11 bohr for a collision energy of 5 kcal/mol and further drops to 8-9 bohr at the three lowest collision energies.
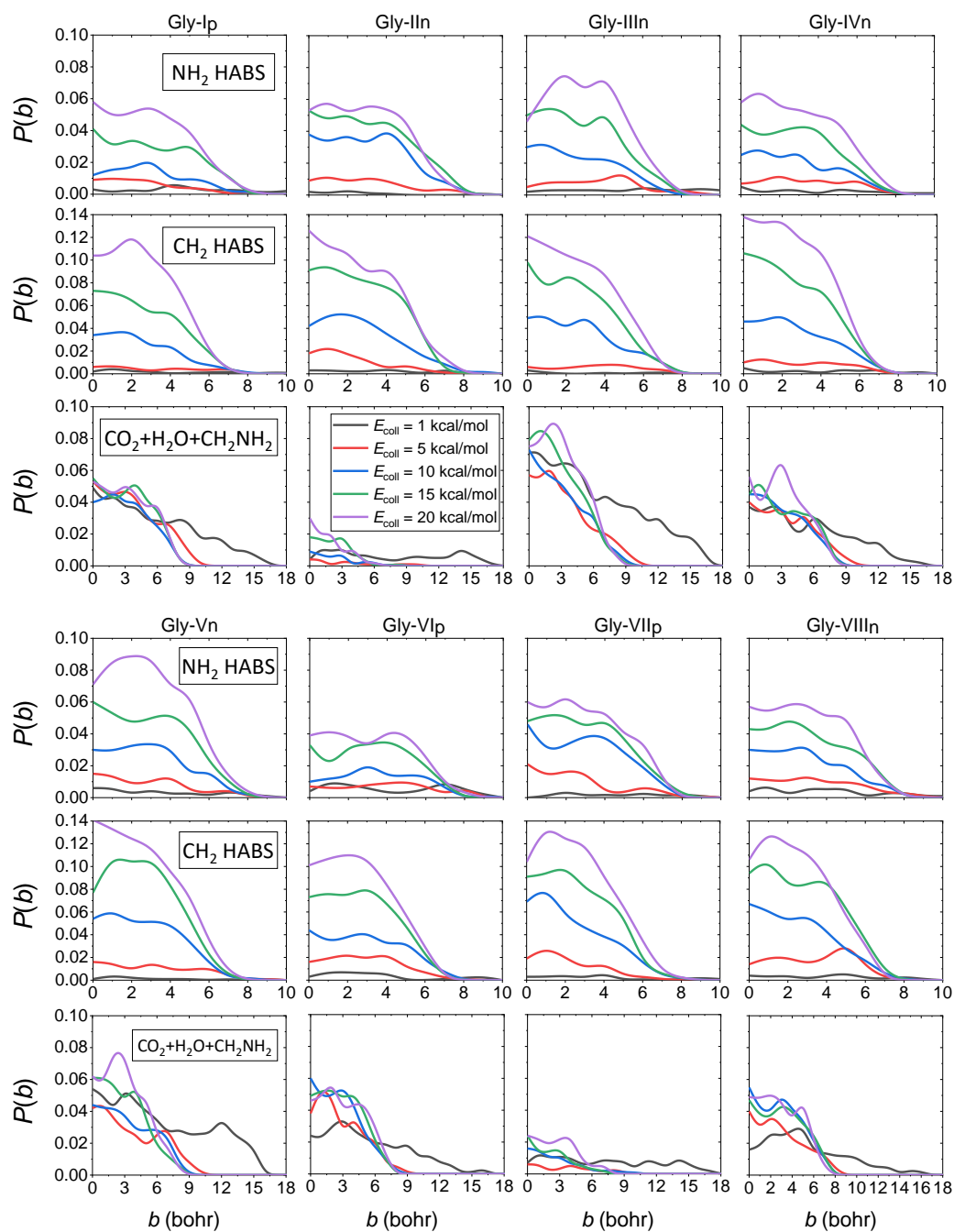
Figure 41. Reaction probabilities for the OH + glycine NH_2 and CH_2 H-abstraction as well as the COOH H-abstraction resulting in CO_2, CH_2NH_2 and H_2O products as a function of the impact parameter at collision energies of 1, 5, 10, 15 and 20 kcal/mol.

The observed increase in cross-section values for the NH_2 and CH_2 H-abstraction reaction channels, as depicted earlier in **Figure 40**, can be explained similarly to the OH + C_2H_6 H-abstraction reaction by the behavior of the opacity curves. At lower collision energies ($E_{coll} = 1$ and 5 kcal/mol), the reaction probability steadily decreases with increasing

impact parameter. However, at higher collision energies (E_{coll} = 10-20 kcal/mol), the reaction probability stays almost constant up to a specific impact parameter that is dependent on the initial glycine conformer after which it suddenly drops. Furthermore, the shape of the ICS curves for H-abstraction reactions occurring at the carboxyl group can also be explained by the changes in reaction probabilities as a function of the impact parameter. In this case, the cross sections are largest at 1 kcal/mol, which is expected based on the opacity function. At E_{coll} = 1 kcal/mol, the maximum impact parameter is significantly larger compared to other collision energies, greatly contributing to the increase in ICS. Subsequently, between E_{coll} = 5-10 kcal/mol, the cross sections reach their minimum value and then remain around a constant level. This behavior is attributed to the significant decrease in the maximum impact parameter and the fact that reaction probabilities do not vary significantly but oscillate within 1-2 % regardless of the collision energy.

Figure 42 shows the scattering angle distributions for the OH + glycine H-abstraction reaction at different collision energies. It can generally be stated that for H-abstraction reactions occurring at the NH_2 and CH_2 groups, similar scattering angle distributions are observed for a given glycine conformer. The scattering angle distributions for some glycine conformers show slight forward scattering, but in most cases predominantly isotropic distributions are observed. This can be explained by the fact that hydrogen bonds may form between the glycine molecule and the OH radical making the reaction highly indirect and resulting in isotropic scattering angle distributions. Additionally, the scattering angle distributions do not exhibit significant dependence on collision energy for any of the glycine conformers.

Figure 43 illustrates the initial angle of attack distributions for the reactant OH at various collision energies. When cos(α) = −1, it means the OH radical is approaching the glycine molecule with its oxygen atom in the lead, while cos(α) = 1 indicates that the hydrogen atom of the OH radical is facing the glycine molecule. In the case of NH_2 H-abstraction for conformers IIn and VIIp, there is a slight preference for the OH radical to approach the glycine molecule with its hydrogen side facing. However, for the other glycine conformers the distributions are more isotropic indicating no significant preference for which side of the OH radical faces the glycine molecule.
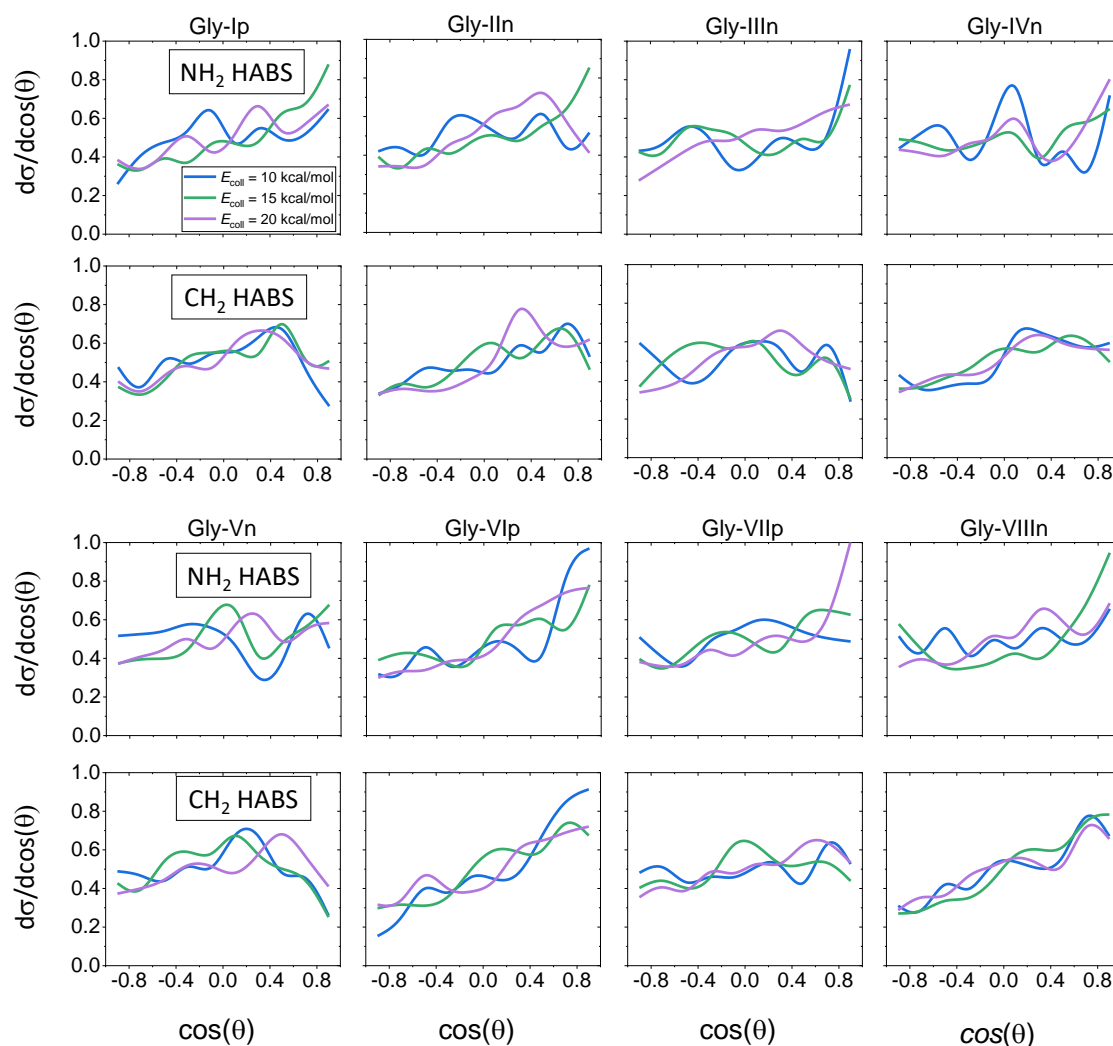
Figure 42. Normalized scattering angle distributions for the OH + glycine H-abstraction reaction at the NH$_2$ and CH$_2$ groups at collision energies of 10, 15 and 20 kcal/mol.

Additionally, the QCT simulations for the Ip glycine conformers suggest a mild preference for the OH radical to approach the glycine molecule in a side-on orientation, similar to what is observed in the OH + C$_2$H$_6$ reaction. For the other two reaction pathways, isotropic distributions are observed for all glycine conformers. The isotropic distribution indicates that even if the OH radical attacks with its hydrogen atom, H-abstraction can still occur. This is because after forming a hydrogen bond, the OH radical can adopt a reactive orientation due to intermolecular interactions with the functional groups of the glycine molecule.
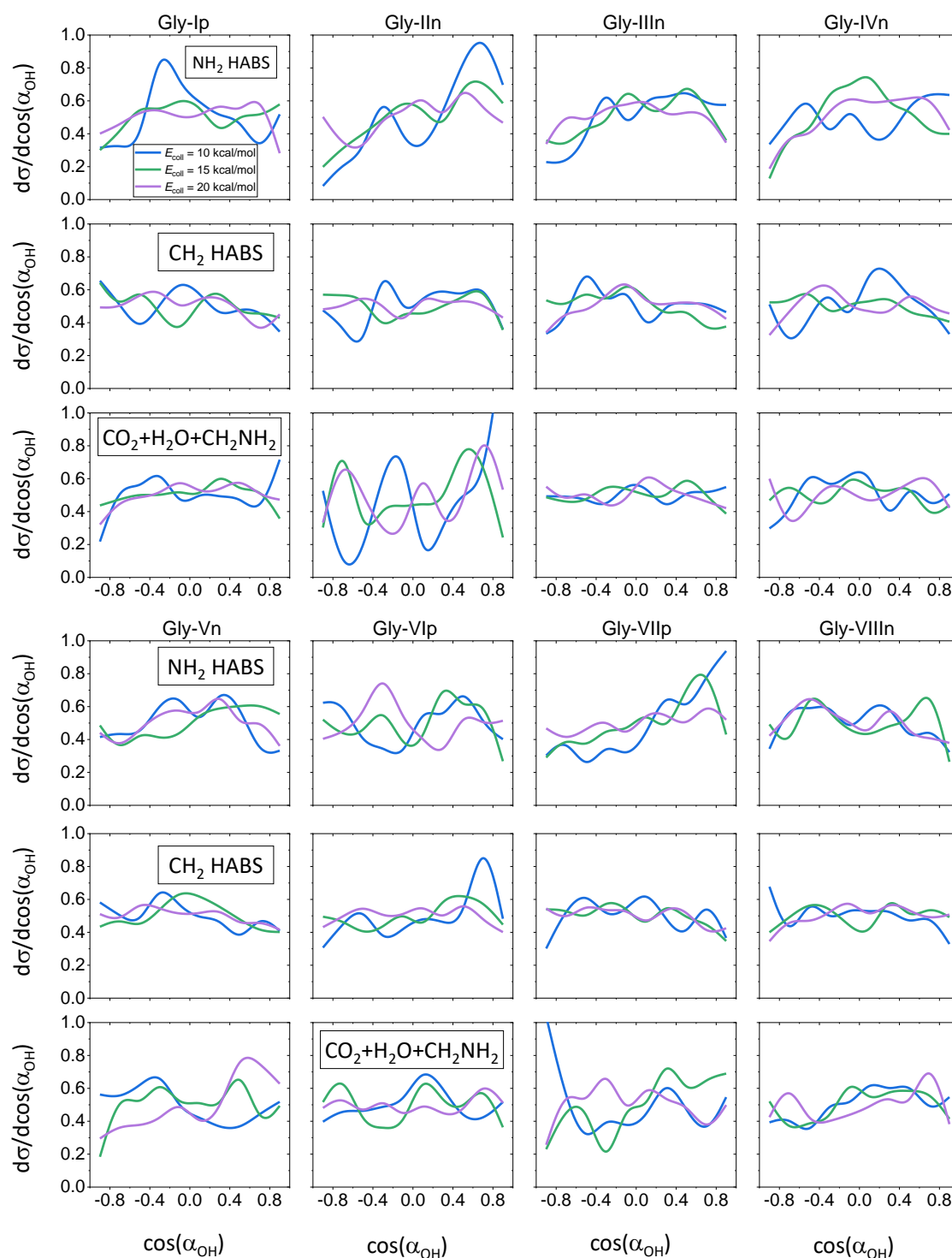
Figure 43. Normalized initial attack angle distributions for the reactant OH in the OH + glycine H-abstraction reaction at collision energies of 10, 15 and 20 kcal/mol.

Figure 44 shows the initial attack angle distributions for the reactant glycine at various collision energies. When $\cos(\alpha) = -1$, the glycine molecule approaches the OH radical with its amino group first, while $\cos(\alpha) = 1$ indicates that the carboxyl group of

glycine is directed toward the OH radical. For NH_2 H-abstraction, it is observed that the glycine molecule approaches the OH radical with its amino group for conformers IIn, Vn and VIIp, which is expected since the hydrogen is abstracted from that site in this type of reaction. Notably, when the trajectories start from the IVn reactant conformer, there is a slight preference for the glycine molecule to approach the OH radical with its carboxyl group at all collision energies. This tendency is also observed for the VIp conformer at collision energy of 10 kcal/mol. For the H-abstraction occurring at the CH_2 group, we would expect an attack angle of around 90° indicating that the glycine molecule approaches the OH radical from the CH_2 group side. However, the distributions show that an approach from the amino group is clearly more preferred for all reactant conformers. This might be explained by two factors. Firstly, the H-bond formed with the nitrogen atom is weaker than the one formed with oxygen, which allows the OH radical to more easily transition from the nitrogen to the CH_2 group of the glycine molecule where the abstraction reaction occurs. Secondly, examining the one-dimensional potential energy curves for the entrance channel made with the Ip reactant conformer reveals that in two cases, no energy minimum is observed. In one case, the OH approaches the amino-N with its O atom and in the other case, the OH approaches the carboxyl-O of the glycine molecule with its oxygen atom. In both scenarios, repulsion occurs between the two molecules, but in the case of the amino group orientation, the OH radical can more readily move to the CH_2 group of the glycine molecule. For H-abstraction at the carboxyl group, the distributions for the Ip, IIIn, IVn, and Vn reactant conformers show that the glycine molecule preferentially approaches the OH radical from the carboxyl group side, which is expected as this is where the reaction takes place. Additionally, for the IIn, VIp, VIIp and VIIIn reactant conformers, there is a slight preference for attack from the NH_2 group. The understanding of this phenomenon is facilitated by **Figure 45.** Based on the mechanisms, we can divide the four conformers into two groups. The first group includes the VIp and VIIIn conformers. The reactions of these glycine conformers are characterized by the glycine molecule initially adopting an orientation in which the NH_2 group is closer to the hydroxyl radical in absolute terms. However, due to the position of the CH_2 group and the relatively distant location of the NH_2 group, the OH molecule will not reach any of the amino Hs upon collision. Once the OH radical comes sufficiently close to the carboxyl-OH group of the glycine molecule, H-

abstraction occurs and the dehydrogenated glycine molecule breaks into CO_2 and CH_2NH_2 fragments.
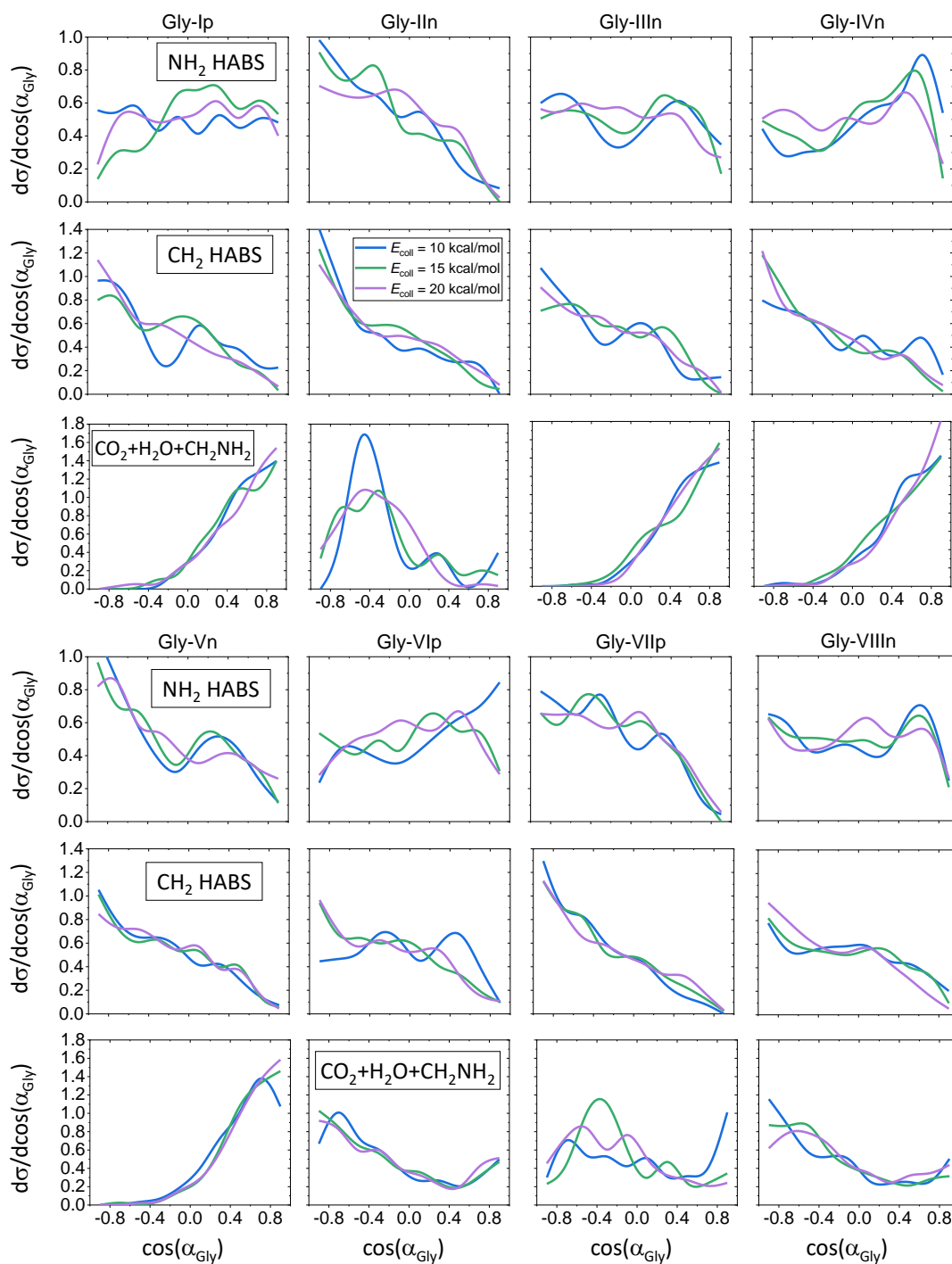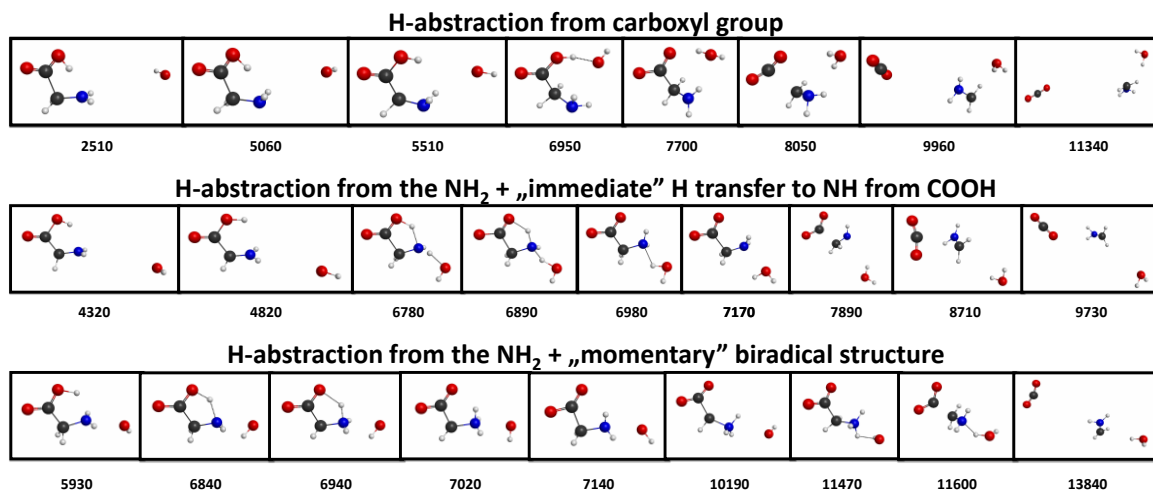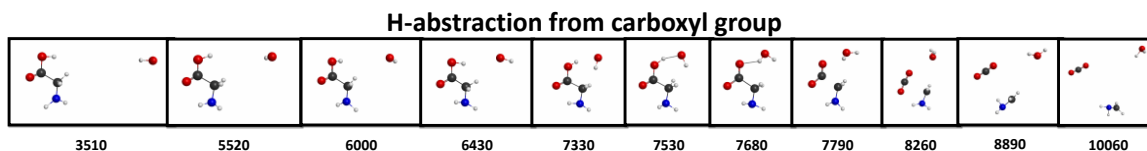

Figure 44. Normalized initial attack angle distributions for the reactant glycine in the OH + glycine H-abstraction reaction at collision energies of 10, 15 and 20 kcal/mol.
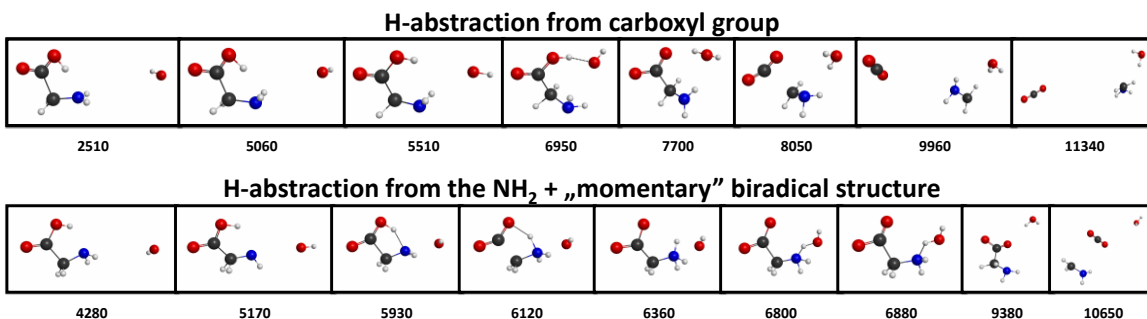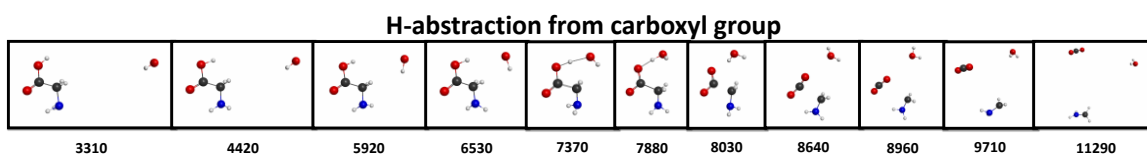
Gly-IIn

H-abstraction from carboxyl group

| 2510 | 5060 | 5510 | 6950 | 7700 | 8050 | 9960 | 11340 |

H-abstraction from the NH$_2$ + „immediate" H transfer to NH from COOH

| 4320 | 4820 | 6780 | 6890 | 6980 | 7170 | 7890 | 8710 | 9730 |

H-abstraction from the NH$_2$ + „momentary" biradical structure

| 5930 | 6840 | 6940 | 7020 | 7140 | 10190 | 11470 | 11600 | 13840 |

Gly-VIp

H-abstraction from carboxyl group

| 3510 | 5520 | 6000 | 6430 | 7330 | 7530 | 7680 | 7790 | 8260 | 8890 | 10060 |

Gly-VIIp

H-abstraction from carboxyl group

| 2510 | 5060 | 5510 | 6950 | 7700 | 8050 | 9960 | 11340 |

H-abstraction from the NH$_2$ + „momentary" biradical structure

| 4280 | 5170 | 5930 | 6120 | 6360 | 6800 | 6880 | 9380 | 10650 |

Gly-VIIIn

H-abstraction from carboxyl group

| 3310 | 4420 | 5920 | 6530 | 7370 | 7880 | 8030 | 8640 | 8960 | 9710 | 11290 |

Time step

Figure 45. The reaction mechanisms of H-abstractions from the IIn, VIp, VIIp and VIIIn glycine conformers occurring at the carboxyl-OH when the glycine molecule approaches the OH radical with its amino group facing it. One time step is 0.0726 fs.

The reactions of the IIn and VIIp glycine conformers can be classified into a separate group because, aside from the simple abstraction of the carboxyl-H by OH, another mechanism is also observed. In this mechanism, H-abstraction actually occurs on the amino group, while the carboxyl-H shifts to N, ultimately resulting in the dehydrogenation of the carboxyl group and the formation of a biradical structure. It is worth mentioning that without additional electronic structure analysis, it is hard to decide that the resulting structure is biradical or zwitterionic. However, given that OH abstracts a H atom from the glycine molecule during the reaction, it can be assumed that a biradical structure is formed. Moreover, in the case of the IIn conformer, a mechanism is illustrated in the second row of **Figure 45** where the H-transfer from the carboxyl group to N and the H-abstraction from the amino group occur simultaneously.

4 SUMMARY

4.1 OH + C$_2$H$_6$

In case of the OH + C$_2$H$_6$ reaction, the transition states and minima are investigated for the H-abstraction, H-substitution and methyl-substitution pathways on the potential energy surface where the substitution reaction channels are characterized for the first time in the present work. Additionally, two mechanisms are considered for the substitution pathways: Walden inversion and front-side attack. In addition to H-abstraction, methyl-substitution is also found to be exothermic, while H-substitution is thermodynamically hindered as the energy of the products is 9.10(7.12) kcal/mol higher than that of the reactants in a classical(adiabatic) sense. The classical(adiabatic) energy barrier for H-abstraction is 3.69(2.18) kcal/mol. Among the transition states for substitution reactions, the Walden-inversion methyl-substitution transition state has the lowest barrier. However, it still has a classical(adiabatic) relative energy of 39.89(39.60) kcal/mol indicating that substitution reactions are kinetically significantly hindered. In the case of H-substitution, the energy barrier associated with the Walden-inversion pathway is lower than that of the front-side mechanism. The difference between the energy of the transition states is 10.81(10.75) kcal/mol classically(adiabatically). For methyl-substitution, stationary points corresponding to the front-side mechanism could not be found. It is possible that such points do not exist for methyl-substitution and the reaction may only proceed through Walden inversion. Among the product channel minima, the H-abstraction has the lowest energy followed by the methyl substitution. Interestingly, for H-substitution the post-reaction complex with the front-side mechanism has lower energy than the Walden-inversion complex, although the difference is minimal being only 0.06(0.01) kcal/mol classically(adiabatically). Additionally, to understand the energetics of the entrance channel, one-dimensional potential energy curves are constructed at three different orientations of the reactants. In these scans, the reactants are fixed in their equilibrium structures and approach each other along a single intermolecular coordinate. Spin-orbit computations are performed for the entrance channel revealing van der Waals wells with depths of 0.5 to 0.8 kcal/mol depending on the relative orientation of the reactants. Examining the geometric parameters of the transition states reveals that the Hammond

postulate is valid for all three reaction channels. Once the stationary points are characterized, a global, analytical, full-dimensional potential energy surface is developed to enable an extensive understanding of the dynamics. The developed PES has an RMS error below 1 kcal/mol in the chemically relevant region. Furthermore, test simulations at collision energies of 1, 10, 20, 30, 40 and 50 kcal/mol revealed that fewer than 3% of the trajectories produced physically unrealistic products. To study the reaction in its vibrational ground state a total of 85 000 QCT simulations are run within the collision energy range of 10-50 kcal/mol. Based on the simulations performed, it can be stated that within the mentioned collision energy range, substitution products are virtually not formed. Therefore, we focused on studying the dynamics of the H-abstraction reaction in greater detail. It can be stated that the cross sections for the H-abstraction increase as the collision energy increases. To eliminate zero-point energy violations soft and hard constraints are used for the vibrational energy of the products. The soft constraint has little impact on the cross sections, whereas with the hard constraint the ICS values are reduced to about half compared to the case with no constraints applied. Additionally, the maximum impact parameters exhibit minimal dependence on collision energy. However, as the collision energy increases the shape of the opacity functions changes showing a preference for larger impact parameters. This pattern is also reflected in the scattering angle distributions, which shift from backward to forward dominance with increasing collision energy. These observations suggest that at lower collision energies the reaction mainly proceeds via a direct rebound pathway, while at higher collision energies the direct stripping mechanism becomes more favoured. Examining the initial attack angle distributions reveals that for the OH radical a side-on attack is clearly preferred, whereas for C_2H_6, there is no distinct orientation that the molecule adopts at the beginning of the reaction. The initial attack angle distributions obtained for the OH radical may seem surprising at first as one might expect that for H-abstraction the preferred pathway would have the OH radical approaching the C_2H_6 molecule with the O atom. However, upon examining the structure of the H-abstraction transition state, where the H-O-H bond angle is approximately 90°, the results become understandable. The initial attack angle distributions for C_2H_6 are as expected, since each hydrogen atom in the molecule is equivalent. Product relative translational energy distributions indicate effective energy transfer between the reactant and product translational modes. The product internal energy distributions exhibit only a

modest dependence on collision energy. Moreover, it can be observed that the vibrational energy distributions of both product molecules show less dependence on collision energy than the internal energy distributions reflecting the nearly constant effect of the hard ZPE constraint. For the rotational energy distributions, it is apparent that with increasing collision energy the distributions shift to higher rotational energies. The zero-point energy violation is greater in the case of the C_2H_5 molecule. Based on the distributions of rotational quantum numbers (J), it can be observed that as the collision energy increases the distributions shift towards higher J excitations. For H_2O, the J values range from 0 to 30, while for C_2H_5, the J values range from 0 to 120 indicating that significantly higher excitations are possible for C_2H_5. This can be attributed to the larger moments of inertia of C_2H_5. After the investigation of the dynamics of the ground-state reaction, we also study the impact of vibrational excitation of the reactants for the H-abstraction reaction. Six different normal mode excitations (CC stretching, CH_3 deformation and symmetric/asymmetric/degenerate CH stretching for C_2H_6 and OH stretching for OH) are investigated with 85 000 trajectories being run for each mode. Thus, the impact of vibrational excitation is analyzed through 510 000 simulations. The cross sections reveal that the vibrational excitation of the CH stretching significantly increases, while the vibrational excitation of the CC stretching reduces and the vibrational excitation of the OH bond does not affect reactivity. Comparing the effects of collision energy and vibrational excitations based on the non- and soft-constrained trajectories reveals that as expected from chemical intuition the OH and CC stretching modes are less effective in activating the reaction than translational energy. However, CH stretching excitations have similar or even slightly greater effects on reactivity compared to translational energy, which contradicts the Polanyi rules. There is no significant mode specificity observed in the angular and translational energy distributions and the distributions in case of the different vibrational extations shift similarly to the ground-state reaction as the collision energy increases. The initial OH excitation energy primarily stays within the H_2O product vibration, while the vibrational energy from the ethane modes transfers to the C_2H_5 product, even for the reactive CH stretching modes. However, the rotational distributions remain unaffected by the vibrational states of the reactants. The mode-specific vibrational distributions of H_2O indicate that for bending and asymmetric stretching the ground state is predominant. In the case of symmetric stretching at the lowest collision energy the ground and first-excited

states are nearly equally populated. However, as the collision energy increases the ground state becomes increasingly favored. Moreover, the initial vibrational extation of the OH stretching mode excites the asymmetric stretching mode of the H_2O product. As the vibrational quantum number increases the population of the bending mode decreases, which is in nearly complete agreement with experimental data. For the stretching modes, experiments only measured cumulative populations, which are higher than those predicted by the current simulations. Nevertheless, both theoretical and experimental findings indicate that H_2O stretching modes are typically excited by at least one quantum consistent with the expected behavior for the early-barrier H-abstraction.

4.2 $OH + CH_3NH_2$

For the $OH + CH_3NH_2$ reaction, minima and saddle points on the potential energy surface are identified distinguishing six different product channels. This work represents a novel contribution to the literature, in which stationary points for substitution channels are also uncovered. Since the CH_3NH_2 molecule contains both a methyl group and an amino group, both H-abstraction and substitution reactions can occur at these two different parts of the molecule. Two types of mechanisms are considered for substitution reactions: Walden inversion and front-side attack. The following reaction channels are distinguished: H-abstraction from the CH_3 group, H-abstraction from the NH_2 group, Walden mechanism H-substitution at the CH_3 group, Walden mechanism H-substitution at the NH_2 group, front-side H-substitution at the CH_3 group, Walden mechanism methyl substitution, Walden mechanism amino substitution and front-side mechanism amino substitution. Based on the constructed schematic potential energy surface, it can be stated that apart from the two H-abstraction reactions, amino substitution is thermodynamically favoured, whereas the products of H-substitution reactions and methyl substitution possess higher energy compared to the reactants indicating that these are endothermic processes. According to the relative classical energies, the H-abstraction reactions occur without an energy barrier. However, when considering the adiabatic energies, the transition-state energy for H-abstraction at the CH_3 group slightly exceeds that of the reactants by 0.13 kcal/mol. The other reaction channels have significant energy barriers making them kinetically hindered. Among them, the reaction with the lowest-energy barrier is the front-side mechanism H-

substitution at the CH_3 group, which has a classical(adiabatic) value of 7.34(4.67) kcal/mol. Interestingly, the Walden-inversion mechanism always has a higher energy barrier compared to the front-side mechanism. This can be explained by the stabilizing intermolecular interactions present in the front-side transition-state structures. In the case of complexes identified in the exit channel, the H-abstraction minima have the lowest energy. Specifically, if the H abstraction occurs at the methyl group, the post-reaction complex has a relative classical(adiabatic) energy of −30.37(−29.14) kcal/mol, whereas if the reaction takes place on the amino group, the post-reaction complex has a slightly higher relative classical(adiabatic) energy of −24.39(−24.20) kcal/mol. Among the other reactions, the amino-substitution reactions considering both mechanisms also exhibit energies that are lower than those of the reactants. The energy of the post-reaction complexes for the other reaction pathways exceeds that of the reactants and differs from the energies of the products in the given product channels by less than 1 kcal/mol. The entrance channel is studied by plotting one-dimensional potential energy curves taking into account 11 different orientations of the reactants. When the OH approaches the CH_3NH_2 molecule with its O atom near the N atom and perpendicular to the C-N bond no minimum is observed. However, when the OH radical approaches in the same orientation but with its hydrogen atom the deepest minimum, approximately 9 kcal/mol, is detected. For other orientations, the observed minima are no deeper than 2 kcal/mol. Additionally, the conformers of the given stationary points are also sought for the transition states, post-reaction complexes and products. In the case of H-abstraction, if it happens on the amino group three distinct transition state structures can be identified, whereas if it occurs on the methyl group five different transition state structures can be distinguished. For the two H-substitution reaction channels and the front-side mechanism amino substitution 2-2-2 transition state conformers are uncovered. In other scenarios, only a single conformer is identified. In the exit channel, except for the H-abstraction occurring on the amino group, two different structures of the post-reaction complexes are observed for each reaction. For the products, the cis and trans isomers of the NH_2OH molecule are identified as well as two conformers of the CH_3NHOH molecule. Finally, rate coefficients are determined for H-abstraction based on transition-state theory. The rate coefficients with the Wigner tunneling correction calculated by us show good agreement with the experimental values.

4.3 OH + GLYCINE: H-ABSTRACTION

The saddle-points and post-reaction minima are obtained on the potential energy surface of the OH + glycine reaction using high-level *ab initio* computations considering three different pathways: CH_2-, NH_2- and COOH-H abstractions. To identify the maximum number of conformers for the transition states and post-reaction complexes a systematic mapping is performed across three different theoretical levels. Geometry optimizations and frequency computations are carried out using the MP2 method with the 3-21G basis starting from 1296 initial structures generated by internal rotations based on the stationary points identified through chemical intuition. Next, the structures obtained at the MP2/3-21G level are used for geometry optimizations and frequency computations at the MP2/aug-cc-pVDZ level. Subsequently, these optimized structures are further refined at the CCSD(T)-F12b/aug-cc-pVDZ level of theory. As a result of the systematic search at the highest quantum chemical level 5, 5 and 5 transition states and 2, 19 and 0 post-reaction complexes are identified for the CH_2-, NH_2- and COOH-H-abstraction reaction pathways, respectively. Benchmark relative energies for the transition states and post-reaction minimum conformers are obtained using a high-level composite approach. This approach utilizes the CCSD(T)-F12b/aug-cc-pVQZ level of theory and includes corrections for post-(T) correlation, core correlation, scalar relativity, spin-orbit effects and zero-point energy. The energies of the products are lower than those of the reactants in the case of every reaction channel. The most exothermic reaction is the H-abstraction from the CH_2 group followed by the H-abstraction from the NH_2 group and then the H-abstraction from the COOH group in increasing energy order. Although the H-abstraction occurring at the COOH group has a low classical energy barrier of 1.02 kcal/mol, when zero-point energy corrections are added to the classical values, it is observed that all three reactions are barrierless. Additionally, the transition-state energy for the reaction at the NH_2 group is lower than that for the CH_2 group, but the opposite trend is observed for the post-reaction complexes. For the entrance channel, one-dimensional scans are performed in seven distinct orientations of the reactants. The scans show that when the OH radical approaches with its O atom directed towards the carbonyl-O or towards the N of the amino group a repulsive interaction occurs between the two molecules. In the other five orientations, significant minima are observed in the energy curves. After mapping the stationary points of the

reaction, a full-dimensional, analytical potential energy surface is developed using a composite coupled-cluster method to compute the energy points. The fitting error of the final PES in the chemically relevant region is 2.82 kcal/mol. Based on dynamics test simulations run at collision energies of 1, 10, 20 and 30 kcal/mol the proportion of unphysical trajectories is reduced to below 3%. The dynamics of the reaction is studied using a total of 504 000 quasi-classical trajectories with 63 000 simulations run for each glycine conformer. The simulations reveal that H-abstraction from the carboxyl group of the glycine molecule does not always lead to the formation of H_2O and NH_2CH_2COO products. Instead, it can result in the decomposition of the dehydrogenated glycine molecule into CO_2 and CH_2NH_2. Furthermore, the cross sections clearly show that this occurs in nearly 100% of the cases. At low collision energies, the three-fragment product channel of the carboxyl group is the most reactive and as the collision energy increases the reactions involving the CH_2 and NH_2 groups become more significant. The scattering angle distributions for H-abstraction reactions occurring at both the CH_2 and NH_2 groups generally show an isotropic distribution for most glycine conformers with some cases exhibiting forward scattering. According to the initial attack angle distributions for the OH radical, the distribution is generally isotropic for most glycine conformers regardless of the group where H-abstraction occurs. In some cases, the OH radical prefers to approach the glycine molecule with its H atom. This finding that attack with the oxygen atom is less preferred can be explained by the repulsive interactions between the O atom of the OH radical and the N or O atoms of the glycine molecule due to non-bonding electron pairs. In contrast, when the OH radical approaches with its H atom, H-bonds can form between the two molecules. After this interaction, the OH radical can still adopt a reactive orientation allowing the H-abstraction to occur. According to the initial attack angle distributions determined for the glycine molecule, when H-abstraction occurs at the CH_2 group, attack with the amino group is clearly preferred for all reactant conformers. This phenomenon may be explained by the stronger H-bond with the carbonyl-O compared to the amino-N. Consequently, the OH radical is more likely to approach the CH_2 group from the NH_2 group. During H-abstraction at the NH_2 group, we expect the glycine molecule to approach the OH radical with its amino group. This is clearly observed for the IIn, Vn, and VIIp glycine conformers. For the other reactant conformers, it can be established that there is no specific orientation in which the glycine molecule preferentially approaches the OH radical.

Additionally, it is evident that a frontal attack on the carboxyl group is not preferred at all. In the case of H-abstraction at the carboxyl group, we expect the glycine molecule to attack from the carboxyl group side. This type of initial attack angle distribution is observed for the Ip, IIIn, IVn, and Vn glycine conformers. For the IIn, VIp, VIIp and VIIIn reactant conformers, there is a minor preference for the glycine molecule to attack with the NH_2 group. In the case of the VIp and VIIIn glycine conformers, this tendency can be interpreted as follows: although the amino group of the glycine molecule is closer to the attacking OH along the horizontal axis, during the collision, the OH actually comes closer to the carboxyl group. Additionally, the CH_2 group acts as a kind of protective shield over the NH_2 group making it difficult for the hydroxyl radical to approach the amino group. In the case of the IIn and VIIp glycine conformers, in addition to the reaction where the OH radical simply abstracts the H from the carboxyl group during collision, despite also coming close to the amino group, the reaction can also proceed in a way that a biradical structure is formed. In this case, the carboxyl-H shifts to the N atom, and the H-abstraction occurs not at the carboxyl group, but at the amino group. Furthermore, it can be concluded that the appearance of the biradical form is related to the orientation of the carboxyl group in the reactant glycine molecule. H-transfer from the carboxyl group to the N atom is only observed when the carboxyl-H is closer to the amino group in the glycine molecule.

4.4 OUTLOOK AND PERSPECTIVES

In summary, during my doctoral research, I mapped the stationary points on the potential energy surfaces of three different reactions using highly accurate *ab initio* methods. These results not only serve as benchmarks in the current literature but uncover new reaction pathways and may lay the groundwork for future PES developments, as demonstrated in my work on the OH + C_2H_6 and OH + glycine reactions, which open up possibilities for a deeper understanding of reaction dynamics. In my work, I applied the QCT method; however, reactions can be simulated more accurately using full quantum dynamics. Unfortunately, due to their high computational cost, these calculations are currently feasible only for very small systems (5-6 atoms). Furthermore, potential energy surfaces not only allow for the study of ground-state reactions but also enable the investigation of the effects of vibrational excitation, which I carried out in my research on

the OH + C_2H_6 reaction. Beyond studying vibrational mode specificity, another potential future direction is exploring how rotational excitation of reactants affects reactivity and the reaction mechanisms. Finally, reactions could also be worth investigating in the liquid phase in the future, using different solvent models, with particular focus on the OH + glycine reaction. Its study could be important from a biological perspective, as OH radicals, released in the human body due to UV radiation, can damage biomolecules, and one of the simplest of which is glycine.

5 ÖSSZEFOGLALÁS

5.1 OH + C₂H₆

Az OH + C_2H_6 reakció esetén a doktori munkámban a H-absztrakciós, H-szubsztitúciós és metil-szubsztitúciós útvonalak átmeneti állapotainak és minimumainak azonosítását és jellemzését tűztük ki célul. Szubsztitúciós útvonalak esetén kétféle mechanizmust különböztettünk meg: Walden inverziót és elölről támadást. Eredményeink alapján megállapítható, hogy a H-absztrakció mellett a metil-szubsztitúció is exoterm, míg a H-szubsztitúció termodinamikailag gátolt, mivel a termékek energiája 9,10(7,12) kcal/mol-lal magasabb klasszikusan(adiabatikusan), mint a reaktánsoké. A H-absztrakció klasszikus(adiabatikus) energiagátja 3,69(2,18) kcal/mol. A szubsztitúciós reakciók átmeneti állapotai közül a Walden-inverziós metil-szubsztitúciós átmeneti állapot rendelkezik a legalacsonyabb gáttal, melynek értéke klasszikusan(adiabatikusan) 39,89(39,60) kcal/mol, ami azt jelzi, hogy a szubsztitúciós reakciók kinetikailag jelentősen gátoltak. H-szubsztitúció esetén a Walden-inverziós útvonalhoz tartozó energiagát alacsonyabb, mint az elölről támadásos mechanizmusé. Az átmeneti állapotok energiái közötti különbség klasszikusan(adiabatikusan) 10,81(10,75) kcal/mol. A metil-szubsztitúció esetén az elölről támadásos mechanizmushoz tartozó stacionárius pontokat nem találtunk, viszont lehetséges, hogy ezen stacionárius pontok nem léteznek a metil-szubsztitúció esetén és a reakció csak Walden-inverzión keresztül mehet végbe. A legalacsonyabb energiájú termékcsatornabeli minimum a H-absztrakcióhoz tartozik, melyet a metil-szubsztitúciós követ. Érdekes módon az elölről támadásos H-szubsztitúciós termékcsatornabeli komplex alacsonyabb energiájú, mint a Walden-inverziós, bár a különbség minimális, klasszikusan(adiabatikusan) mindössze 0,06(0,01) kcal/mol. A bemeneti csatornát egydimenziós potenciális energiagörbék segítségével vizsgáltuk a reaktánsok három különböző orientációjában. Az ezekhez szükséges számítások esetén a reaktánsokat befagyasztottuk az egyensúlyi szerkezetükben és egyetlen intermolekuláris koordináta mentén közelítettük őket egymáshoz. Továbbá spin-pálya számításokat végeztünk a bemeneti csatornára vonatkozóan, ahol a reaktánsok relatív orientációjától függően 0,5-0,8 kcal/mol mélységű van der Waals-völgyek jelentek meg. Az átmeneti állapotok geometriai paramétereit szemügyre véve kiderül, hogy a Hammond-posztulátum

mindhárom reakciócsatorna esetén érvényes. A stacionárius pontok jellemzése után egy globális, analitikus, teljes dimenziós potenciálisenergia-felületet fejlesztettünk, amely lehetővé tette a dinamika széles körű megértését. A kifejlesztett PES RMS hibája 1 kcal/mol alatt van a kémiailag releváns régióban. Ezenkívül az 1, 10, 20, 30, 40 és 50 kcal/mol ütközési energiáknál végzett tesztszimulációk azt mutatták, hogy a trajektóriák kevesebb mint 3%-a eredményezett fizikailag irreális termékeket. A rezgési alapállapotú reakció vizsgálatához összesen 85 000 QCT szimulációt futtattunk a 10-50 kcal/mol-os ütközési energia tartományban. Az elvégzett szimulációk alapján megállapítható, hogy az említett ütközési energia tartományon belül gyakorlatilag nem képződnek szubsztitúciós termékek, így a továbbiakban a H-absztrakciós reakcióút dinamikájának részletesebb tanulmányozására összpontosítottunk. Megállapítható, hogy a H-absztrakció integrális hatáskeresztmetszet értékei az ütközési energia növekedésével nőnek. A zérusponti energiasértések kiküszöbölésére "lágy" és "kemény" megszorításokat alkalmaztunk a termékek rezgési energiájára vonatkozóan. A "lágy" megszorítás csekély hatással van a hatáskeresztmetszetekre, míg a kemény megszorítással az ICS-értékek körülbelül a felére csökkennek a megszorítás nélküli esethez képest. Továbbá megállapítható, hogy a maximális ütközési paraméterek minimális függést mutatnak az ütközési energiától. Azonban, ahogy az ütközési energia növekszik, az opacitás függvények alakja megváltozik, jelezve a nagyobb ütközési paraméterek előtérbe kerülését. Ez a trend tükröződik a szórási szögeloszlásokban is, amelyek alapján megállapítható, hogy az ütközési energia növekedésével az előreszórás kerül egyre inkább előtérbe a hátraszórással szemben. Ezek a megfigyelések arra utalnak, hogy kisebb ütközési energiáknál a reakció főként direkt visszapattanásos mechanizmussal megy végbe, míg nagyobb ütközési energiáknál a direkt lehasításos mechanizmus válik dominánsabbá. A kezdeti támadási szögeloszlások megmutatták, hogy az OH gyök esetében egyértelműen az oldalirányú támadás a domináns, míg a C_2H_6 esetében nincs egyértelmű orientáció, amelyet felvenne a molekula a reakció elején. Az OH gyöknél kapott kezdeti támadási szögeloszlások elsőre meglepőnek tűnhetnek, mivel azt várhatnánk, hogy a H-absztrakció esetében az előnyben részesített útvonal az, amikor az OH gyök az O felől közelíti meg a C_2H_6 molekulát. Azonban a H-absztrakciós átmeneti állapot szerkezetét megfigyelve érthetővé válnak az eredmények, ahol a H-O-H kötésszög körülbelül 90°. A C_2H_6 kezdeti támadási szögeloszlása a vártnak megfelelő, mivel a molekulában minden hidrogénatom egyenértékű. A termékek relatív

transzlációs energiaeloszlása hatékony energiaátvitelt mutat a reaktáns és a termék transzlációs módusai között. A termékek belső energiaeloszlása csak kis mértékben függ az ütközési energiától. Megfigyelhető továbbá, hogy mindkét termékmolekula rezgési energiaeloszlása kisebb mértékben függ az ütközési energiától, mint a belső energiaeloszlások, ami a "kemény" ZPE megszorítás közel állandó hatását tükrözi. A forgási energiaeloszlások esetében nyilvánvaló, hogy az ütközési energia növekedésével az eloszlások a nagyobb forgási energiák felé tolódnak el. A zérusponti energiasértés nagyobb a C_2H_5 molekula esetében. A forgási kvantumszámok (J) eloszlása alapján megfigyelhető, hogy az ütközési energia növekedésével az eloszlások a nagyobb J gerjesztések felé tolódnak el. A H_2O esetében a J értékek 0 és 30 között, míg a C_2H_5 esetében a J értékek 0 és 120 között mozognak, ami azt jelzi, hogy a C_2H_5 esetében lényegesen nagyobb gerjesztés lehetséges. Ez a C_2H_5 nagyobb tehetetlenségi nyomatékának tudható be. Az alapállapotú reakció dinamikájának vizsgálata után a reaktánsok rezgési gerjesztésének hatását is vizsgáltuk a H-absztrakciós reakció esetén. Hat különböző normál módus gerjesztését (CC nyújtás, CH_3 deformáció és szimmetrikus/aszimmetrikus/degenerált CH nyújtás C_2H_6 esetén és OH nyújtás OH esetén) vizsgáltuk 85 000 trajektória futtatásával minden módus esetén. Így összesen a rezgési gerjesztés hatását 510 000 szimuláción keresztül elemeztük. Az integrális hatáskeresztmetszetek megmutatták, hogy a CH nyújtás rezgési gerjesztése jelentősen növeli, a CC nyújtás rezgési gerjesztése csökkenti, míg az OH kötés rezgési gerjesztése nem befolyásolja a reakcióképességet. Összehasonlítva az ütközési energia és a rezgési gerjesztés hatását a nem- és "lágy"-megszorításos trajektóriák alapján kiderül, hogy az OH és CC nyújtási módusok kevésbé hatékonyak a reakció aktiválásában, mint a transzlációs energia. A CH nyújtási gerjesztések azonban hasonló, vagy valamivel nagyobb hatást gyakorolnak a reaktivitásra a transzlációs energiához képest, ami ellentmond a Polanyi-szabályoknak. A szög- és transzlációs energiaeloszlásban nem figyelhető meg szignifikáns módspecifikusság, valamint az ütközési energia növekedésével az eloszlások a különböző rezgési gerjesztések esetén az alapállapotú reakcióhoz hasonlóan tolódnak el. A kezdeti OH gerjesztési energia elsősorban a H_2O termékrezgésen belül marad, míg az etán módusokból származó rezgési energia átkerül a C_2H_5 molekulába. A forgási eloszlást nem befolyásolja a reaktánsok rezgési gerjesztése. A H_2O módspecifikus rezgési energiaeloszlása alapján elmondható, hogy hajlításnál és aszimmetrikus nyújtásnál az alapállapot betöltöttsége a domináns. Szimmetrikus nyújtás esetén a legalacsonyabb ütközési

energiánál az alap és az egyszeresen gerjesztett állapotok közel azonos mértékben vannak betöltve. Azonban ahogy az ütközési energia növekszik, az alapállapot egyre előnyösebbé válik. Továbbá, az OH nyújtás kezdeti rezgési gerjesztése a termék H_2O aszimmetrikus nyújtási módusát gerjeszti. A rezgési kvantumszám növekedésével a hajlítási mód populációja csökken, ami majdnem teljes összhangban van a kísérleti adatokkal. A nyújtási módusok esetében a kísérletek csak kumulatív populációkat mértek, amelyek magasabbak a jelenlegi szimulációk által előre jelzettnél. Mindazonáltal mind az elméleti, mind a kísérleti eredmények azt mutatják, hogy a H_2O nyújtási módusok általában legalább egy kvantummal gerjesztődnek, amely összhangban van azzal, hogy a H-absztrakció korai gáttal rendelkezik.

5.2 OH + CH₃NH₂

Az OH + CH₃NH₂ reakció esetén a minimumokat és nyeregpontokat azonosítottuk a potenciálisenergia-felületen hat különböző termékcsatornát megkülönböztetve. Megjegyezném, hogy a szubsztitúciós reakciókhoz tartozó stacionárius pontokat a szakirodalomban először ez a munka tárta fel. Mivel a CH₃NH₂ molekula metilcsoportot és aminocsoportot is tartalmaz, a molekula ezen két különböző részén mind a H-absztrakció, mind a szubsztitúciós reakciók végbemehetnek. A szubsztitúciós reakciók esetén kétféle mechanizmust vettünk figyelembe: Walden inverziót és elölről támadást. A következő reakciócsatornákat különböztettük meg: H-absztrakciót a CH₃-csoportról, H-absztrakciót az NH₂-csoportról, Walden-mechanizmusú H-szubsztitúciót a CH₃-csoportnál, Walden-mechanizmusú H-szubsztitúciót az NH₂-csoportnál, elölről támadásos H-szubsztitúciót a CH₃ csoportnál, Walden-mechanizmusú metil-szubsztitúciót, Walden-mechanizmusú amino-szubsztitúciót és elölről támadásos mechanizmusú amino-szubsztitúciót. Az elkészített sematikus potenciálisenergia-felület alapján megállapítható, hogy a két H-absztrakciós reakción kívül az aminoszubsztitúció termodinamikailag kedvező, míg a H-szubsztitúciós reakciók és a metilszubsztitúció termékei nagyobb energiával rendelkeznek a reaktánsokhoz képest, ami azt jelzi, hogy ezek endoterm folyamatok. A relatív klasszikus energiák alapján a H-absztrakciós reakciók energiagát nélkül mennek végbe. Az adiabatikus energiákat figyelembe véve azonban a CH₃-H-absztrakció átmeneti állapotának energiája 0,13 kcal/mol-lal meghaladja a reaktánsokét. A többi reakciócsatorna jelentős

energiagáttal rendelkezik, ami kinetikailag gátolttá teszi őket. Közülük a legalacsonyabb energiagáttal rendelkező reakció a CH_3 csoportnál végbemenő elölről támadásos mechanizmusú H-szubsztitúció, melynek klasszikus(adiabatikus) értéke 7,34(4,67) kcal/mol. Érdekes módon a Walden-inverziós mechanizmus mindig magasabb energiagáttal rendelkezik, mint az elölről támadásos mechanizmus. Ez a jelenség az elölről támadásos mechanizmusú átmeneti állapot szerkezetében jelenlévő stabilizáló intermolekuláris kölcsönhatásokkal magyarázható. A termékcsatornabeli komplexek esetében a H-absztrakciós minimumok energiája a legalacsonyabb. Pontosabban, ha a H-absztrakció a metilcsoporton történik, akkor a termékcsatornabeli komplex relatív klasszikus(adiabatikus) energiája −30,37(−29,14) kcal/mol, míg ha a reakció az aminocsoporton megy végbe, akkor a termékcsatornabeli komplex relatív klasszikus(adiabatikus) energiája valamivel magasabb, melynek értéke −24,39(−24,20) kcal/mol. A többi reakció között az amino-szubsztitúciós reakciók mindkét mechanizmust figyelembe véve szintén kisebb energiával rendelkeznek, mint a reaktánsok. A termékcsatornabeli komplexek energiája a többi reakcióútra nézve meghaladja a reaktánsokét, és kevesebb, mint 1 kcal/mol-al tér el az adott termékcsatornákban lévő termékek energiáitól. A bemeneti csatornát egydimenziós potenciális energiagörbék segítségével vizsgáltuk, amely során a reaktánsoknak 11 különböző orientációját vettük figyelembe. Amikor az OH az O atomjával közelíti meg a CH_3NH_2 molekulát az N atom közelében merőlegesen a C-N kötésre, akkor nem figyelhető meg minimum. Ha azonban az OH gyök ugyanebben az orientációban, de a H atomjával közelít, a legmélyebb minimumot figyelhetjük meg, melynek nagysága körülbelül 9 kcal/mol. Más orientációk esetén a megfigyelt minimumok nem mélyebbek 2 kcal/mol-nál. Továbbá az átmeneti állapotok, a termékcsatornabeli komplexek és a termékek esetén az adott stacionárius pontok konformereit is sikerült azonosítanunk. A H-absztrakció esetében, ha az aminocsoporton történik, három, míg ha a metilcsoporton, akkor öt különböző átmeneti állapot szerkezet különböztethető meg. A két H-szubsztitúciós reakciócsatorna és az elölről támadásos mechanizmusú amino-szubsztitúció esetében 2-2-2 átmeneti állapotot azonosítottunk. A kimeneti csatornában, az aminocsoporton végbemenő H-absztrakció kivételével, a termékcsatornabeli komplexek két különböző konformere figyelhető meg minden reakciónál. A termékek esetében az NH_2OH molekula cisz és transz izomerjeit, valamint a CH_3NHOH molekula két konformerét azonosítottuk. Végül az átmeneti állapot elmélet

alapján meghatároztuk a H-absztrakció sebességi együtthatóit különböző hőmérsékleteken. Az általunk számított sebességi együtthatók, melyek figyelembe veszik az alagúteffektust a Wigner-féle korrekció alapján, jó egyezést mutatnak a kísérleti értékekkel.

5.3 OH + GLICIN: H-ABSZTRAKCIÓ

Az OH + glicin reakció potenciálisenergia-felületén az elsőrendű nyeregpontokat és termékcsatornabeli minimumokat azonosítottuk és jellemeztük nagy pontosságú *ab initio* számítások segítségével három különböző útvonalat figyelembe véve: CH_2-, NH_2- és COOH-H absztrakciókat. Az átmeneti állapotok és a termékcsatornabeli komplexek konformereinek maximális számának meghatározásához szisztematikus keresést hajtottunk végre három különböző elméleti szinten. 1296 kezdeti szerkezetből indultunk ki, amelyekre egyenként elsőkörben MP2/3-21G elméleti szinten végeztük el a geometriai optimálásokat és a frekvenciaszámításokat. A kezdeti szerkezeteket molekulán belüli forgatásokkal állítottuk elő a kémiai intuícióval azonosított stacionárius pontokból kiindulva. Ezután az MP2/3-21G szinten kapott szerkezetekre a geometria optimálásokat és frekvenciaszámításokat MP2/aug-cc-pVDZ szinten is elvégeztük. Ezt követően ezeket az optimalizált MP2/aug-cc-pVDZ szerkezeteket tovább pontosítottuk CCSD(T)-F12b/aug-cc-pVDZ szinten. A legmagasabb kvantumkémiai szinten (CCSD(T)-F12b/aug-cc-pVDZ) végzett számítások eredményeként a CH_2-, NH_2- és COOH-H-absztrakciós reakciócsatornák esetén 5, 5 és 5 átmeneti állapotot, illetve 2, 19 és 0 termékcsatornabeli komplexet azonosítottunk. Az átmeneti állapotok és a termékcsatornabeli minimumok konformereinek relatív benchmark energiáit egy kompozit megközelítéssel kaptuk meg, amelyben a CCSD(T)-F12b/aug-cc-pVQZ szinten meghatározott energiákhoz hozzáadtuk a poszt-(T) korreláció hatását, a törzskorrekciót, a skaláris relativisztikus korrekciót, a spin-pálya és a zéruspontí energia korrekciót. Az elkészített energiaprofil alapján megállapítható, hogy a termékek energiája minden reakciócsatorna esetében kisebb, mint a reaktánsoké. A legexotermebb reakció a CH_2 csoportról történő H-absztrakció, melyet követ az NH_2-csoportról történő H-absztrakció, majd a COOH-csoportról történő H-absztrakció következik növekvő energiarendben. Bár a COOH csoportnál fellépő H-absztrakció alacsony, 1,02 kcal/mol-os, klasszikus energiagáttal rendelkezik, ha a klasszikus

értékekhez hozzáadjuk a zéruspont energiakorrekciót, akkor megfigyelhető, hogy mindhárom reakció gát nélkül megy végbe. Az NH_2-csoport reakciójának átmeneti állapotának energiája alacsonyabb, mint a CH_2-csoporté, de a termékcsatornabeli komplexek esetében ellenkező tendencia figyelhető meg. A bemeneti csatornát egydimenziós potenciális energiagörbék segítségével vizsgáltuk a reaktánsok hét különböző orientációjában. A görbék alapján megállapítható, hogy amikor az OH gyök az O atomjával a karbonil-O vagy az aminocsoport N-je felé közelít, akkor taszító kölcsönhatás lép fel a két molekula között. A másik öt orientációban jelentős minimumok figyelhetők meg az energiagörbéken. A reakció stacionárius pontjainak feltérképezése után egy csatolt klaszter minőségű, teljes dimenziós, analitikus potenciálisenergia-felületet fejlesztettünk. A végső PES illesztési hibája a kémiailag releváns régióban 2,82 kcal/mol. Az 1, 10, 20 és 30 kcal/mol ütközési energiáknál végzett dinamikai tesztszimulációk alapján a fizikailag irreleváns termékeket eredményező trajektóriák aránya 3% alatt volt. Minden egyes glicin konformerből 63 000 szimulációt indítottunk ki, így a reakció dinamikáját összesen 504 000 kvázi-klasszikus trajektóriával tanulmányoztuk. A szimulációk megmutatták, hogy a glicin molekula karboxilcsoportjáról történő H-absztrakció nem mindig vezet a H_2O és NH_2CH_2COO termékek képződéséhez. Ehelyett a dehidrogénezett glicin molekula CO_2-ra és CH_2NH_2-re bomlik szét. Továbbá az integrális hatáskeresztmetszetek egyértelműen megmutatták, hogy a dehidrogénezett glicin molekula bomlása az esetek közel 100%-ában megtörténik. Alacsony ütközési energiáknál e háromfragmenses termékcsatorna a legreaktívabb, majd az ütközési energia növekedésével a CH_2 és NH_2 csoportokon végbemenő H-absztrakciós reakciók jelentősebbé válnak. A szórási szögeloszlások mind a CH_2-, mind az NH_2-csoportok esetén általában izotróp eloszlást mutatnak a legtöbb glicin-konformer esetén, néhány esetben pedig előreszórás figyelhető meg. Az OH gyök kezdeti támadási szögeloszlása alapján elmondható, hogy az eloszlás általában izotróp a legtöbb glicin konformer esetén, függetlenül attól, hogy melyik csoporton történik a H-absztrakció. Egyes esetekben az OH gyök szívesebben közelíti meg a glicin molekulát a H atomjával. Ez a megállapítás, hogy az O atommal történő támadás kevésbé előnyös, az OH gyök O atomja és a glicin molekula N vagy O atomjai közötti taszító kölcsönhatásokkal magyarázható, amelyek a nemkötő elektronpárok miatt lépnek fel. Ezzel szemben, amikor az OH gyök a H atomjával közeledik, akkor H-kötések jöhetnek létre a két molekula között. Ezen kölcsönhatás után az OH gyök még mindig felvehet reaktív orientációt, ami lehetővé teszi

a H-absztrakció végbemenetelét. A glicinmolekulára meghatározott kezdeti támadási szögeloszlások szerint, ha a H-absztrakció a CH_2 csoporton történik, akkor az aminocsoporttal történő támadás egyértelműen előnyös minden reaktáns konformer esetében. Ez a jelenség a karbonil-O-val kialakított erősebb H-kötéssel magyarázható az amino-N-hez képest. Következésképpen az OH gyök nagyobb valószínűséggel közelíti meg a CH_2 csoportot az NH_2 csoport felől. Az NH_2 csoporton történő H-absztrakció során azt várjuk, hogy a glicin molekula az aminocsoportjával közelítse meg az OH-gyököt. Ez egyértelműen megfigyelhető a IIn, Vn és VIIp glicin konformerek esetében. A többi reaktáns konformer esetében megállapítható, hogy nincs olyan specifikus orientáció, amelyben a glicin molekula preferáltan közelítené meg az OH-gyököt. Ezen túlmenően nyilvánvaló, hogy a karboxilcsoporton történő frontális támadás egyáltalán nem jellemző. Továbbá a karboxilcsoporton történő H-absztrakció esetén azt várjuk, hogy a glicin molekula a karboxilcsoport oldaláról támadjon. Erre jellemző kezdeti támadási szögeloszlások figyelhetőek meg az Ip, IIIn, IVn és Vn glicin konformerek esetén. A IIn, VIp, VIIp és VIIIn reaktáns konformerek esetén enyhén előnyösebb, ha a glicin molekula az NH_2 csoporttal közelíti az OH gyököt. A VIp és VIIIn glicin konformerek esetében ez a tendencia a következőképpen értelmezhető: bár a glicin molekula aminocsoportja a vízszintes tengely mentén közelebb van a támadó OH-hoz, az ütközés során az OH valójában közelebb kerül a karboxil csoporthoz. Ezenkívül a CH_2 csoport egyfajta "védőpajzsként" funkcionál az NH_2 csoport felett, megnehezítve a hidroxilcsoport számára az aminocsoport megközelítését. A IIn és VIIp glicin konformerek esetében azon reakción túlmenően, ahol az OH gyök egyszerűen leszakít egy H-t a karboxilcsoportról az ütközés során, a reakció úgy is végbemehet, hogy biradikális szerkezet alakul ki. Ebben az esetben a karboxil-H az N atom felé néz, és a H-absztrakció nem a karboxilcsoporton, hanem az aminocsoporon megy végbe. Megállapítható továbbá, hogy a biradikális forma megjelenése a reaktáns glicinmolekulában lévő karboxilcsoport orientációjával függ össze. A karboxilcsoportról a N atomra történő H-transzfer csak akkor figyelhető meg, ha a karboxil-H közelebb van a glicinmolekulában lévő aminocsoporthoz.

5.4 KITEKINTÉS

Összefoglalva, a doktori munkám során három különböző reakció potenciálisenergia-felületét térképeztem fel nagy pontosságú *ab initio* módszerekkel. Ezek az eredmények nemcsak viszonyítási alapként szolgálnak a jelenlegi irodalomban, hanem új reakcióutakat tártak fel és megalapozhatnak jövőbeni PES fejlesztéseket. Munkám során a QCT módszert alkalmaztam a reakciók dinamikájának mélyebb megértéséhez, a reakciók azonban pontosabban szimulálhatók abban az esetben, ha az atommagok mozgását is teljesen a kvantummechanika segítségével írjuk le. Viszont ezen számítások a magas számítási költségük miatt jelenleg csak nagyon kis (5-6 atomos) rendszerekre valósíthatók meg. Továbbá a potenciálisenergia-felületek nemcsak az alapállapotú reakciók vizsgálatát teszik lehetővé, hanem a rezgési gerjesztés hatásainak vizsgálatát is lehetővé teszik, amit az OH + C_2H_6 reakcióval kapcsolatos kutatásaim során én is elvégeztem. A rezgési mód-specifitás vizsgálatán túl egy másik lehetséges jövőbeli irány lehet az, hogy a reaktánsok forgási gerjesztése hogyan befolyásolja a reakcióképességet és a reakciómechanizmusokat. Végül a reakciókat a jövőben folyadékfázisban is érdemes lehet vizsgálni különböző oldószermodellek alkalmazásával, különös tekintettel az OH + glicin reakcióra, melynek tanulmányozása biológiai szempontból is fontos lehet, hiszen az UV sugárzás hatására az emberi szervezetben felszabaduló OH gyökök károsíthatják a biomolekulákat, melyek egyik legegyszerűbb képviselője a glicin.

6 ACKNOWLEDGEMENTS

7 REFERENCES

[1] A. Szabo and N. S. Ostlund, *Modern quantum chemistry: Introduction to advanced electronic structure theory, Mineola N.Y.: Dover Publications*, 1996.

[2] G. C. Shatz and A. Kuppermann, *J. Chem. Phys.*, 1975, **62**, 2502.

[3] G. C. Shatz and A. Kuppermann, *J. Chem. Phys.*, 1976, **65**, 2642.

[4] G. C. Shatz, J. M. Bowman and A. Kuppermann, *J. Chem. Phys.*, 1975, **63**, 674.

[5] D. Skouteris, J. F. Castillo and D. E. Manolopoulos, *Comput. Phys. Commun.*, 2000, **133**, 128.

[6] Polanyi, *J. C. Some Concepts in Reaction Dynamics., Science*, 1987, **236**, 680.

[7] G. C. Shatz, M. C. Calton and J. L. Grant, *J. Phys. Chem.*, 1984, **88**, 2971.

[8] A. Sinha, M. C. Hsiao and F. F. Crim, *J. Chem. Phys.*, 1990, **92**, 6333.

[9] M. J. Bronikowski, W. R. Simpson, B. Girard and R. N. Zare, *J. Chem. Phys.*, 1991, **95**, 8647.

[10] R. B. Metz, J. D. Thoemke, J. M. Pfieffer and F.F. Crim, *J. Chem. Phys.*, 1993, **99**, 1744.

[11] D. H. Zhang and J. C. Light, *J. Chem. Soc.*, 1997, **93**, 691.

[12] J. P. Camden, H. A. Bechtel and R. N. Zare, *Angew. Chem. Int. Ed.*, 2003, **42**, 5227.

[13] Z. H. Kim, A. J. Alexander, H. A. Bechtel and R. N. Zare, *J. Chem. Phys.*, 2001, **115**, 179.

[14] S.Yoon, S. Henton, A. N. Zivkovic and F. F. Crim, *J. Chem. Phys.*, 2002, **116**, 10744.

[15] J. J. Lin, J. Zhou, W. Shiu and K. Liu, *Science*, 2003, **300**, 966.

[16] A. Bonard, V. Daele, J. Delfau and C. Vovelle, *J. Phys. Chem. A.*, 2002, **106**, 4384.

[17] M. G. Bryukov, V. D. Knyazev, S. L. Lomnicki, C. A. McFerrin and B. Dellinger, *J. Phys. Chem. A.*, 2004, **108**, 10464.

[18] H. Lin, Y. Zhao, B. A. Bellingston, J. Pu and D. G. Truhlar, *J. Am. Chem. Soc.*, 2005, **127**, 2830.

[19] B. Zhang, W. Shiu and K. Liu, *J. Phys. Chem. A.*, 2005, **109**, 8989.

[20] S. R. Sellevag, G. Nyman and C. J. Nielsen, *J. Phys. Chem. A.*, 2006, **110**, 141.

[21] L. K. Huynh, A. Ratkiewicz and T. N. Troung, *J. Phys. Chem. A.*, 2006, **110**, 473.

[22] B. A. Ellingson, J. Pu, H. Lin, Y. Zhao and D. G. Truhlar, *J. Phys. Chem. A.*, 2007, **111**, 11706.

[23] P. H. Wine and J. M. Nichovich, *Encyclopedia of Radicals in Chemistry, Biology and Materials*, 2015, **1**, 15.

[24] H. Hakola and H. Hellén, *Nat. Geosci.*, 2016, **9**, 475.

[25] M. Li, A. Pozzer, J. Lelieveld and J. Williams, *Earth Syst. Sci. Data*, 2022, **14**, 4351.

[26] K. D. Dobbs and D. A. Dixon, *J. Chem. Phys.*, 1993, **98**, 8852.

[27] J. Li and H. Guo, *J. Chem. Phys.*, 2015, **143**, 221103.

[28] T. Hashimoto and S. Iwata, *J. Chem. Phys. A*, 2002, **106**, 11.

[29] C. Rangel, M. Garcia-Chamorro, J. C. Corchado and J. Espinosa-Garcia, *Phys. Chem. Chem. Phys.*, 2020, **22**, 14796.

[30] L. Marrodán, T. Pérez and M. U. Alzueta, *Combust. Flame*, 2024, **259**, 112130.

[31] C. J. Nielsen, H. Herrmann and C. Weller, *Chem. Soc. Rev.*, 2012, **41**, 6684.

[32] M. U. Alzueta, T. Pérez and L. Marrodán, *Proc. Combust. Inst.*, 2024, **40**, 105456.

[33] W. Tian, W. Wang, Y. Zhang and W. Wang, *Int. J. Quantum Chem.*, 2009, **109**, 1566.

[34] L. Onel, L. Thonger, M. A. Blitz, P. W. Seakins, A. J. C. Bunkan, M. Solimannejad and C. J. Nielsen, *J. Phys. Chem. A*, 2013, **117**, 10736.

[35] R. Atkinson, R. A. Perry and J. N. Pitts Jr., *J. Chem. Phys.*, 1977, **66**, 1578.

[36] S. A. Carl and J. N. Crowley, *J. Phys. Chem. A*, 1988, **102**, 8131.

[37] N. I. Butkovskaya and D. W. Setser, *J. Phys. Chem. A*, 2016, **120**, 6698.

[38] L. Onel, L. Thonger, M. A. Blitz, P. W. Seakins, A. J. C. Bunkan, M. Solimannejad and C. J. Nielsen, *J. Phys. Chem. A*, 2013, **117**, 10736

[39] G. M. Chaban, D. Wang and W. M. Huo, *J. Phys. Chem. A*, 2015, **119**, 377.

[40] A. G. Császár, *J. Am. Chem. Soc.*, 1992, **114**, 9568.

[41] A. G. Császár, *J. Mol. Struct.*, 1995, **346**, 141.

[42] V. Kasalová, W. D. Allen, H. F. Schaefer III, E. Czinki and A. G. Császár, *J. Comput. Chem.*, 2007, **28**, 1373.

[43] R. M. Balabin, *Chem. Phys. Lett.*, 2009, **479**, 195.

[44] R. M. Balabin, *J. Phys. Chem. Lett.*, 2010, *1*, 20.

[45] V. Barone, M. Biczysko, J. Bloino and C. Puzzarini, *Phys. Chem. Chem. Phys.*, 2013, **15**, 1358.

46 V. Barone, M. Biczysko, J. Bloino and C. Puzzarini, *Phys. Chem. Chem. Phys.*, 2013, **15**, 10094.

47 E. M. Orján, A. B. Nacsa and G. Czakó, *J. Comput. Chem.*, 2020, **41**, 2001.

48 D. Yu, A. Rauk and D. A. Armstrong, *J. Am. Chem. Soc.*, 1995, **117**, 1789.

49 A. Galano, J. R. Alvarez-Idaboy, L. A. Montero and A. VivierBunge, *J. Comput. Chem.*, 2001, **22**, 1138.

50 A. K. Croft, C. J. Easton and L. Radom, *J. Am. Chem. Soc.*, 2003, **125**, 4119.

51 Y. Huang, L. Guler, J. Heidbrink and H. Kenttamaa, *J. Am. Chem. Soc.*, 2005, **127**, 3973.

52 A. Mavrandonakis, S. C. Farantos and G. E. Froudakis, *J. Phys. Chem. B*, 2006, **110**, 6048.

53 G. Yang, Y. Zu and L. Zhou, *J. Phys. Org. Chem.*, 2008, **21**, 34.

54 P. Carbonniere, A. Dargelos, I. Ciofini, C. Adamo and C. Pouchan, *Phys. Chem. Chem. Phys.*, 2009, **11**, 4375.

55 R.-J. Lin, C.-C. Wu, S. Jang and F.-Y. Li, *J. Mol. Model.*, 2010, **16**, 175.

56 J. Uranga, O. Lakuntza, E. Ramos-Cordoba, J. M. Matxain and J. I. Mujika, *Phys. Chem. Chem. Phys.*, 2016, **18**, 30972.

57 M. C. Owen, I. G. Csizmadia, B. Viskolcz and B. Strodel, *Molecules*, 2017, **22**, 655.

58 M. Born and R. Oppenheimer, *Ann. Phys.*, 1927, **84**, 457.

59 S. F. Boys, *Proc. R. Soc. London. Ser. A. Math. Phys. Sci.*, 1950, **200**, 542.

60 R. Ditchfield, W. J. Hehre and J. A. Pople, *J. Chem. Phys.*, 1971, **54**, 724.

61 W. J. Hehre, K. Ditchfield and J. A. Pople, *J. Chem. Phys.*, 1972, **56**, 2257.

62 T. H. Dunning, *J. Chem. Phys.*, 1989, **90**, 1007.

63 D. E. Woon and T. H. Dunning, *J. Chem. Phys.*, 1993, **98**, 1358.

64 D. E. Woon and T. H. Dunning, *J. Chem. Phys.*, 1995, **103**, 4572.

65 J. G. Hill, S. Mazumder and K. A. Peterson, *J. Chem. Phys.*, 2010, **132**, 054108.

66 C. Møller and M. S. Plesset, *Phys. Rev.*, 1934, **46**, 618.

67 J. A. Pople, J. S. Binkley and R. Seeger, *Int. J. Quantum Chem.*, 1976, **10**, 1.

68 J. Čížek, *J. Chem. Phys.*, 1966, **45**, 4256.

69 K. Raghavachari, G. W. Trucks, J. A. Pople and M. Head-Gordon, *Chem. Phys. Lett.*, 1989, **157**, 479.

[70] R. J. Bartlett, *J. Phys. Chem.*, 1989, **93**, 1697.

[71] G. D. Purvis and R. J. Bartlett, *J. Chem. Phys.*, 1982, **76**, 1910.

[72] P. Piecuch and J. Paldus, *Int. J. Quantum Chem.*, 1989, **36**, 429.

[73] G. E. Scuseria and T. J. Lee, *J. Chem. Phys.*, 1998, **93**, 5851.

[74] T. B. Adler, G. Knizia and H. J. Werner, *J. Chem. Phys.*, 2007, **127**, 221106.

[75] G. Knizia, T. B. Adler and H. J. Werner, *J. Chem. Phys.*, 2009, **130**, 054104.

[76] H. B. Schlegel, *WIREs Computaional Molecular Science*, 2011, 790.

[77] A. Banarjee, N. Adams and J. Simons, *J. Chem. Phys.*, 1985, **89**, 52.

[78] H. B. Schlegel, *in Modern Electronic Structure Theory: Part I., 1995, pp. 459– 500*.

[79] T. Győri and G. Czakó, J. Chem. *Theory Comput.*, 2020, **16**, 51.

[80] B. J. Braams and J. M. Bowman, *Int. Rev. Phys. Chem.*, 2009, **28**, 577.

[81] Z. Xie and J. M. Bowman, *J. Chem. Theory Comput.*, 2010, **6**, 26.

[82] W. L. Hase, *Encyclopedia of Computational Chemistry, Wiley, New York, 1998, pp. 399– 407*.

[83] J. Noga and R. J. Bartlett, *J. Chem. Phys.*, 1986, **86**, 7041.

[84] Y. J. Bomble, J. F. Stanton, M. Kállay and J. Gauss, *J. Chem. Phys.*, 2005, **123**, 054101.

[85] G. S. Hammond, *J. Am. Chem. Soc.*, 1955, **77**, 334.

[86] T. Győri and G. Czakó, *J. Chem. Phys.*, 2022, **156**, 071101.